Theses and Dissertations

December 2014

Novel Nanostructured Materials for Solar Fuel Production and Advanced Rechargeable Batteries

Cunyu Zhao
University of Wisconsin-Milwaukee

NOVEL NANOSTRUCTURED MATERIALS FOR SOLAR FUEL

PRODUCTION AND ADVANCED RECHARGEABLE BATTERIES

by

Cunyu Zhao

A Dissertation Submitted in

Partial Fulfillment of the

Requirements for the Degree of

Doctor of Philosophy

in Engineering

at

The University of Wisconsin-Milwaukee

December 2014

ABSTRACT

NOVEL NANOSTRUCTURED MATERIALS FOR SOLAR FUEL PRODUCTION AND ADVANCED RECHARGEABLE BATTERIES

by

Cunyu Zhao

The University of Wisconsin-Milwaukee, 2014
Under the Supervision of Professor Ying Li

Non-renewable fossil fuels are the major sources to meet the energy, electricity and transportation demands of today's world. The over consumption of fossil fuels will lead to the increasing energy crisis and disastrous effects such as air pollution, global warming etc.

The primary greenhouse gas is CO_2 mainly emits from the combustion of fossil fuels. Photocatalytic reduction of CO_2 using sunlight as the energy input is a promising way to reduce CO_2 level in the atmosphere and in the meantime produce alternative fuels such as CO, methane, methanol, etc. Among the various photocatalyst materials reported, nanomaterial TiO_2 is the most widely studied due to its suitable band positions, high chemical stability, non-toxic nature, and low cost. However, the energy conversion efficiency using TiO_2 for CO_2 photoreduction is still low, mainly due to the reasons of (1) high probability of recombination of photo-induced electron-hole pairs, (2) fast backward reaction of hydrogen and oxygen to form water, and (3) limited ability of visible light utilization.

Another efficient way to decrease CO_2 emissions is to reduce fossil fuels consumption. The invention of hybrid electric vehicles (HEVs) and electric vehicles (EVs) are great promise of replacing traditional gasoline driven automobiles. As one of the

new generation high energy density batteries, lithium-sulfur (Li-S) battery is very attractive because sulfur has a high theoretical capacity of 1,675 mA h g^{-1}. However, the practical realization of Li-S batteries is limited by several problems: (1) poor electrical conductivity of sulfur (2) dissolution of the lithium polysulfide intermediates into the electrolyte, and (3) large volume expansion of sulfur during cycling.

One objective of this study is to demonstrate high-efficiency photocatalysts using innovative hybrid nanostructures that consist of Ce doped TiO_2 dispersed on mesoporous silica (SBA-15) or noble-metal nanoparticles Ag supported on TiO_2 or MgAl-LDOs (layered double oxides) grafted on TiO_2 (TiO_2-MgAl LDOs). The use of Ce doping could result in smaller TiO_2 nanocrystals and facilitate electron-hole separation, while SBA-15 provides good dispersion of TiO_2 and a strong interaction between TiO_2 and the substrate. And Ag species on TiO_2 facilitate electron trapping and transport to the catalyst surface, and thus, can potentially enhance multi-electron transfer processes. TiO_2-MgAl LDOs is favorable for CO_2 species adsorption on the photocatalyst, therefore, compensating the weakened CO_2 adsorption ability at higher temperature in the presence of H_2O vapor. The other objective of this study is to find alternative materials as anode for Li-ion battries and demonstrate high-performance Li-S battery electrodes using hybrid nanomaterials consist of sulfur infiltrated porous micrsophere carbon (PMC). Carbon/TiO_2 was found to be promising as anode alternative to replace graphite materials to avoid safety issues for Li-ion batteries. Cathodes made of sulfur infiltrated in such a multi-modal porous carbon framework provide advantageous properties that guaranttee the superior electrochemical performance.

Ce-doped TiO_2 on SBA-15, Ag deposited TiO_2 (Ag/TiO_2) and MgAl-LDOs grafted on TiO_2 (TiO_2-MgAl LDOs) were synthesized and characterized for applications in CO_2 photoreduction with H_2O. Ce-doped TiO_2 were synthesized using sol-gel method and SBA-15 was then added to the sol to prepare Ce-doped TiO_2 on SBA-15 nanocomposites. Modification of TiO_2 with Ce significantly stabilized the TiO_2 anatase phase and increased the specific surface area, which contributed to an improvement of CO production from CO_2 reduction. Dispersing Ce-TiO_2 nanoparticles on the mesoporous SBA-15 support further enhanced both CO and CH_4 production. The superior catalytic activity may be related to the partially embedded Ce-TiO_2 nanoparticles in the ordered 1-D pores in SBA-15 that form synergies between the different components of the catalysts and enhance the diffusion and adsorption of CO_2. Ag/TiO_2 nanocomposites were synthesized by spray pyrolysis technique. This work has demonstrated the feasibility of syngas (H_2 and CO) production from a gas mixture of CO_2, H_2O and CH_3OH hrough a photocatalytic reduction process on Ag/TiO_2 nanocomposite catalysts under solar irradiation.The material property analysis and photocatalytic activity results showed that the ultrasonic spray pyrolysis method is much superior to conventional wet impregnation process with the advantages of smaller Ag nanoparticles, a better Ag dispersion on TiO_2, and a higher fraction of metallic Ag species, which facilitate charge transfer and improve photocatalytic activity. TiO_2-MgAl LDOs were synthesized by hydrothermal and coprecipitation method. As the MgAl LDOs concentration increases, TiO_2 crystal size was increased. MgAl LDOs grafting on TiO_2 cuboids may help improve the adsorption ability of CO_2 onto TiO_2 which improves the photocatalytic activity of CO_2 reduction.

Our work also entails the synthesis and characterization of carbon coated TiO_2 for the application of Li-ion batteries and sulfur infiltrated porous microsphere carbon (PMC/S) for the application of Li-S batteries. Carbon decorated on commercial TiO_2 nanoparticles (P25 and P90) composites with optimized carbon concentration and structure were fabricated by a facile process employing carbonization method. The electrochemical performance of C-P90 was superior to C-P25 because of its higher specific surface area and larger anatase fraction that can accommodate more lithium ions. 1.9% carbon was found to form an optimized carbon layer on TiO_2 that can improve the electronic conductivity. The PMC was synthesized by spray pyrolysis method. Then PMC/S was fabricated via a liquid phase infiltration. The novel-structured porous carbon microspheres possess a controllable multi-modal pore size distribution, i.e., a combination of interconnected micropores, mesopores and macropores, which is beneficial for Li-S batteries electrochemical performance.

Future work includes further improvement of PMC/S composites to inhibit shuttle effect and improve the electrode performance including the cyclability and rate capability.

TABLE OF CONTENTS

LIST OF FIGURES

LIST OF TABLES

LIST OF ABBREVIATIONS

1D	one-dimensional
3D	three-dimensional
BET	Brunauer-Emmett-Teller method
BJH	Barrett-Joyner-Halenda method
CB	conduction band
CV	cyclic voltammogram
DFT	density functional theory
DI	deionized
DRIFTS	diffuse reflectance infrared fourier transform spectroscopy
e-h	electron-hole
EDX	energy-dispersive X-ray spectroscopy
EIS	electrochemical impedance spectroscopy
EVs	electric vehicles
FID	flame ionization detector
GHG	greenhouse gas
GHGs	greenhouse gases
HEVs	hybrid electric vehicles
HRTEM	high resolution transmission electron microscopy
IR	infrared
LDHs	layered double hydroxides
LDOs	layered double oxides
LIBs	lithium-ion battries

Li-S   lithium-sulfur

NPs   nanoparticles

PMC   porous microsphere carbon

PMC/S   porous microsphere carbon/sulfur

PSD   pore size distribution

Rct   interfacial resistance

SEI   solid-electrolyte interface

SEM   scanning electron microscopy

SP   spray pyrolysis

SPR   surface plasmon resonance

TCD   thermal conductive detector

TEM   transmission electron microscopy

TiO_2 A   Anatase   B   Brookite   R   Rutile

TGA   thermogravimetric analysis

USP   ultrasonic spray pyrolysis

UV   ultraviolet

UV-vis   ultraviolet-visible

VB   valence band

WI   wet impregnation

XPS   X-ray photoelectron spectroscopy

XRD   X-ray diffraction

XREM   X-ray elemental mapping

ACKNOWLEDGEMENTS

CHAPTER 1 INTRODUCTION AND RESEARCH OBJECTIVES

1.1 Introduction

Energy supply is essential to economic development everywhere in the world, and current pattern of global energy development greatly relies on fossil fuels (coal, natural gas and oil). The future global economy is likely to consume ever more such non-renewable fossil fuels, especially with the rising energy demand of developing countries. As a result, this is causing crisis that our energy resources are starting to run out, with devastating consequences for the global economy development. The combustion of fossil fuels for energy and transportation (see **Fig. 1.1**, main activities that consume fossil fuels and emits CO_2) emits CO_2 directly to the atmosphere, which is the primary greenhouse gas (GHG). The energy crisis is further exacerbated by the tremendous risk of climate change associated with the use of fossil fuels.
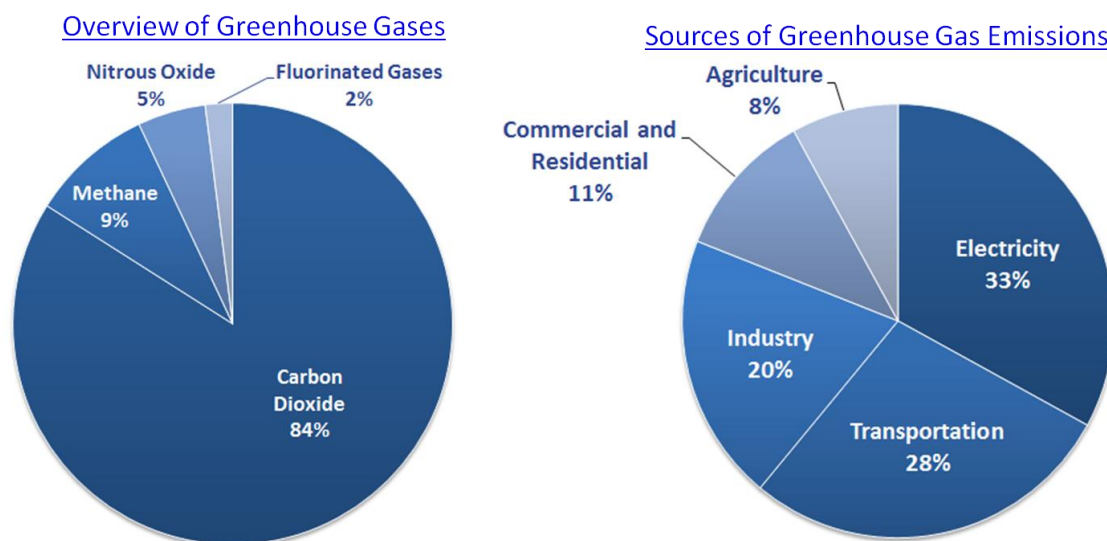
Figure 1.1 Greenhouse gases (GHGs) emissions and the primary sources of greenhouse gas emissions in the United States in 2011.[1]

CO_2 emissions is likely to increase as the fossil fuels consumption increases. The huge amount of CO_2 existing in the atmosphere is expected to cause continued global warming which has substantial impacts on the environment, human health and economy. How to solve this environmental concern has become an emergency.   Although strategies have tried to bury CO_2 in the deep ground or ocean, potential risk is not fully evaluated and catastrophe may occur if overload of CO_2 pumped into deep ground.   Photocatalytic reduction of CO_2 using sunlight as the energy input is a promising way to reduce CO_2 level in the atmosphere and in the meantime produce alternative fuels such as CO, methane, methanol, etc. Semiconductor photocatalyts such as WO_3, ZrO_2, Ga_2O_3, and TiO_2 [2-5] have been studied for such applications, and among them, TiO_2 has been considered the most appropriate photocatalyst due to its high photosensitivity, non-toxic nature, low cost, and easy availability.[6-10] However, the photoefficiency of CO_2 reduction on TiO_2 is usually very low, mainly due to the fast recombination of photo-excited electron-hole (e-h) pairs and the wide band gap of TiO_2 (3.2 eV for anatase) that does not allow the utilization of visible light.[11-12] Innovations are needed overcome these limitations to enhance the CO_2 conversion to alternative fuels. [13-14]

Photocatalytic reduction of CO_2 to alternative fuels is a promising way to reduce CO_2 level in the long run, which does not mean we could keep using the non-renewable fossil fuels. It is essential to find alternative energy to replace the fossil fuels especially for transport energy, as transportation consists almost 1/3 of the total energy consumption (see **Fig. 1.1**). And it is expected that the energy use in the transportation sector will continue to grow at rates that are considerably larger than other sectors of the U.S. economy (see **Fig. 1.2**). **Fig. 1.3** shows that petroleum is the main fossil fuels used for the energy

requirement in the transportation. Is it possible to replace the petroleum by other energy system? Scientists have proposed to apply lithium-ion batteries (LIBs) in the hybrid electric vehicles (HEVs) or electric vehicles (EVs) to lower or avoid the petroleum consumption. The HEVs or EVs demand for safe, light, low-cost, high-energy density, and long-lasting rechargeable batteries. Current lithium-ion batteries (LIBs) using transition metal compounds as cathode materials operate on the basis of topotactic intercalation reactions, which inherently limits its storage capacity to around 300 mAh g^{-1} for any perspective system. As a result, the current LIBs cannot provide a suitably long driving distance for EVs.[15-18] As one of the new generation high energy density batteries, lithium-sulfur (Li-S) battery is very attractive because sulfur has a high theoretical capacity of 1,675 mA h g^{-1}, nearly five times higher than that of existing transition metal oxides and phosphates materials.[19-22]
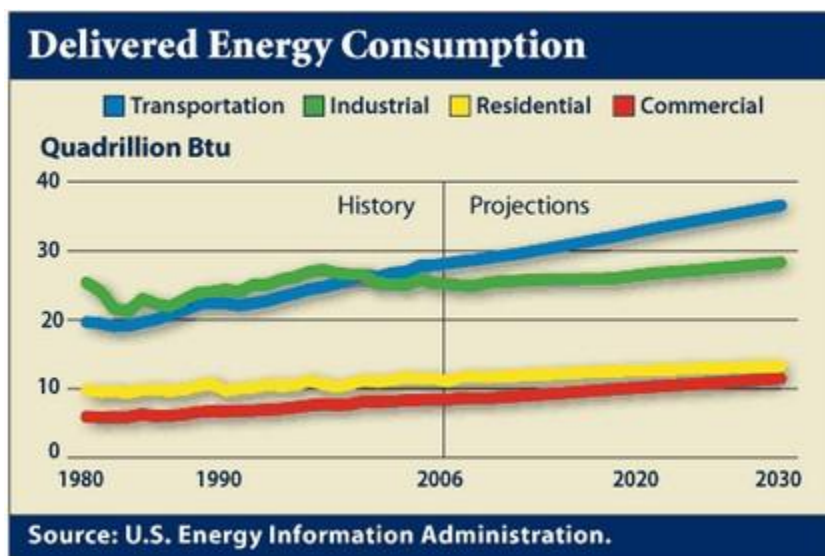
Figure 1.2 Energy consumption for different sectors of US economy.[23]
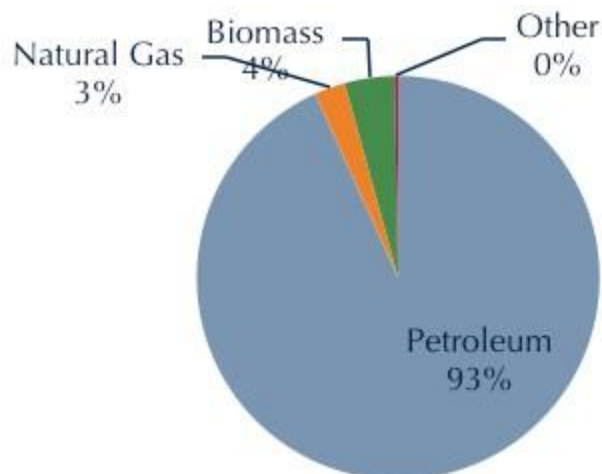
Figure 1.3 Energy sources in the US transportation sector 2010. [24]
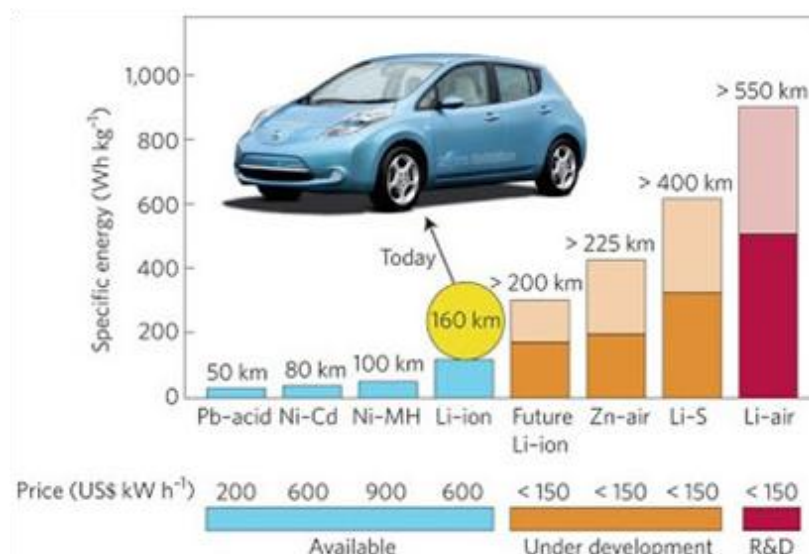
Figure 1.4 Energy density of various battery technologies.[25]

1.2 Solar fuel production using CO_2 as the feedstock

Photocatalytic hydrogen production from water using semiconductor catalysts is a promising way to convert solar energy to clean and renewable hydrogen fuel energy. [26-28] For efficient water splitting, the conduction band (CB) level of the semiconductor should be more negative than water reduction level (to produce H_2) while the valence band (VB) level should be more positive than water oxidation level (to produce O_2), as shown in **Fig.**

1.5. Among the various photocatalyst materials reported, TiO_2 is the most widely studied due to its suitable band positions, high chemical stability, non-toxic nature, low cost, and easy availability.
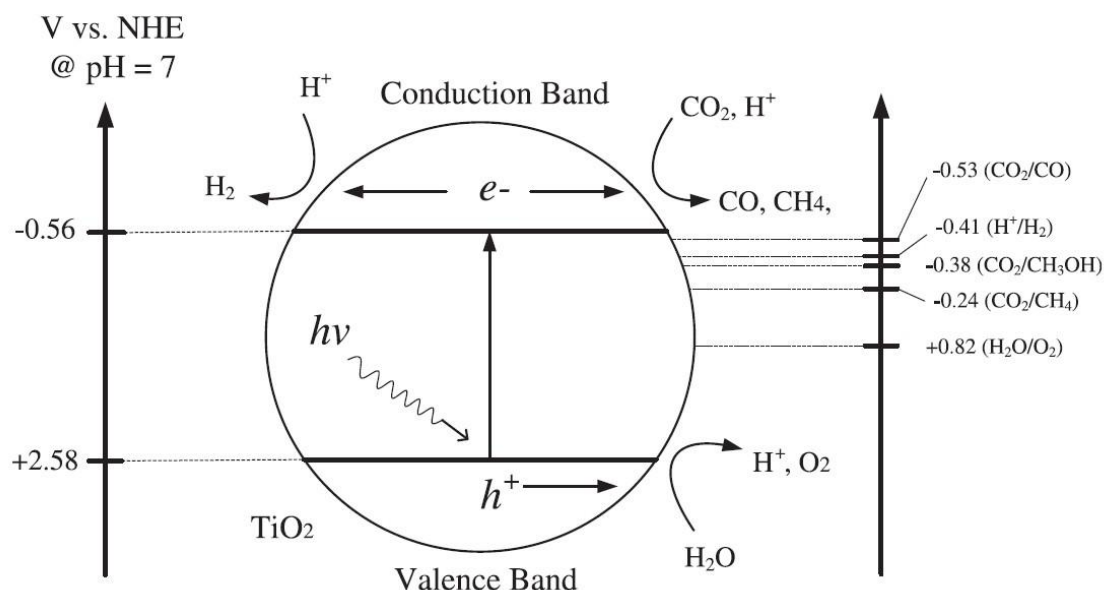
Figure 1.5 Mechanism of photocatalytic hydrogen production and CO_2 reduction with water on TiO_2 semiconductor and their reduction potentials at pH 7 vs. NHE.

Besides hydrogen production from photocatalytic water splitting, another promising solar fuel technology is to photocatalytically reduce carbon dioxide with water to generate gaseous or liquid fuels such as CO, methane, methanol, etc. **Fig. 1.5** shows that these CO_2 reduction reactions are theoretically feasible on TiO_2. However, photocatalytic CO_2 reduction is believed to be more challenging than simply water splitting, because CO_2 is thermodynamically very stable, the CO_2/CO reduction potential is even more negative than that of H_2O/H_2, and the multi-electron processes (i.e., six electron reduction to produce methanol and eight-electron reduction to produce methane) have very low efficiency. Hence, many studies have also been conducted to modify the TiO_2 catalysts to enhance the

CO_2 photoreduction rate, including metal loading, nonmetal doping, and usage of a high surface area substrate, etc.

1.3 Lithium Secondary Batteries

Lithium ion batteries (LIBs) have been dominating the power sources of portable electronic devices for decades. The critical performance indicators for LIBs are capacity, cyclability and rate capability, which are strongly dependent on the active electrode materials. Graphitic carbons are most commonly used as conventional commercial anode materials owing to its low cost, relatively high energy density and very low flat working potential. However, graphitic carbon anode materials suffer the disadvantages of severe safety issues because of its low operating voltage (~0.1 V vs Li/Li^+), poor life cycle performance due to solid-electrolyte interface (SEI) film and the formation of dendritic lithium on the surface of graphitic carbons anode. Thus, it is essential to make improvements such as safety, cost, high efficiency and long cycle life of the anode materials for LIBs.

As one of the new generation high energy density batteries, lithium-sulfur (Li-S) battery is very attractive because sulfur has a high theoretical capacity of 1,675 mA h g^{-1}, nearly five times higher than that of existing transition metal oxides and phosphates materials.[19-22] Moreover, sulfur is light, cheap, and abundant. However, the practical realization of Li-S batteries is limited by several problems: (1) poor electrical conductivity of sulfur (only 5×10^{-30} S/cm at 25 ˚C),[29-30] (2) dissolution of the lithium polysulfide (Li_2S_x, $4 \leq x \leq 8$) intermediates into the electrolyte,[31-32] and (3) large volume expansion of sulfur (~80%) during cycling. [33-34] Consequently, Li-S batteries suffer from rapid capacity decay and low Coulombic efficiency.

1.4 Summary and Literature Review

Aimed at solving the problems of TiO_2-based photocatalysts for CO_2 photoreduction, i.e. low photoefficiency of CO_2 reduction on TiO_2, the fast recombination of photo-excited electron-hole (e-h) pairs and the wide band gap of TiO_2, modification of TiO_2 needs to be studied in this work. During the past decade, lots of work about CO_2 photoreduction has been done but the mechanism still maintains opaque. Ceria and silver will be used to modify TiO_2 to study the unclear mechanism of CO_2 photoreduction.

Rare earth element modified TiO_2 have not been studied for CO_2 photoreduction, although they have demonstrated enhanced photocatalytic oxidation ability than bare TiO_2.[8, 35-36] Cerium (Ce) is one of the four most abundant rate earth elements, and composites of Ce-TiO_2 have shown enhanced photocatalytic activity for water splitting and degradation of organic compounds.[37-40] The Ce^{3+}/Ce^{4+} redox couple may facilitate charge transfer.[41] Besides modifying the properties and nanostructures of TiO_2 itself, many approaches have been used to immobilize TiO_2 nanoparticles on mesoporous substrates such as molecular sieve 5A, amorphous silica, and SBA-15,[5, 42-44] and the direct benefits include larger surface area and better dispersion of the nano-sized catalysts. It has been reported that Cu-TiO_2, Ru-TiO_2, and TiO_2 supported on amorphous silica showed higher CO_2 photoreduction rates than the catalysts without supports.[5, 42, 45] The Si-OH group on SBA-15 was found to enhance the interaction of CO_2 and H_2O on the catalyst surface based on the results of an IR study.[46] Experimental results also demonstrated an enhancement of CO_2 photoreduction to methanol on a 2%Cu-TiO_2/SBA-15 sample compared with 2%Cu-TiO_2, and the promotional effect was likely attributed to the synergistic effect between the metal species, TiO_2 and the support.[47]

As for Ag/TiO_2 photocatalyst, photocatalytic H_2 production and CO_2 reduction using water as the reductant are mostly being investigated separately in the literature, very few publications report on the simultaneous H_2 production and CO_2 reduction in one experimental system. Many literature publications on CO_2 photoreduction either did not detect H_2 production or simply did not measure H_2 production; only a few studies reported concurrent production of H_2 and C1 or C2 fuels but the H_2 yield was at the similar level or even less than the hydrocarbon fuels.[6, 48-49] In addition, most of the experiments were carried out in an aqueous system where many other reaction products such as methanol, formic acid, and formaldehyde were detected and the product selectivity was not controlled.[50-51] Hence, it is desirable to be able to control the H_2: CO ratio in the products and to eliminate the unwanted reaction intermediates or products so that a high purity syngas can be produced. In this regard, a gas-phase reaction system may be more appropriate than an aqueous system, because in our previous work of photocatalytic CO_2 reduction with water vapor,[5, 52] CO was the main reaction product with formation of minor CH_4 and no other products were detected. H_2 production was not detected using bare TiO_2 or Cu/TiO_2 in our previous work,[5, 52] but the addition of noble metals such as Pt and Ag to TiO_2 has been demonstrated for effective H_2 production in the literature.[53-55] Therefore, the first objective of this work was to explore the feasibility of syngas production from CO_2 and water vapor through a photocatalytic process using a silver-modified TiO_2 (Ag/TiO_2) nanoparticle catalyst. Ag was selected because it is much less expensive than Pt and Ag/TiO_2 has shown effectiveness in H_2 production [53]and CO_2 photoreduction [48]in separate studies.

Our research work on CO_2 photoreduction was not only focused on tackling the

major obstacles, but also on other factors that hinder the photocatalytic activity but are rarely studied in the open access literature, such as the weakened CO_2 adsorption on TiO_2 in the presence of H_2O vapor at the solid-gas interface and limited desorption of reaction products or intermediates from the catalyst surface. In order to improve the CO_2 photoreduction conversion efficiency to hydrocarbon fuels, it is highly desirable to enhance the CO_2 adsorption on the photocatalysts. We have reported works about MgO-TiO_2 hybrid adsorbent-photocatalyst prepared by different methods. MgO is chosen as CO_2 adsorbent because of its good CO_2 adsorption ability that is boosted in the presence of H_2O vapor. We found that MgO-TiO_2 hybrid catalysts possessed a much more stable catalytic performance than pristine TiO_2, which may be due to the easier desorption of reaction intermediates and the enhanced CO_2 adsorption by MgO.

However, the CO_2 adsorption capacity for MgO was not high enough comparing with hydrotalcite-derived mixed oxides based on our previous work and other groups' reported literature. As sorption materials, activated MgAl-LDOs have recently been found to have a high sorption capacity for CO_2. Since the flue gas from a coal burner is with a high temperature around 400-600 $^{\circ}C$ and the real flue gas emitted to the atmosphere is with a temperature around 110-160 $^{\circ}C$, it is essential to adsorb CO_2 at high temperatures instead of cooling it to room temperature for CO_2 photocatalytic reduction application to be more feasible. In particular, MgAl-LDOs can capture much more CO_2 than MgO at higher temperature range 150-450 $^{\circ}C$. Therefore, we aim to design a novel hybrid composite incorporating an adsorbent with strong CO_2 adsorption ability and a TiO_2 photocatalyst. Most literature reported that nano-size TiO_2 were used for many purposes such as air purification, degradation of organic matters, heavy metal removal   and photocatalytic

CO_2 reduction to alternative fuels because nano-size TiO_2 possess high surface area which guarantee its high photocatalytic activity. However, more and more papers recently pointed out that nano-sized TiO_2 material could be possibly dangerous to human health since the ultra-small size particles could penetrate into human body from skin and nose especially when it is applied for air purification or photocatalysts for gaseous phase CO_2 conversion. There are also problems when nano-sized TiO_2 is used in liquid phase. The nano-sized TiO_2 particles make it extremely difficult to separate from solutions to recover. Therefore, much attention is focused on the possibility of micron size TiO_2 application as photocatalysts.

Targeting on making improvements such as safety, cost, high efficiency and long cycle life of the anode materials for LIBs, it is essential to find alternatives to replace the commercial graphite materials. The critical performance indicators for LIBs are capacity, cyclability and rate capability, which are strongly dependent on the active electrode materials. Graphitic carbons are most commonly used as conventional commercial anode materials owing to its low cost, relatively high energy density and very low flat working potential. However, graphitic carbon anode materials suffer the disadvantages of severe safety issues because of its low operating voltage (~0.1 V vs Li/Li^+), poor life cycle performance due to solid-electrolyte interface (SEI) film and the formation of dendritic lithium on the surface of graphitic carbons anode. Researchers in the scientific and industrial communities have investigated different materials such as silicon, tin (II) based oxide, and TiO_2 as LIBs anode to replace graphite materials in order to eliminate the safety issue and meanwhile improve LIBs performance. Different from tin (II) based oxides and silicon, TiO_2 material is structural stable during lithium insertion and extraction which means a very low volume change (<4% for Li_xTiO_2, $0 \leq x \leq 1$) for electrode. This advantage

guarantees its good stability during charge/discharge process at high current density rate. Moreover, its high working voltage (> 1.5 V vs Li/Li$^+$) avoids reactions with organic electrolyte and short circuit caused by electrode expansion during cycling that make it safer than graphite anode material. However, TiO$_2$ anodes practical capacity is only 168 mAh g^{-1} because of the poor electronic and ionic conductivity in its bulk form, limiting TiO$_2$ anode practical applications. These problems could be tackled via modification with carbon coating on TiO$_2$.

While the new generation of Li-S batteries system offers promising alternative for the energy requirements, it also presents challenges as mentioned above. To address the above challenges, various cathode materials for Li-S batteries have been explored to enhance electrical conductivity, reduce the active sulfur loss by preventing polysulfides from dissolving in the electrolyte, and accommodate the sulfur volume expansion. In 2009, Nazar and co-workers reported a pioneering work in the Li-S cathode material by incorporating sulfur into a highly ordered mesoporous carbon (CMK-3) and coating sulfur-CMK-3 with polyethylene glycol (PEG).[15] Those materials exhibited good stability over 20 cycles tested and had high initial discharge capacities at 1,320 mA h g^{-1} and 1,005 mA h g^{-1} at 0.1 C rate (1 C = 1,675 mA/g) with and without PEG modification, respectively. Nazar's work inspired the investigation of many carbon materials as sulfur substrates such as porous carbon frameworks,[29, 56-60] carbon nanotubes,[34, 61-62] hollow carbon nanofibers,[16] graphene,[63-64] and conductive polymers.[15, 65-66] Cui et al.[65] reported a poly (3,4-ethylenedioxythiophene):poly (styrene sulfonate) (PEDOT:PSS) coated CMK-3/sulfur that could achieve 96-98% Coulombic efficiency.

Most of the above mentioned literature reports carbon materials having one-dimensional (1D) channel/pore structure or two-dimensional (2D) layered architectures with micropores (< 2 nm) or mesopores (6-8 nm). Three-dimensional (3D) hierarchical porous structures such as bulk carbon or nanoplates with a large surface area, good electrolyte permeability, and good electrochemical performance have also been designed in supercapacitors,[67-68] lithium-ion batteries,[69-70] and lithium-sulfur batteries.[71]   Regardless of the number of dimensions, pore structure and sizes are important factors that determine the electrochemical performance. It has been reported that mesopores can enhance the initial discharge capacity of carbon-sulfur composites and micropores can effectively restrain the shuttling effect.[72-74] A 3D carbon framework can usually be designed with larger pores (e.g., macropores) that are in favor of ion transport and electrolyte permeation from various directions into the carbon porous structure.

1.5 Research Objectives of Outline of the Dissertation

One of the objectives of the research is to demonstrate novel TiO_2-based photocatalysts with hybrid composites structures and enhanced activity for CO_2 reduction and H_2 production and contribute more information about the unclear reaction mechanism. Another objective is to incorporate carbon and sulfur with novel structure to solve the problems that limit lithium-sulfur batteries technology. In order to achieve the research objectives, the research work is divided into five major tasks, which are summarized below.

Task 1. Nanostructured Ce-TiO$_2$/SBA-15 Composites for CO$_2$ Photoreduction (Chapter 2)

The objective of this task is to synthesize Ce-TiO$_2$/SBA-15 materials with high dispersion of TiO_2 and Ce could help facilitating electron-hole separation to decrease e-h pair recombination rate to enhance the activity. Three subtasks will be carried out:

- Ce-TiO$_2$ composites will be synthesized by sol-gel method.

- SBA-15 will be synthesized according to well-known method to be used as a support for Ce-TiO$_2$. Ce-TiO$_2$/aSiO$_2$ (amorphous silica) will be synthesized to compare with Ce-TiO$_2$/SBA-15.

- The resulting nanomaterials will be characterized using various techniques, such as scanning electron microscopy (SEM), transmission electron microscopy (TEM), high-resolution TEM (HRTEM), X-ray diffraction (XRD), X-ray photoelectron spectroscopy (XPS), and UV-vis diffuse reflectance spectra. Finally, the nanomaterials will be applied to CO_2 photoreduction.

Task 2. Ag/TiO$_2$ Nanocomposite Photocatalysts For Simultaneous H$_2$ Production And CO$_2$ Reduction (Chapter 3)

The objectives of this task are to fabricate and characterize Ag/TiO$_2$ nanocomosites via ultrasonic spray pyrolysis for simultaneous H$_2$ production and CO$_2$ reduction to produce syngas (CO+H$_2$) and to study the mechanism for the photocatalytic reaction. Three subtasks will be carried out:

- Ag/TiO$_2$ nanocomosites will be fabricated using ultrasonic spray pyroysis and wet impregnation method.

- The resulting nanomaterials will be characterized using various techniques, such as scanning electron microscopy (SEM), transmission electron microscopy (TEM), high-resolution TEM (HRTEM), X-ray diffraction (XRD), and UV-vis diffuse reflectance spectra. And the nanomaterials will be applied to both water splitting and CO$_2$ photoreduction.

- The CO$_2$/H$_2$O/CH$_3$OH ratio will be adjusted for the photocatalytic reaction to check if we can produce syngas with tunable CO/H$_2$ ratio.

Task 3. Hybrid MgAl LDO-TiO$_2$ Composites for CO$_2$ Photoreduction (Chapter 4)

The objectives of this task are to fabricate and characterize MgAl layered double oxides grafted TiO$_2$ rods composites and apply the materials to CO$_2$ photoreduction. The mechanism of CO$_2$ adsorption-desorption ability provided by MgAl LDO on TiO$_2$ will be studied. Three subtasks will be carried out:

- MgAl LDO-TiO$_2$ with different MgAl LDO concentration will be fabricated by coprecipitation method. The morphology of MgAl LDO will be controlled by adjusting the Mg, Al amount.

- The resulting materials will be characterized using various techniques, such as scanning electron microscopy (SEM), transmission electron microscopy (TEM),

high-resolution TEM (HRTEM), X-ray diffraction (XRD), thermogravimetric analysis (TGA) and UV-vis diffuse reflectance spectra. Finally, the nanomaterials will be applied to CO_2 photoreduction.

Task 4. Carbon-TiO$_2$ Nanocomposites Prepared With Simple Method For Lithium-Ion Batteries (LIBs) (Chapter 5)

The objectives of this task are to fabricate and characterize carbon-TiO_2 hybrid nanocomposites and apply the materials to LIBs. The mechanism of carbon formation on TiO_2 will be discussed and the electrochemical performance of C-TiO_2 hybrid materials will be studied. Four subtasks will be carried out:

- C-TiO_2 with different carbon concentration will be synthesized by a simple carbonization process. The carbon content will be controlled by adjusting the sucrose amount.

- The resulting materials will be characterized using various techniques, such as scanning electron microscopy (SEM), transmission electron microscopy (TEM), high-resolution TEM (HRTEM), X-ray diffraction (XRD), and thermogravimetric analysis (TGA). And the nanomaterials will be used as anode materials for LIBs.

- Electrodes and half-coin cell will be prepared and their performance will be investigated.

- The performance of C-TiO_2 nanomaterials as anode will be optimized.

Task 5. Hierarchical Sulfur-Infiltrated Porous Microspheres Carbon For High Energy Lithium-Sulfur Batteries (Chapter 6)

The objectives of this task are to fabricate and characterize hierarchical structure sulfur-infiltrated porous microsphere carbon and apply the materials to lithium-sulfur

batteries cathode. The mechanism of the porous structure for constraining intermediates polysulfide will be studied. Four subtasks will be carried out:

- Porous microsphere carbon with different pore size distribution will be fabricated by adjusting different silica nanoparticle template size or mixing ratio.

- The resulting nanomaterials will be characterized using various techniques, such as scanning electron microscopy (SEM), transmission electron microscopy (TEM), high-resolution TEM (HRTEM), X-ray diffraction (XRD), and thermogravimetric analysis (TGA). And the nanomaterials will be used as cathode materials for lithium-sulfur batteries.

- Electrodes and half-coin cell will be prepared and their performance will be investigated.

- The performance of PMC/S nanomaterials as cathode will be optimized.

CHAPTER 2 CHARACTERIZATION TECHNIQUES

X-ray Diffraction: X-ray diffraction is the primary method for determining the phase and the crystalline structure.

The crystal structures of the powder catalysts were identified by X-ray diffraction (XRD) (Scintag XDS 2000) using Cu Kα irradiation at 45 kV and a diffracted beam monochromator operated at 40 mA in the setting 2θ range at a scan rate of 1 °/min. The crystal size of different crystal phases for TiO_2 was calculated by the Scherrer equation. The fractional phase content, W_A, W_B, and W_R, for anatase, brookite, and rutile, respectively, are mathematically defined in Equations (1), (2) and (3)

$$W_A = \frac{0.886 \times A_A}{(0.886 \times A_A + A_R + 2.721 \times A_B)} \qquad (1)$$

$$W_B = \frac{2.721 \times A_B}{(0.886 \times A_A + A_R + 2.721 \times A_B)} \qquad (2)$$

$$W_R = \frac{A_R}{(0.886 \times A_A + A_R + 2.721 \times A_B)} \qquad (3)$$

where A_A, A_B and A_R represent the integrated intensity of the anatase (1 0 1) peak (2θ = 25.28 °), the brookite (1 2 1) peak (2θ = 30.81 °), and the rutile (1 1 0) peak (2θ = 27.45 °), respectively. Because the brookite (1 2 0) (2θ = 25.34 °) and brookite (1 1 1) (2θ = 25.69 °) peaks overlap with the anatase (1 0 1) peak, A_A and A_B were calculated by the following method. Using the single isolated brookite (1 2 1) peak as a reference, the anatase (1 0 1), brookite (1 2 0) and brookite (1 1 1) overlapped peaks were deconvoluted by 0.9 and 0.8 intensity ratio for $I_{(brookite)}^{(121)}/I_{(brookite)}^{(120)}$ and $I_{(brookite)}^{(111)}/I_{(brookite)}^{(120)}$ respectively, with the same full width at half maximum (FWHM) of brookite (1 2 1).

BET Analysis: The Brunauer, Emmett and Teller (BET) technique is the most common method for determining the surface area of powders and porous materials. Nitrogen gas is

generally employed as the probe molecule and is exposed to a solid under investigation at liquid nitrogen conditions (i.e. 77 K).

The Brunauer-Emmett-Teller (BET) specific surface area and pore size of the catalysts were measured by nitrogen adsorption-desorption isotherms using a Micrometrics ASAP 2020 Surface Area and Porosity Analyzer.

For Ce-TiO$_2$/SiO$_2$ and C/TiO$_2$ materials: Before each adsorption measurement, approximate 0.10 g sample was degassed at 100 ˚C for 18 hours. The BET surface area was determined by a multipoint BET method using the adsorption data in a relative pressure (P/P$_0$) range 0.05-0.3. Pore size distribution was determined via Barret-Joyner-Halender (BJH) method using desorption isotherm. The N$_2$ adsorption volume at the relative pressure of 0.998 was used to determine the total pore volume and average pore size.

For PMC and PMC/S materials: Before each adsorption measurement, 0.10 g PMC sample was degassed at 300 ˚C for 4 h. It is not possible to follow the conventional protocol to degas the PMC/S samples above 155 ˚C before BET measurements owing to the volatility of the sulfur, and thus no pretreatment was done for PMC/S. The pore size distribution plot was derived from the adsorption branch of the isotherm based on the density functional theory (DFT).

XPS Technique: X-ray photoelectron spectroscopy (XPS) is a surface-sensitive quantitative spectroscopic technique that measures the elemental composition at the parts per thousand range, empirical formula, chemical state and electronic state of the elements that exist within a material. XPS spectra are obtained by irradiating a material with a beam of X-rays while simultaneously measuring the kinetic energy and number of electrons that escape from the top 0 to 10 nm of the material being analyzed. XPS requires high vacuum

(P $\sim 10^{-8}$ millibar) or ultra-high vacuum (UHV; P $< 10^{-9}$ millibar) conditions, although a current area of development is ambient-pressure XPS, in which samples are analyzed at pressures of a few tens of millibar.

X-ray photoelectron spectroscopy (XPS) (Perkin-Elmer PHI 5100) was used to examine the valance states of Ce in the Ce/TiO_2 samples before and after CO_2 photoreduction with water vapor. A thin layer of powder samples were loaded on a silicon substrate and subject to XPS analysis. Subsequently, the same samples were exposed to photoillumination in the presence of CO_2 and water vapor for 4 h and then subject to XPS analysis again.

SEM Characterization Technique: A scanning electron microscope (SEM) is a type of electron microscope that produces images of a sample by scanning it with a focused beam of electrons. The electrons interact with atoms in the sample, producing various signals that can be detected and that contain information about the sample's surface topography and composition. The electron beam is generally scanned in a raster scan pattern, and the beam's position is combined with the detected signal to produce an image. SEM can achieve resolution better than 1 nanometer.

Scanning electron microscopy (SEM) equipped with energy-dispersive X-ray (EDX) spectroscopy (Hitachi S4800) was used to analyze the catalyst morphology and surface elemental composition.

TEM Characterization Technique: Transmission electron microscopy (TEM) is a microscopy technique in which a beam of electrons is transmitted through an ultra-thin specimen, interacting with the specimen as it passes through. An image is formed from the interaction of the electrons transmitted through the specimen; the image is magnified

and focused onto an imaging device, such as a fluorescent screen, on a layer of photographic film, or to be detected by a sensor such as a CCD camera.

The particle size and crystal lattice of TiO_2, the particle size of Ag and the pore structure of SBA-15 were analyzed by transmission electron microscopy (TEM) (Hitachi H9000NAR) and high resolution TEM (HR-TEM).

TGA Analysis: Thermogravimetric analysis or thermal gravimetric analysis (TGA) is a method of thermal analysis in which changes in physical and chemical properties of materials are measured as a function of increasing temperature (with constant heating rate), or as a function of time (with constant temperature and/or constant mass loss). TGA is commonly used to determine selected characteristics of materials that exhibit either mass loss or gain due to decomposition, oxidation, or loss of volatiles (such as moisture).

The thermal stability of electrode materials were carried out on a thermalgravimetric analyzer (TGA-DAT-2960 SDT).

For C/TiO$_2$: TGA were carried out at a heating rate of 20 ˚C min^{-1} from 25 to 1000 ˚C in air.

For PMC/S: TGA were carried out at a heating rate of 20 ˚C min^{-1} from 25 to 500 ˚C in argon.

UV-vis reflectance spectra: Ultraviolet–visible spectroscopy or ultraviolet-visible spectrophotometry (UV-Vis or UV/Vis) refers to absorption spectroscopy or reflectance spectroscopy in the ultraviolet-visible spectral region. This means it uses light in the visible and adjacent (near-UV and near-infrared) ranges. The absorption or reflectance in the visible range directly affects the perceived color of the chemicals involved. In this region of the electromagnetic spectrum, molecules undergo electronic transitions.

The UV-vis reflectance spectra were recorded with a UV-vis spectrophotometer (Ocean Optics) using $BaSO_4$ as the background. The reflectance was converted to $F(R)$ using the Kubelka-Munk (K-M) function $[F(R) = (1-R)^2/2R]$, and the band gap energy was obtained from the plot of $[F(R)E_{ph}]^{1/2}$ against the photon energy E_{ph}.

CHAPTER 3   TIO$_2$-BASED PHOTOCATALYSTS FOR SOLAR FUEL PRODUCTION

3.1 Nanostructured Ce-TiO$_2$/SBA-15 Composites for CO$_2$ Photoreduction

According to the literature review results in Chapter 1, we hypothesize that this unique charge separation capacity with the assistance of Ce species could improve CO$_2$ photoreduction with water on TiO$_2$ photocatalysts. SBA-15 as support for Ce-TiO$_2$ will provide sufficient surface area and may have Si-OH group that is beneficial to CO$_2$ photoreduction.

3.2 Materials and Methods

The Ce-TiO$_2$ nanoparticles were synthesized by a sol-gel method. [8, 75] In a typical synthesis process, 10 mL titanium butoxide (Ti(OBu)$_4$, 99%) was ultrasonically dispersed in 40 mL absolute ethyl alcohol for 10 min (Solution A). A certain amount of Ce(NO$_3$)$_3$·6H$_2$O (99.5%) was dissolved in 10 mL H$_2$O, 10 mL absolute ethyl alcohol and 2 mL 62% nitric acid (Solution B). Then Soultion A was added dropwise to Solution B (forming Solution C) with vigorous stirring for 3 h at room temperature. The obtained transparent sol was further aged for 6 h at room temperature, dried at 70 °C for 36 h and finally calcined in a muffle furnace at 500 °C for 2 h. Samples with molar ratios of Ce to Ti at 0.01, 0.03, 0.08 and 0.12 were prepared. For comparison, pristine TiO$_2$ was also prepared without adding the Ce precursor.

SBA-15 was prepared according to a well-established procedure reported by Zhao et. al. [76]   4 g of Pluronic P123 (Aldrich) was dissolved in 125 g of 2 M HCl at 35 °C with stirring. Tetraethyl orthosilicate (TEOS, Aldrich) was then added into the solution after

P123 was dissolved. The resultant solution was stirred for 20 h at 35 ℃, after which the mixture was aged at 80 ℃ for 24 h in a sealed Teflon bottle. The solid product was recovered by filtration and air-dried at room-temperature overnight. SBA-15 was obtained by calcination of the solid product at 500 ℃ for 6 h.

Ce-TiO$_2$ was loaded on SBA-15 by adding SBA-15 particles to Solution C in the sol-gel process of preparing Ce-TiO$_2$ as previously described. The same aging, drying, and calcination procedure was applied. Ce-TiO$_2$/SBA-15 composites with a molar ratio of Ce:Ti:Si at 0.03:1:1, 0.03:1:2, and 0.03:1:4 were prepared. For comparison, Ce-TiO$_2$ loaded on amorphous silica was also prepared following the same procedure, and the amorphous mesoporous silica particles were prepared according to the process reported in our previous study.[5] The prepared samples are denoted as xCe_yTi, xCe_yTi_zSi, and xCe_yTi_z*a*Si, where Ce represents cerium, Ti represents titania, Si represents SBA-15, *a*Si presents amorphous silica, and the numbers of x, y, and z indicate the molar ratio of Ce, Ti, and Si. For example, 0.03Ce_1Ti_4Si represents Ce-TiO$_2$/SBA-15 sample with a Ce:Ti:Si molar ratio at 0.03:1:4.

The Brunauer-Emmett-Teller (BET) specific surface area and pore size of the catalysts were measured by nitrogen adsorption-desorption isotherms using a Micrometrics ASAP 2020 Surface Area and Porosity Analyzer. The crystal structures of the powder catalysts were identified by X-ray diffraction (XRD) (Scintag XDS 2000) using Cu Kα irradiation at 45 kV and a diffracted beam monochromator operated at 40 mA in the 2θ range from 20 ° to 60 ° at a scan rate of 1 °/min. The fractional phase contents of anatase, brookite, and rutile TiO$_2$ were calculated by the method reported in previous work.[11] The Scherrer equation was applied to calculate the crystal size of TiO$_2$. The UV−vis diffuse

reflectance spectra were recorded by a UV–vis spectrophotometer (Ocean Optic) using BaSO$_4$ as the background. Scanning electron microscopy (SEM) (Hitachi S4800) was used to obtain the catalysts surface morphology. The particle size and crystal lattice of TiO$_2$ and the pore structure of SBA-15 were analyzed by transmission electron microscopy (TEM) (Hitachi H9000NAR) and high resolution TEM (HR-TEM).

The photocatalytic activity of CO$_2$ reduction with water vapor was investigated in an experimental system as shown in **Fig. 3.1**. Compressed CO$_2$ (99.999%, Praxair) regulated by a mass flow controller (at a flow rate of 4 mL/min) passed through a deionized water bubbler to introduce CO$_2$ and water vapor mixture (volume fraction of H$_2$O $\approx$ 2.3%) into a photoreactor that has stainless steel walls and a quartz window. For each test, 200 mg powder catalyst was evenly dispersed on a glass-fiber filter and placed in the photoreactor facing the quartz window. A 450 W Xe lamp (Oriel) was used as the irradiation source with a light intensity around 400 mW/cm^2 (UV-vis region), measured by a spectroradiometer (International Light Technologies ILT950). Circulated cooling water was applied to absorb the infrared portion of the Xe lamp irradiation. The photoreactor was operating at a continuous-flow mode and the effluent gas sample was analyzed every 30 min by a gas chromatograph (GC, Agilent 7890A) equipped with an automated gas sampling valve, a thermal conductivity detector (TCD) and flame ionization detector (FID).
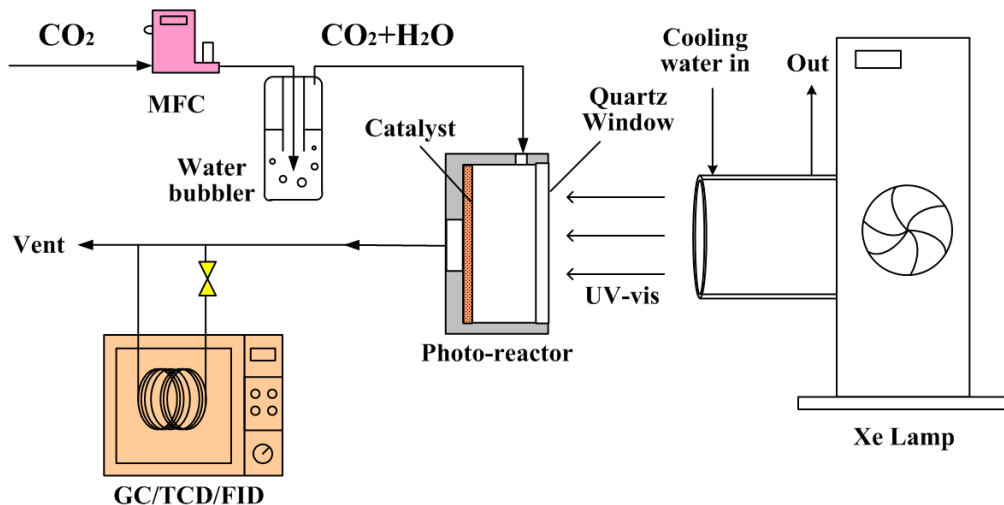
Figure 3.1 Experimental setup for photocatalytic CO_2 reduction with water vapor

3.3 Results and Discussion

Fig. 3.2 shows the XRD patterns of pristine TiO_2 and Ce-TiO_2 nanoparticles with different Ce:Ti molar ratios. The calculated fractional phase contents and crystal sizes of TiO_2 are summarized in **Table 3.1**. Pristine TiO_2 exhibited prominent characteristic peaks for anatase (JCPDS No. 21-1272) and rutile (JCPDS No. 21-1276), as well as a very weak peak for brookite (JCPDS No. 29-1360). It had the highest rutile phase fraction, 53.7%. With the addition of 0.01% Ce, the fraction of rutile phase remarkably decreased to 4.8% with significant increases in anatase and brookite phases. Further increasing the Ce:Ti ratio to 0.03 and 0.08 resulted in the disappearance of the rutile TiO_2. This result is in agreement with the literature reports that even a low concentration of ceria can stabilize the anatase phase and inhibit transformation of anatase to rutile.[77-78] The stabilization mechanism was attributed to the preferential nucleation of ceria on the oxygen vacancies of anatase TiO_2.[77-78] In addition, no obvious peaks corresponding to cubic Ce or cerium oxides were observed in the XRD patterns of Ce-TiO_2, probably due to the low concentration of Ce and the very small particle size of ceria, as well as its well dispersion on the TiO_2 surface.[79]

The diffraction peaks of Ce-TiO$_2$ are broadened compared with pristine TiO$_2$, suggesting smaller crystal size of TiO$_2$ due to Ce addition. As summarized in **Table 3.1**, the average crystal sizes of pristine TiO$_2$ were 17 nm for anatase and 9.5 nm for brookite, and they both decreased with the Ce concentration. It has been reported that dopant in TiO$_2$ favors the formation of smaller crystals.[11, 80]   The smaller Ce-TiO$_2$ size in this work is an indirect evidence that Ce was partially doped in TiO$_2$ lattice. This also contributes to the reason that no Ce or CeO$_2$ peaks were observed in the XRD patterns. **Table 3.1** also shows the BET specific surface area and pore size data. The pristine TiO$_2$ had the lowest surface area at 25.2 m^2/g. The incorporation of Ce in TiO2 dramatically increased the surface are to 136.7 m^2/g for the sample of 0.03Ce_1Ti. This is likely due to the smaller particle size of 0.03Ce_1Ti as previously mentioned.

Table 3.1 Fractional phase content, crystal size, BET specific surface area and pore size of TiO$_2$, SBA-15, Ce-TiO$_2$, Ce-TiO$_2$/SBA-15 and Ce-TiO$_2$/aSiO$_2$ samples

Samples	Phase Content (%)			Crystal Size (nm)			S$_{BET}$ (m^2/g)	Pore Size (nm)
	A	B	R	A	B	R		
TiO$_2$	34.5	11.7	53.7	17	9.5	10.3	25.2	4.6
0.01Ce_1Ti	66.3	28.9	4.8	7.6	7.2	9.9	139.9	5.6
0.03Ce_1Ti	71.5	28.5	0	5.7	5.2	-	136.7	5.5
0.08Ce_1Ti	100	0	0	3.6	-	-	179.0	4.5
SBA-15	-	-	-	-	-	-	871.9	5.3
0.03Ce_1Ti_1Si	100	0	0	-	-	-	334.2	4.1
0.03Ce_1Ti_2Si	100	0	0	-	-	-	509.7	4.4
0.03Ce_1Ti_4Si	100	0	0	-	-	-	443.3	4.7
0.03Ce_1Ti_4aSi	-	-	-	-	-	-	374.4	6.3
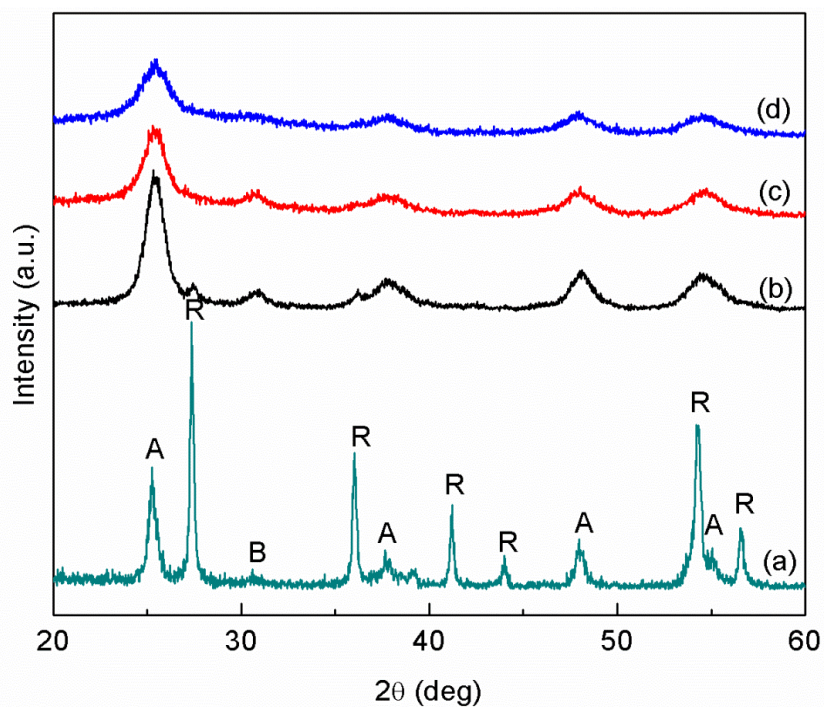
Figure 3.2 XRD patterns of pristine TiO_2 and Ce-TiO_2 samples with different Ce/Ti molar ratios: (a) pristine TiO_2; (b) 0.01Ce_1Ti; (c) 0.03Ce_1Ti; and (d) 0.08Ce_1Ti.   (A: Anatase; B: Brookite; R: Rutile)
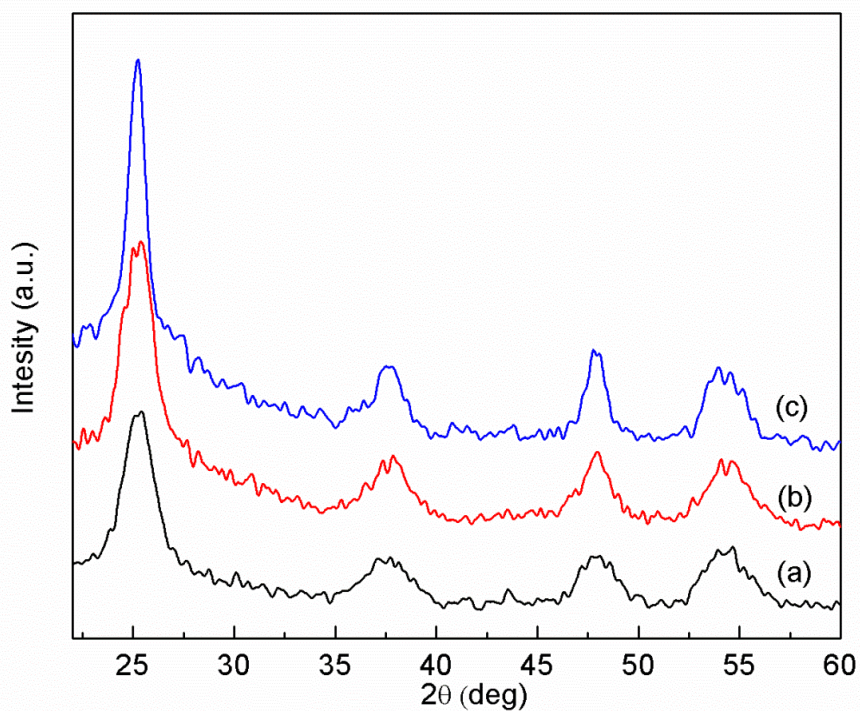
Figure 3.3 XRD patterns of Ce-TiO2/SBA-15 samples with different Ti:Si molar ratios: (a) 0.03Ce_1Ti_1Si; (b) 0.03Ce_1Ti_2Si; and (c) 0.03Ce_1Ti_4Si.

Fig. 3.3 shows the XRD patterns of Ce-TiO$_2$/SBA-15 samples. Only anatase TiO$_2$ diffraction peaks were observed and the noisy background was due to the silica substrate. The specific surface area was significantly increased due to the presence of SBA-15. It is interesting to find that the 0.03Ce_1Ti_4Si sample had a slightly smaller surface area than that of 0.03Ce_1Ti_2Si, considering more SBA-15 was in the 0.03Ce_1Ti_4Si sample. It may be because that the Ce-TiO$_2$ particles were better dispersed on the 0.03Ce_1Ti_4Si sample and partially blocked the pores of SBA-15, resulting in a smaller surface area.

N$_2$ adsorption-desorption was applied to explore the textual property of Ce-TiO$_2$ and Ce-TiO$_2$/SBA-15 catalysts. As shown in **Fig. 3.4**, compared to bare TiO$_2$, Ce-TiO$_2$ samples showed the typical type IV adsorption-desorption isotherms with a relatively wide H$_1$ hysteresis loop, an indicative of mesoporous structure. This mesopore may be resulted from the inter-space of aggregated nanoparticles. With Ce concentration increasing in Ce-TiO$_2$, the specific surface area is also increasing. It may be because that the Ce addition can help decrease particle size which leads to a higher specific surface area. Ce-TiO$_2$ samples showed the similar narrow BJH pore-size distribution with average pore diameter about 4-6 nm.
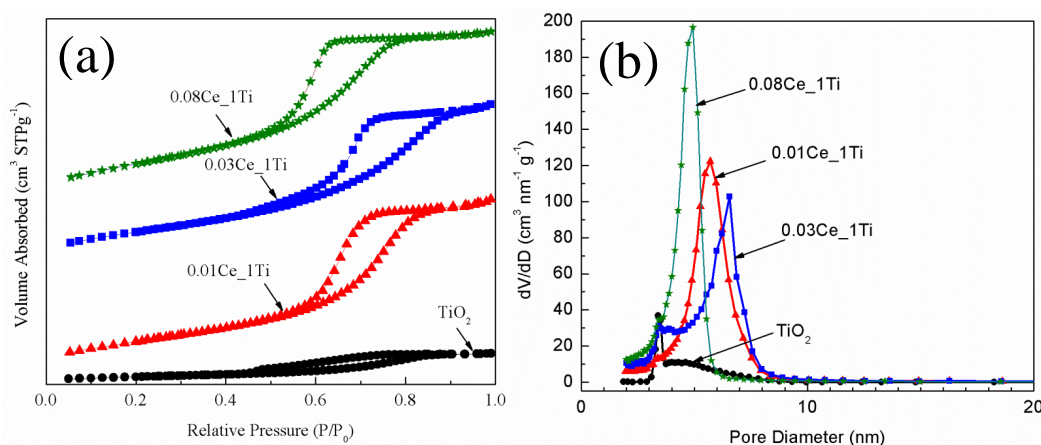
Figure 3.4 N$_2$ adsorption-desorption isotherms (a) and BJH pore size distributions (b) of TiO$_2$ and Ce/TiO$_2$ samples.
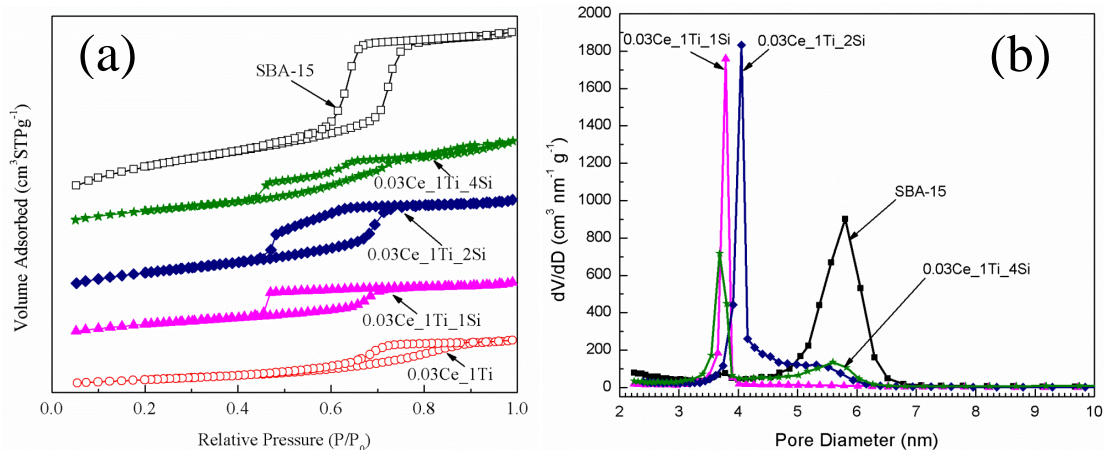
Figure 3.5 N_2 adsorption-desorption isotherms (a) and BJH pore size distributions (b) of SBA-15 and Ce-TiO2/SBA-15 samples.

　　Fig. 3.5 shows the N2 adsorption-desorption isotherms and BJH pore size distribution of SBA-15 and Ce-TiO$_2$/SBA-15 samples. SBA-15 and Ce-TiO$_2$/SBA-15 sample exhibits the typical type IV adsorption-desorption isotherm with a large H$_2$ hysteresis loops. However, the H$_2$ hysteresis loop in the P/P$_o$ on pure SBA-15 ranges from 0.55 to 0.80, while that of Ce-TiO$_2$/SBA-15 is from 0.45 to 0.70, which suggest that Ce-TiO$_2$/SBA-15 samples have large uniform mesopores without changing the pore frame of SBA-15. The different P/P$_o$ positions of the inflection points between SBA-15 and Ce-TiO$_2$/SBA-15 indicate their different pore widths in the mesopore rage. As evidenced in **Fig. 3.5b**, SBA-15 shows a narrow pore size distribution with the diameter of 5.3 nm. In contrast, Ce-TiO$_2$/SBA-15 photocatalysts display a lower pore size distribution around 4.1-4.7 nm. This narrow is probably resulted from the interaction between Ce-TiO$_2$ and SBA-15 that may block some pore openings. Interestingly, 0.03Ce_1Ti_4Si displays two pore size distribution at 3.6 nm and 5.5 nm. This could be resulted from the Ce-TiO$_2$ particles filling into SBA-15 pores and also the pores between the disordered Ce-TiO2 particles on the surface of SBA-15.
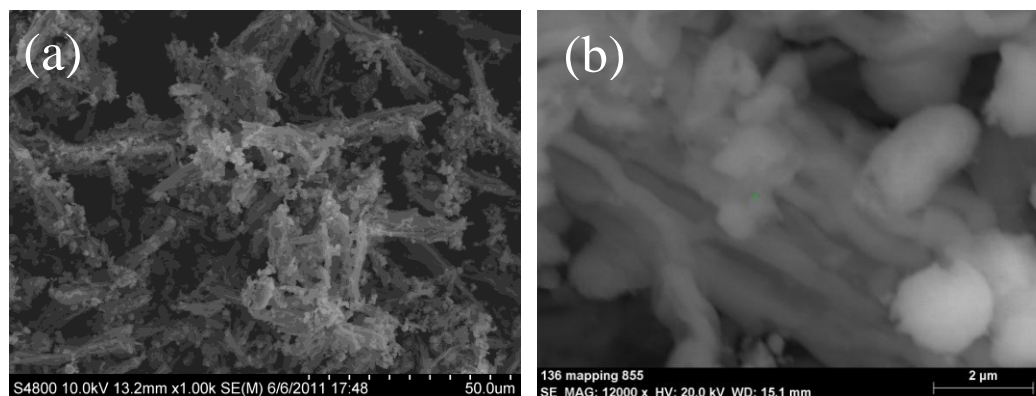
Figure 3.6 SEM images of the 0.03Ce_1Ti_4Si sample.

Detailed morphological information of the Ce-TiO$_2$/SBA-15 sample (0.03Ce_1Ti_4Si) was examined by SEM and TEM. The SEM images in **Fig. 3.6** demonstrate micrometer size particles with irregular shapes mainly in rods and spheres, which are assigned to SBA-15 particles. The TiO$_2$ nanoparticles are not discernible in the SEM images but are clearly shown in the TEM images in **Fig. 3.7**. **Fig. 3.7a-b** demonstrates the morphology of bare SBA-15 samples, where one-dimensional channels of ordered pores are clearly identified. The pore opening is around 8 nm, consistent with the pore size analysis data shown in **Fig. 3.5**. **Fig. 3.7c** demonstrates that for the Ce-TiO$_2$/SBA-15 sample, the TiO$_2$ nanoparticles are dispersed on the surface, at the edge, and possibly in the pores of the SBA-15 support. The fraction of TiO$_2$ nanoparticles embedded in the pores of SBA-15 may be very small, but it may increase as the SBA-15 loading increases. These embedded particles may block a portion of the pores, which explains why the measured specific surface area of the 0.03Ce_1Ti_4Si sample is smaller than that of the 0.03Ce_1Ti_2Si sample (see **Table 3.1**). Aggregates of TiO$_2$ nanoparticles on the outer surface of SBA-15 were also identified, as shown in **Fig. 3.7d**. The TiO$_2$ crystal size is around 5 nm, as shown in the HR-TEM image in **Fig. 3.7e**, which matches the calculated crystal size listed in **Table 3.1** for 3%Ce-TiO$_2$ sample. Clear lattice fringes of nanocrystal

with an interplanar space of 0.350 nm were observed, which corresponds to the (101) plane of anatase TiO_2.[81]
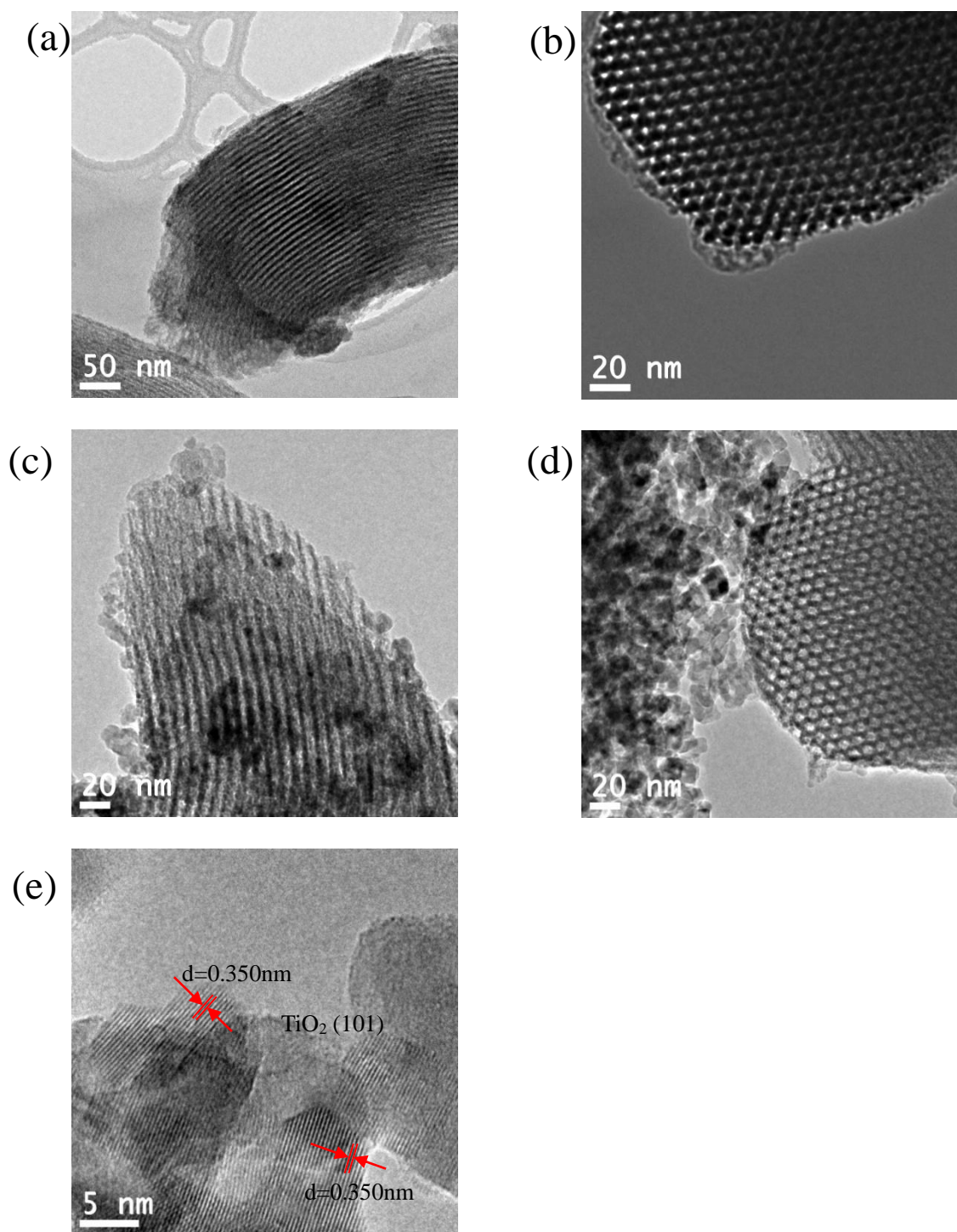
Figure 3.7 TEM and HRTEM images of SBA-15 (a,b) and 0.03Ce_1Ti_4Si (c,d,e) samples.

Diffuse reflectance UV-vis spectra were recorded to explore the influence of Ce and

SBA-15 addition on the optical property of TiO$_2$. As shown in **Fig. 3.8a**, pristine TiO$_2$ absorbs light at wavelength shorter than 400 nm, corresponding to a band gap about 3.0 eV. Incorporation of Ce in TiO$_2$ resulted in a red-shift in the absorption edge, extending to the visible light region in the range of 400 ~ 500 nm. The red-shift was enhanced at an increased Ce concentration, but the enhancement was not significant when the Ce concentration exceeded 3%. **Fig. 3.8b** shows the UV-vis spectra of Ce-TiO$_2$/SBA-15 samples. In contrast to the red-shift effect brought by the Ce doping, the incorporation of SBA-15 as the support resulted in a blue-shift of the absorption spectra, which is signified at a higher SBA-15 loading. This result is in agreement with the literature that a blue shift of light absorption edge of TiO$_2$/SBA-15 has been observed compared with pure anatase TiO$_2$ or P25,[82-84] probably due to the quantum size effect of smaller TiO$_2$ nanocrystals in the SBA-15 matrix.[85]
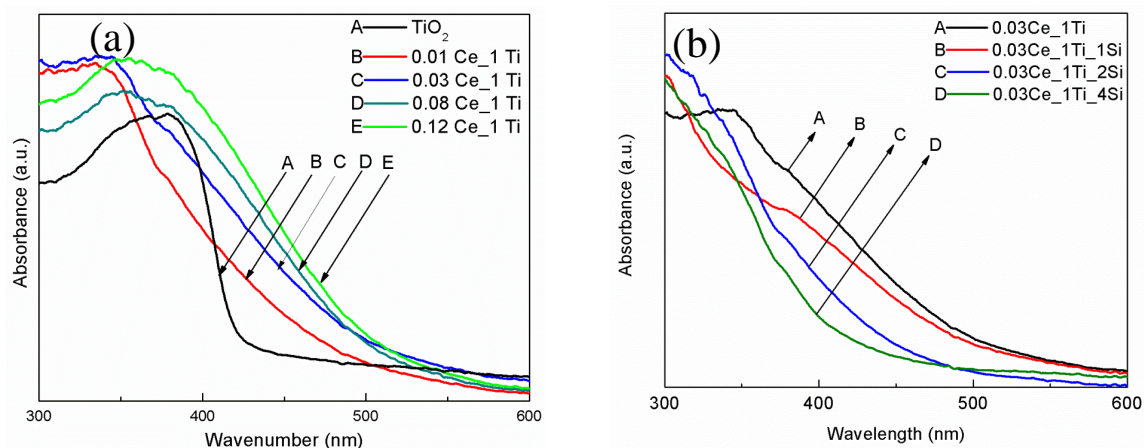
Figure 3.8 UV–vis diffuse reflectance spectra of TiO$_2$ and Ce-TiO$_2$ with different Ce:Ti molar ratios (a) and Ce-TiO$_2$/SBA-15 with different Ti:Si molar ratios (b).

The results of XPS for the 0.03Ce_1Ti sample are shown in **Fig. 3.9**. The energy interval between approximately 882 eV and 903 eV was attributed by Ce 3d 5/2, while the Ce 3d 3/2 was at the 905 eV to 918 eV interval. To perform quantitative analysis, the

background was first subtracted using Shirley approximation function in Augerscan software, and then the 3d 3/2 and 3d 5/2 peak structures were fitted. There were in total 10 peaks fitted for the XPS spectrum between 870 and 920 eV, where Ce^{4+} (CeO_2) has six peaks (#5 – 10) for the total 3d lines due to strong hybridization of the oxygen 2p valence band with the Ce 4f orbital, while Ce^{3+} (Ce_2O_3) has four peaks (#1 – 4).[86] Relative ratio/concentrations of Ce^{3+}/Ce^{4+} were calculated based on the summation of the corresponding peak areas, which gives a Ce^{3+}/Ce^{4+} ratio equal to 55.3%/44.7% before photoreaction and 49.5%/50.5% after photoreaction. The same analysis was done for the 0.08Ce_1Ti sample (XPS spectra not shown here), and the Ce^{3+}/Ce^{4+} ratio was 51.8%/48.2% before photoreaction and 52.7%/47.2% after photoreaction. These results indicate that the Ce^{3+}/Ce^{4+} ratios were similar for the different Ce/TiO_2 samples and almost did not change during the CO_2 photoreduction process.
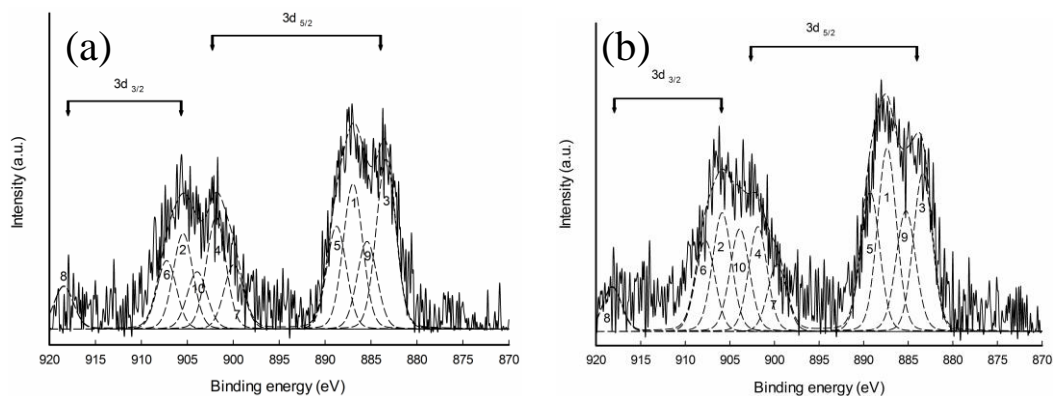
Figure 3.9 XPS spectra of Ce 3d of the 0.03Ce_1Ti sample before (a) and after (b) CO_2 photocatalytic reduction with water vapor.

In this study, CO and CH_4 were identified as the main products of CO_2 photoreduction with H_2O on $Ce–TiO_2$ and $Ce–TiO_2/SBA$-15 nanocomposites. This was in line with our previous published work[5, 52, 87] that CO and CH_4 are the main products of CO_2 photoreduction with water vapor. **Fig. 3.10** shows the production rates of CO and CH_4 on

selected photocatalysts as a function of photo-illumination time. For all catalysts, the production rates gradually decreased after reaching the maximum values, indicating a gradual deactivation of the catalytic performance. Similar trend in deactivation has been observed in our previous studies[5, 88] and in the literature reports.[89-90] Possible reasons are surface coverage of reaction intermediates or re-oxidation of the reaction products.[89] To better compare the activities of the different photocatalysts, accumulative yields during the 4 h photo-illumination were calculated by integrating the production rate with time. The comparison results are presented as follows.
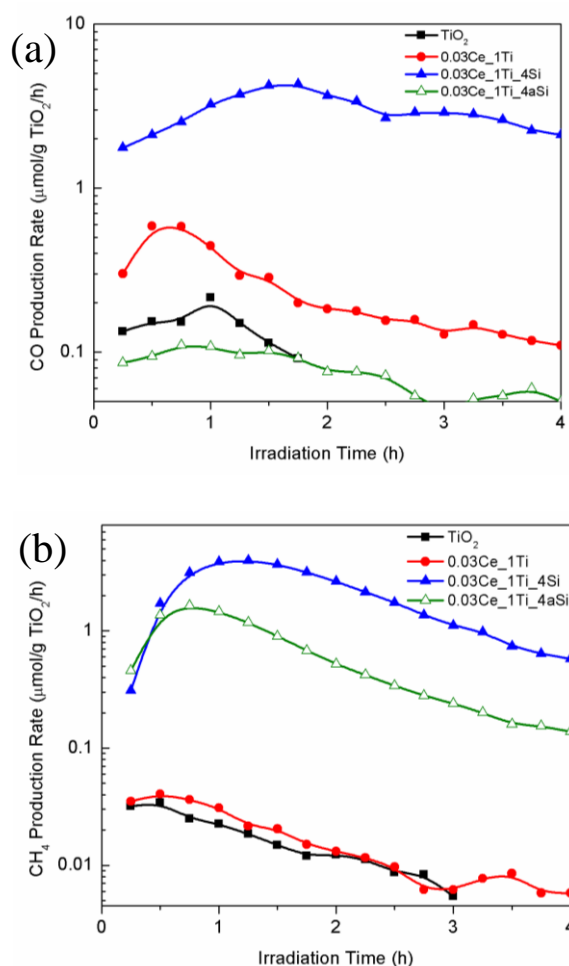
Figure 3.10 Production rate of (a) CO and (b) CH_4 over TiO_2, 0.03Ce_1Ti, 0.03Ce_1Ti_4Si and 0.03Ce_1Ti_4aSi catalysts under UV-vis illumination.
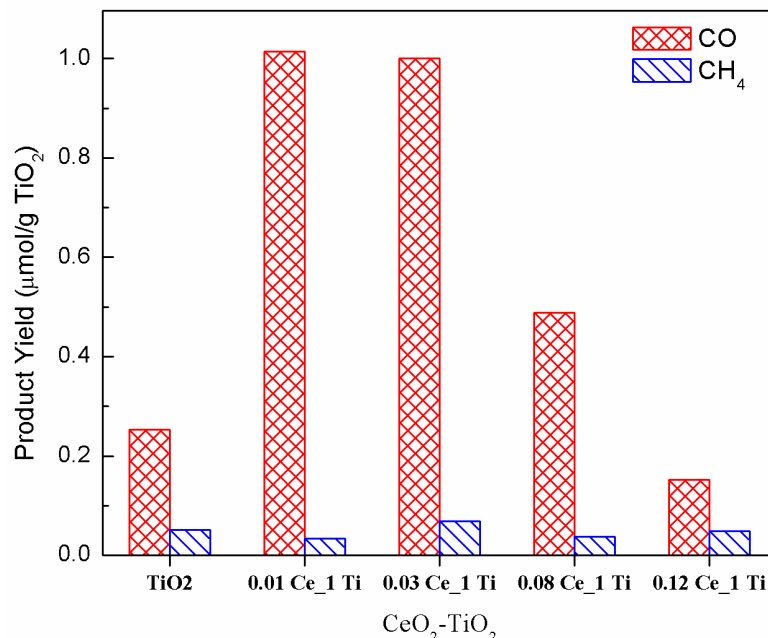
Figure 3.11 Product yields of CO and CH_4 production over TiO_2 and Ce-TiO_2 catalysts under UV-vis illumination for 4 hr.

Fig 3.11 shows the accumulative yields of CO and CH_4 production during a 4 h photo-illumination period using pristine TiO_2 and Ce-TiO_2 samples with different Ce:Ti ratios. Pristine TiO_2 exhibited very low photocatalytic activity, with a CO yield at 0.25 µmol g^{-1} and a CH4 yield at 0.05 µmol g^{-1}. Ce-modification in TiO_2 significantly influenced CO production. At 1% and 3% Ce concentration, the CO yield reached approximately 1.0 µmol g^{-1}, four times as high as the pristine TiO_2. However, further increasing the Ce concentration to 8% resulted in a lower CO yield, and at 12% Ce concentration, the CO yield was even lower than that of pristine TiO_2. The CH_4 yields of all the TiO_2 and Ce-TiO_2 samples remained in the same order and at least one magnitude lower than CO yields, indicating that CH_4 yield was not affected by the Ce addition.

The enhanced CO production due to low concentration Ce-modification on TiO_2 can be attributed to the following reasons. First, Ce-dopant decreased the crystal size of TiO_2 and increased the surface area, as shown in **Table 3.1**, thus enhancing the catalytic

activity. Second, Ce-dopant inhibited the transformation of anatase to rutile phase and promoted the growth of both anatase and brookite phases, as shown in **Table 3.1**. It is well known that anatase TiO_2 is photocatalytically more active than rutile, but a mixture of the two phases can be advantageous. The above results indicate that a binary anatase-brookite with dominating anatase phase at low Ce concentration could promote CO_2 photoreduction activity.

Another important reason for the enhanced activity may be related to the Ce^{3+}/Ce^{4+} redox couple on TiO_2 that facilitates electron-hole separation. It is well known that Ce^{4+} ions can trap photo-excited electrons at the CeO_2/TiO_2 interface through reaction (1).[7, 36, 38, 91] The Ce^{3+} ions can then react with gas-phase O_2, if any (reaction (2)) to regenerate Ce^{4+},[35, 91] or react with CO_2 (reaction (3)) in the case of this study, to form surface adsorbed CO_2^- that can be further reduced to CO (reaction (4)). The formation of CO_2^- species as CO_2 reduction intermediates has been confirmed by our previous in situ DRIFTS study using Cu/TiO_2 catalysts.[88] Hence, the presence of Ce^{4+} enhanced electron trapping and transfer to CO_2.

$$e^- + Ce^{4+} \longrightarrow Ce^{3+} \tag{1}$$

$$Ce^{3+} + O_2 \longrightarrow Ce^{4+} + O_2^- \tag{2}$$

$$Ce^{3+} + CO_2 \longrightarrow Ce^{4+} + CO_2^- \tag{3}$$

$$CO_2^- + e^- \longrightarrow CO + O_2^- \tag{4}$$

$$Ce^{3+} + h^+ \longrightarrow Ce^{4+} \tag{5}$$
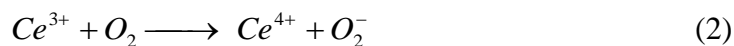
On the other hand, it is possible that Ce^{3+} ions can be directly oxidized back to Ce^{4+} by photo-excited holes, according to reaction (5),[7] which may diminish the promoting

effect of electron transfer as described above. However, the pre-existing Ce^{3+} ions on the TiO_2, in the case of Ce-TiO_2 samples prepared in this work, can provide abundant Ce^{3+} sites to promote reaction (3). Furthermore, the hole trapping effect of Ce^{3+} can also prevent holes from re-oxidizing the reaction product (i.e., CO) back to CO_2. Therefore, the Ce^{3+}/Ce^{4+} redox couples are advantageous over Ce^{4+} or Ce^{3+} alone to promote charge separation and enhance CO_2 photoreduction. The XPS result that the Ce^{3+}/Ce^{4+} ratio almost did not change during the photo-reaction was another evidence for the abovementioned Ce^{3+}/Ce^{4+} redox reactions that remained at a dynamic equilibrium.

In this set of experiments, a fixed amount of 200 mg Ce-TiO_2/SBA-15 was used for each test, while the Ce concentration relative to TiO_2 remained the same at 3% and the Ti:Si ratio varied from 1 to 4. Compared with the bare Ce-TiO_2 sample, dispersing the Ce-TiO_2 nanoparticles on the SBA-15 matrix resulted in a significant enhancement in the yields of CO and CH_4 production, as shown in **Fig. 3.12**. The enhancement seemed to be proportional to the loading of SBA-15 used. Among the three Ce-TiO_2/SBA-15 samples tested, the sample with the highest SBA-15 loading, 0.03Ce_1Ti_4Si, showed the highest activity for both CO and CH_4 production, reaching 7.5 and 7.9 μmol g^{-1}, respectively. Compared with the 0.03Ce_1Ti sample, the 0.03Ce_1Ti_4Si sample demonstrated 8-fold enhancement in CO production and 115-fold enhancement in CH_4 production.
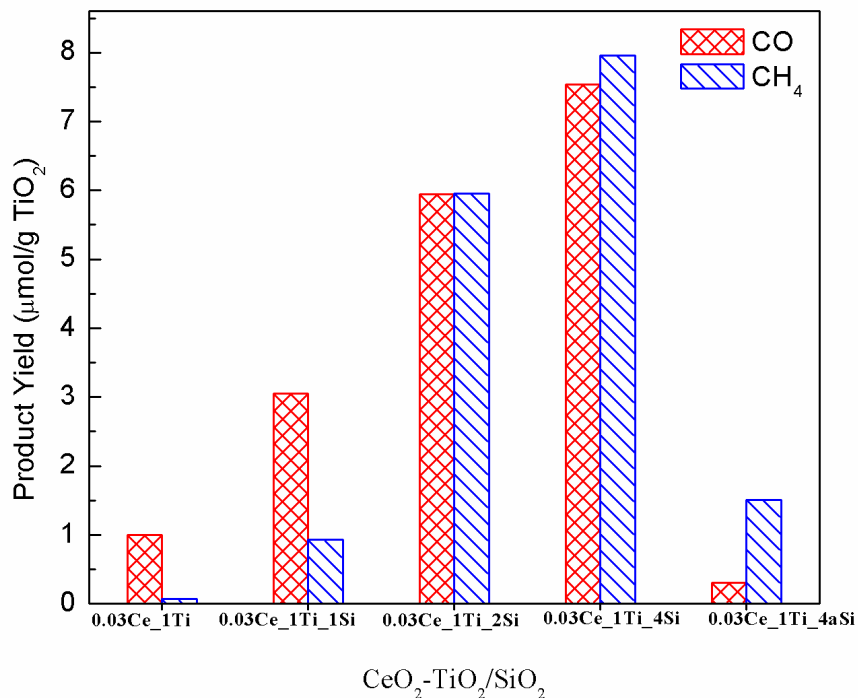
Figure 3.12 Product yields of CO and CH$_4$ production over Ce-TiO$_2$/SBA-15 and Ce-TiO$_2$/aSiO$_2$ catalysts under UV-vis illumination for 4 hr.

This superior activity of SBA-15 supported Ce-TiO$_2$ catalysts is believed to be mainly attributed to the higher surface area and better dispersion of the Ce-TiO$_2$ nanoparticles, as verified by the BET and TEM analyses. Moreover, SBA-15 as the support may enhance the stability of the TiO$_2$ anatase phase and prevent the grain growth of TiO$_2$ nanocrystals.[92]   This mechanism was also supported by our XRD results that 100% anatase TiO$_2$ was present in Ce-TiO$_2$/SBA-15 samples and supported by our UV-vis DRS results that smaller TiO$_2$ nanopartricles were present due to the SBA-15 confinement effect leading to a blue-shift in light absorption. In addition, mesoporous silica is also a well-known CO$_2$ adsorbent that may increase the localized concentration of CO$_2$ near the surface of TiO$_2$, and thus improve CO$_2$ adsorption on TiO$_2$ and subsequent reduction. In a recent study by Yang et al. [47]   an enhanced photocatalytic CO$_2$ reduction was observed on a 2%Cu-TiO$_2$/SBA-15 sample (45 wt% TiO$_2$ loading) compared with 2%Cu-TiO$_2$; however,

the enhancement due to the SBA-15 support was only 20%. In our work, the enhancement factor was much more significant on Ce-TiO$_2$/SBA-15, suggesting the superior effect of Ce addition. Furthermore, the dramatic 115-fold enhancement in CH$_4$ production observed in this study is very intriguing. Because eight protons are needed for generation of one CH$_4$ molecule in comparison with two electrons for CO generation, the surface Si-OH groups or active OH sites due to the presence of SBA-15 may be more readily available for CO$_2$ reduction and conversion to CH$_4$. Investigations on this high CH$_4$ selectivity as well as the potential synergies between the Ce species, TiO$_2$ and the SBA-15 support are in our future research plan.

Another important finding in this study was that Ce-TiO$_2$ dispersed on SBA-15 was much more active than that dispersed on amorphous mesoporous silica. As shown in **Fig. 3.12**, the CO yield on the amorphous silica supported sample, 0.03Ce_1Ti_4*a*Si was very small, even lower than the catalyst without silica support. The CH$_4$ yield of 0.03Ce_1Ti_4*a*Si was 1.5 μmol g^{-1}, higher than the catalyst without silica support but still much lower than the catalyst supported on SBA-15. The overall CO$_2$ reduction rate to CO and CH$_4$ was more than 10 times higher on 0.03Ce_1Ti_4Si than on 0.03Ce_1Ti_4*a*Si. Since the specific surface area of the 0.03Ce_1Ti_4Si sample was only about twice as much as that of the 0.03Ce_1Ti_4*a*Si sample (**Table 3.1**), the much higher activity of the SBA-15 supported sample should result from other factors besides the surface area effect.

The possible reason is that ordered pores of SBA-15 are pores accessible to TiO$_2$ precursors during the preparation process, leading to a better dispersion of TiO$_2$ nanoparticles. Amorphous silica with random arrays of pores and shapes in some cases are

poor supports for functional agents because not all the volume of irregular pores is accessible to the incorporated species.[93]

3.4 Conclusion

A novel Ce-TiO$_2$/SBA-15 nanocomposite was synthesized for the first time in the literature and tested as a photocatalyst for converting CO$_2$ and H$_2$O to fuels such as CO and CH$_4$ under photo-illumination. Modification of TiO$_2$ with Ce significantly stabilized the TiO$_2$ anatase phase and increased the specific surface area, which contributed to an improvement of CO production from CO$_2$ reduction. Dispersing Ce-TiO$_2$ nanoparticles on the mesoporous SBA-15 support further enhanced both CO and CH$_4$ production. Particularly the CH$_4$ production was enhanced by up to 115 times compared with unsupported Ce-TiO$_2$. The superior catalytic activity may be related to the partially embedded Ce-TiO$_2$ nanoparticles in the ordered 1-D pores in SBA-15 that form synergies between the different components of the catalysts and enhance the diffusion and adsorption of CO$_2$. This mechanism also correlates well the results that using SBA-15 as the support led to more than 10 times higher activity in CO$_2$ photoreduction than using amorphous silica as the support.

CHAPTER 4   AG/TIO$_2$ NANOCOMPOSITE   PHOTOCATALYSTS FOR SIMULTANEOUS H$_2$ PRODUCTION AND CO$_2$ REDUCTION

4.1 Introduction

As shown in **Fig. 1.5**, both photocatalytic H$_2$ production and CO$_2$ reduction using water as the reductant processes could occur concurrently and compete with each other for photo-induced electrons. However, the benefit of having both reactions in one system is the possibility of producing syngas, a mixture of H$_2$ and CO, which is a valuable feedstock in producing synthetic petroleum through Fischer-Tropsch process. According to the literature review, the first objective of this work was to explore the feasibility of syngas production from CO$_2$ and water vapor through a photocatalytic process using a silver-modified TiO$_2$ (Ag/TiO$_2$) nanoparticle catalyst. Ag was selected because it is much less expensive than Pt and Ag/TiO$_2$ has shown effectiveness in H$_2$ production [53] and CO$_2$ photoreduction [48] in separate studies.

Another unique feature of this work is the method of preparing the Ag/TiO$_2$ catalyst using a simple ultrasonic spray pyrolysis (USP) process. Conventional preparation methods for Ag/TiO$_2$ catalysts include sol-gel [48, 53, 94] and wet impregnation, [95] which are batch processes and require several after-treatment steps. USP offers several advantages over conventional material processing techniques, including a narrow particle size distribution and a high purity of the product powder. [96-98]

Among the limited number of publications, no studies have been investigated on USP synthesized Ag/TiO$_2$ catalysts for simultaneous H$_2$ production and CO$_2$ reduction. Therefore, the second objective of this work was to explore the potential advantages of

USP synthesis of Ag/TiO$_2$ catalysts over conventional wet-impregnation method with regard to material property and catalytic activity.

4.2 Materials and Methods

The apparatus for ultrasonic spray pyrolysis process and the formation mechanism of Ag/TiO$_2$ nanoparticle composites are shown in **Fig. 4.1**. The spraying solution was prepared by mixing aqueous AgNO$_3$ solution and TiO$_2$ (Degussa P25) nanoparticles. The TiO$_2$ concentration was fixed at 16 mg/ml and the amount of AgNO$_3$ was varied so that the nominal weight percentage of Ag to TiO$_2$ in the catalysts was in the range of 1%-8%. The ultrasonic nebulizer (Sonaer) has a frequency of 2.4 MHz and produces droplets with a volumetric mean diameter of 1.8 mm. The generated mists containing AgNO$_3$/TiO$_2$ were carried out by N$_2$ and passed through a diffusion dryer composed of silica gels. The particles then passed through a cylindrical quartz reactor that was placed inside a tube furnace (Thermo Fisher) with a set temperature of 550 °C. The spray-pyrolyzed particles were collected on a glass fiber filter placed inside a stainless-steel filter holder. As a control, Ag modified TiO$_2$ samples with the same nominal Ag weight percentages were also synthesized by a benchmark wet-impregnation method by mixing and stirring desired amount of TiO$_2$ (P25) in AgNO$_3$ aqueous solution at 80 °C overnight and finally calcining the sample in air environment at 400 °C for 4 h. To have a comparable basis for material property, the spray pyrolysis samples were also calcined in air at 400 °C for 4 h as a final step. The samples were denoted as m%Ag/TiO$_2$-SP or m%Ag/TiO$_2$-WI, where m represents the nominal Ag weight percentage, SP represents materials prepared by spray pyrolysis method, and WI represents materials prepared by wet impregnation method.
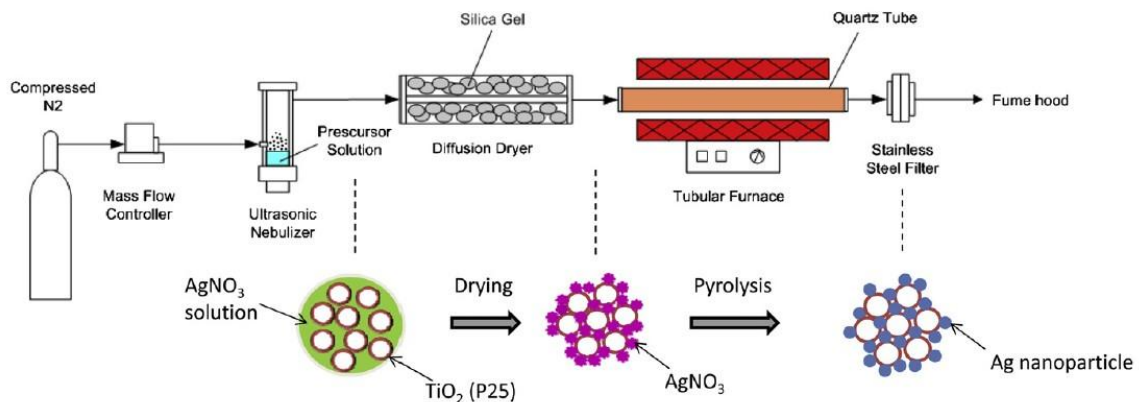
Figure 4.1 Schematic diagram of the ultrasonic spray pyrolysis process and the formation of Ag/TiO$_2$ nanoparticle composites.

The Brunauere-Emmette-Teller (BET) specific surface area of the catalysts was measured by nitrogen adsorption using a surface area and porosity analyzer (Micrometrics ASAP2020). The crystal structures of the catalysts were identified by X-ray diffraction (XRD) (Scintag XDS 2000) using Cu Ka irradiation at 45 kV and a diffracted beam monochromator operated at 40 mA in the 2θ range from 20° to 80° at a scan rate of 2°/min. The UV-vis reflectance spectra were recorded with a UV-vis spectrophotometer (Ocean Optics) using BaSO$_4$ as the background. The reflectance was converted to F(R) using the Kubelka-Munk (K-M) function [F(R)= (1-R)^2/2R], and the band gap energy was obtained from the plot of [F(R)E$_{ph}$]$^{1/2}$ against the photon energy E$_{ph}$.[87] Scanning electron microscopy (SEM) equipped with energy-dispersive X-ray (EDX) spectroscopy (Hitachi S4800) was used to analyze the catalyst morphology and surface elemental composition. Transmission electron microscopy (TEM, Hitachi H9000NAR) and high-resolution TEM were used to examine the particle size and dispersion of Ag nanoparticles on TiO$_2$ as well as the lattice information.

The schematic of the photocatalytic reaction system is illustrated in **Fig. 4.2**. Compressed N$_2$ (99.998%, Praxair) or CO$_2$ (99.999%, Praxair) was used as the carrier gas

for measuring the catalytic activity of H_2 production or CO_2 reduction, respectively. The carrier gas regulated by a mass flow controller passed through a bubbler containing 5 vol% methanol in de-ionized water to generate a water-methanol vapor mixture. Methanol was expected to serve as the hole scavenger and thus enhance the rate of reduction by electrons.[87, 99-100] Estimated from the saturation vapor pressure-temperature profile,[101] the volume fraction of H_2O and CH_3OH in the gas mixture at 20 ˚C was calculated to be 2.2% and 0.6%, respectively, balanced with the carrier gas (N_2 or CO_2). The gas mixture was then introduced into a photoreactor. 100 mg powder catalysts were dispersed on a glass fiber filter and placed at the bottom of the reactor. A 150 W Solar Simulator (Oriel) was used as the photo-excitation source. Before photo-illumination, the reactor was purged with the carrier gas (N_2 or CO_2) at a flow rate of 120 ml/min for 1 h and then at 4 ml/min for 1 h. During the illumination, the carrier gas flow rate maintained at 4 ml/min and the sample of effluent gas was taken every 30 min by an automated valve to a gas chromatograph (GC, Agilent 7890A). The GC was equipped with a thermal conductivity detector (TCD) and flame ionization detector (FID).
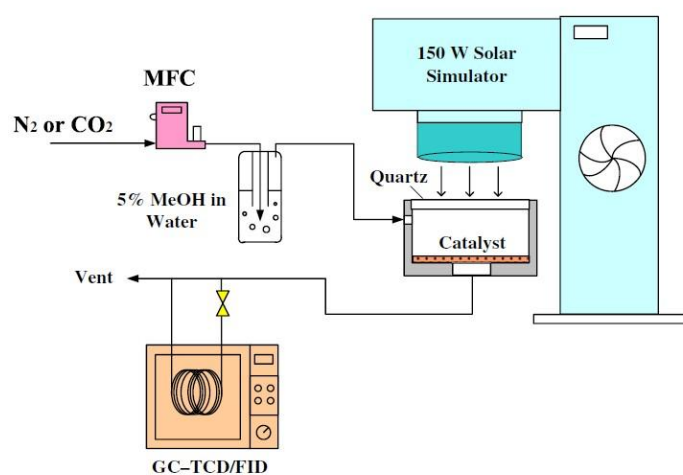
Figure 4.2 Experimental system for photocatalytic H_2 production and/or CO_2 reduction.

4.3 Results and Discussion

Fig. 4.3 compares the XRD patterns of Ag/TiO$_2$-SP and Ag/TiO$_2$-WI samples. All patterns indicate a mixture of TiO$_2$ anatase and rutile phases, which agrees with the composition of P25 (approximately 80% anatase and 20% rutile). At a lower Ag concentration (i.e., 2%), no diffraction lines of Ag species were observed, suggesting that Ag is well dispersed or the particle size is very small. At a higher Ag concentration (i.e.,8%), the SP sample showed peaks at 2θ = 38.2˚, 44.4˚, 64.5˚ and 77.4˚ that correspond to metallic silver.[53, 102-104] This indicates that Ag ions are thermally reduced during the spray pyrolysis process.[105] In contrast, for the 8% Ag/TiO$_2$-WI sample, neither metallic silver or silver oxides were observed. The result implies that silver oxides could be the major Ag species on WI samples as some literature publications reported the presence of Ag$_2$O in a Ag/TiO$_2$ composite prepared by impregnation[95] without detecting Ag$_2$O diffraction peaks in the XRD patterns.
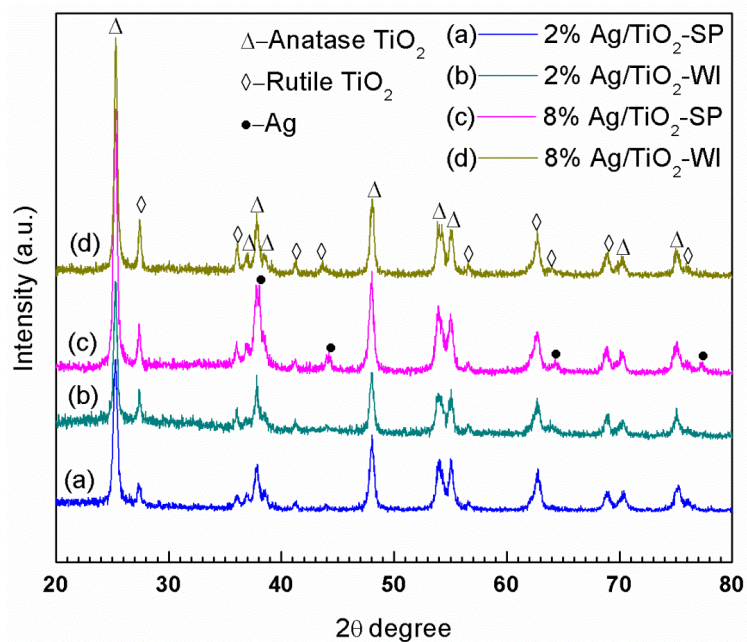
Figure 4.3 XRD patterns of (a) 2% Ag/TiO$_2$-SP, (b) 2% Ag/TiO$_2$-WI, (c)8% Ag/TiO$_2$-SP and (d) 8% Ag/TiO$_2$-WI.

Table 4.1 Comparison of BET and EDX analysis results for 2% Ag/TiO$_2$ samples prepared by SP and WI methods.

Sample	BET Analysis			EDX Elemental Analysis		
	Specific Surface Area (m^2/g)	Pore Volume (cm^3/g)	Pore Size (nm)	Ti (wt.%)	O (wt.%)	Ag (wt.%)
2% Ag/TiO$_2$-SP	54.2	0.34	17.6	56.8	42.0	1.2
2% Ag/TiO$_2$-WI	43.8	0.27	15.5	61.7	36.1	2.2

The textural properties of the Ag/TiO$_2$ samples were characterized by BET, SEM/EDX, and TEM/HRTEM analysis. **Table 4.1** compares the results of BET analysis for the SP and WI samples with the same nominal Ag concentration (i.e., 2%). The SP sample had a larger specific surface area (54.2 m^2/g) compared with the WI sample (43.8 m$_2$/g). The pore volume and average pore size for the SP sample were also larger than those of the WI sample. The results suggest that the spray pyrolysis process may lessen the degree of agglomeration of the TiO$_2$ nanoparticles through the solvent evaporation process, resulting in a larger pore size and a larger surface area. The pore size in the range of 15-18 nm indicate a mesoporous structure for both samples, which is confirmed by the SEM images shown in **Fig. 4.4**. The SP samples (**Fig. 4.4a**) are mesoporous spheres composed of the primary nanoparticles while the WI samples (**Fig. 4.4b**) are irregular-shape agglomerates of the primary nanoparticles. TEM and HRTEM images for the SP and WI samples are shown in **Fig. 4.5**. It is clear that Ag nanoparticles in the size range of 1-2 nm are well dispersed on crystalline TiO$_2$ particles (~20 nm, agreeing with P25 primary particle size) for both SP and WI samples. However, some "big" Ag nanoparticles (~8 nm, see **Fig.**

4.5d) and aggregates of Ag nanoparticles (see **Fig. 4.5e**) were found on the WI sample, indicating that the Ag dispersion on the WI sample was worse than on the SP sample.
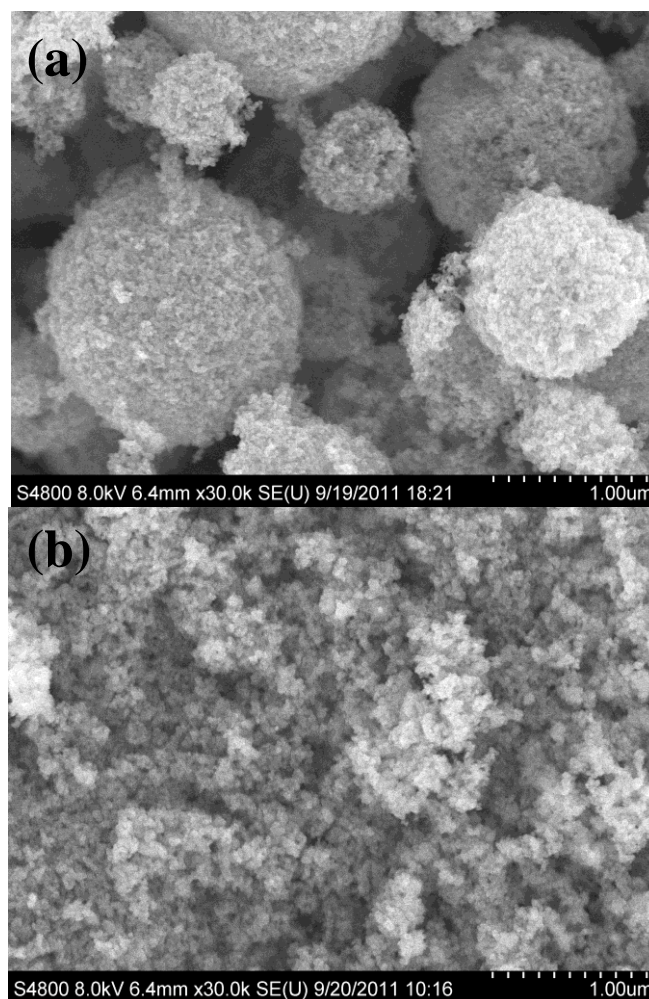
Figure 4.4 SEM images of 2% Ag/TiO$_2$-SP (a) and 2% Ag/TiO$_2$-WI (b).
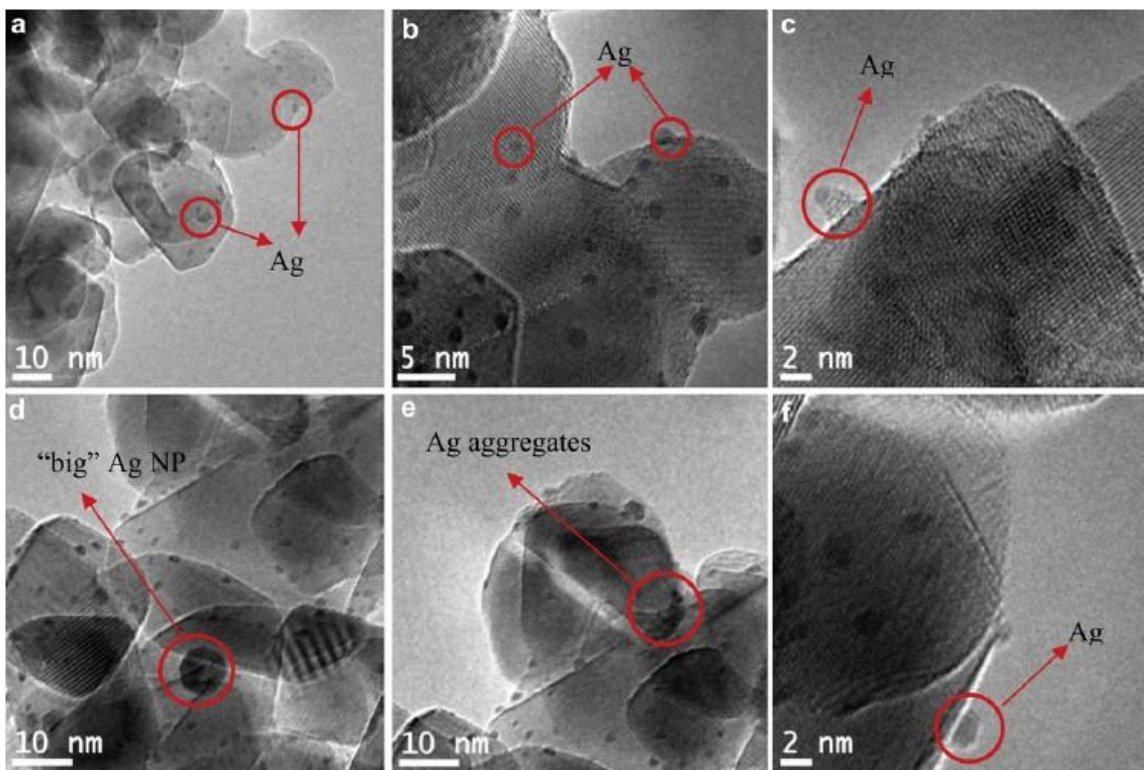
Figure 4.5 TEM images of (a) and (b) 2% Ag/TiO$_2$-SP; (d) and (e) 2% Ag/TiO$_2$-WI and HRTEM images of (c) 2% Ag/TiO$_2$-SP; (f) 2% Ag/TiO$_2$-WI

The EDX elemental analysis data for the 2% Ag/TiO$_2$ samples are listed in **Table 4.1**. A major difference between the SP and WI samples is the measured Ag concentration, although both of them had the same nominal Ag concentration (i.e., 2 wt%) calculated from the precursor composition in the starting solution. For the WI sample, the measured Ag concentration (2.2 wt%) was very close to the nominal concentration, while for the SP sample, the measured Ag concentration was only 1.2 wt%. A possible reason for the lower Ag concentration on SP samples could be that a portion of the Ag nanoparticles formed during the spray pyrolysis escaped from the TiO$_2$ surface along with the solvent evaporation process and these Ag nanoparticles were not collected on the filter due to their extremely small size.

Fig. 4.6 shows the results of band gap analysis derived from the UV-vis diffuse reflectance spectra. Pure TiO_2 P25 has a band gap of 3.20 eV. With incorporation of Ag species, the band gap slightly decreased to 3.0-3.1 eV for SP samples and 2.9-3.0 eV for WI samples. However, the change in band gap is not an apparent function of Ag concentration. The shift of band gap is probably due to the interaction of Ag ions with TiO_2 [95] or formation of impurity band inside the TiO_2 band gap. [106-107] A broad peak around 2.35 eV (or 500-550 nm in absorption spectra) was observed for both SP and WI samples with higher Ag concentration (>4 wt%). This unique peak is an indication of the localized surface plasmon resonance (SPR) of Ag nanoparticles, [95, 108] which again confirms the presence of metallic Ag on TiO_2.
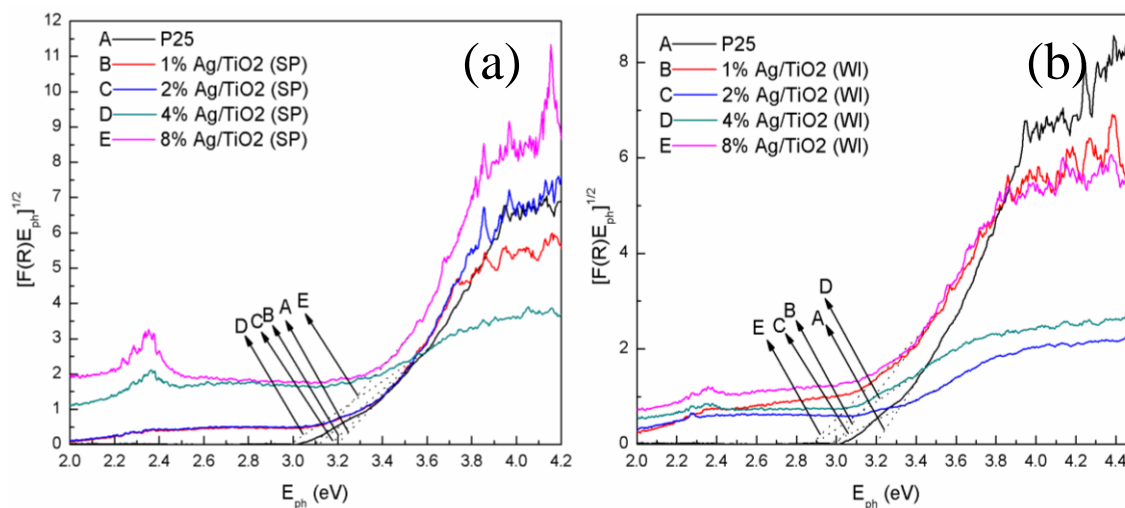
Figure 4.6 Diffuse reflectance spectra of TiO_2, Ag/TiO_2 (a) prepared by ultrasonic spray pyrolysis (b) prepared by wet impregnation.

The experiments of photocatalytic hydrogen production were carried out by using N_2 as the carrier gas to bubble through the methanol/water mixture. Since the reactor was running in a continuous-flow mode, the H_2 production rate gradually increased and reached a steady value after approximately 4 h of photo-illumination (the curves of H_2 production

rate with illumination time are not shown here). **Fig. 4.7** summarizes the steady-state H_2 production rate for SP and WI samples with different Ag concentrations. For bare TiO_2, the H_2 production rate was very small for both SP and WI samples. The incorporation of Ag species significantly enhanced the H_2 production rate. For Ag/TiO_2 samples with Ag concentration greater than 1%, the SP samples were much more active than the WI samples and the optimal Ag concentration appeared to be 2%. For 2% Ag/TiO_2-SP, the H_2 production rate was 1130 mmol/g/h, 6 times as much as that of 2% Ag/TiO_2-WI (180 mmol/g/h), and 60 times as much as that of bare TiO_2-SP (19 mmol/g/h). Ag concentration greater than 2% resulted in a lower H_2 production rate, probably because too high a metal concentration on TiO_2 leads to the formation of electron-hole recombination centers. [5]
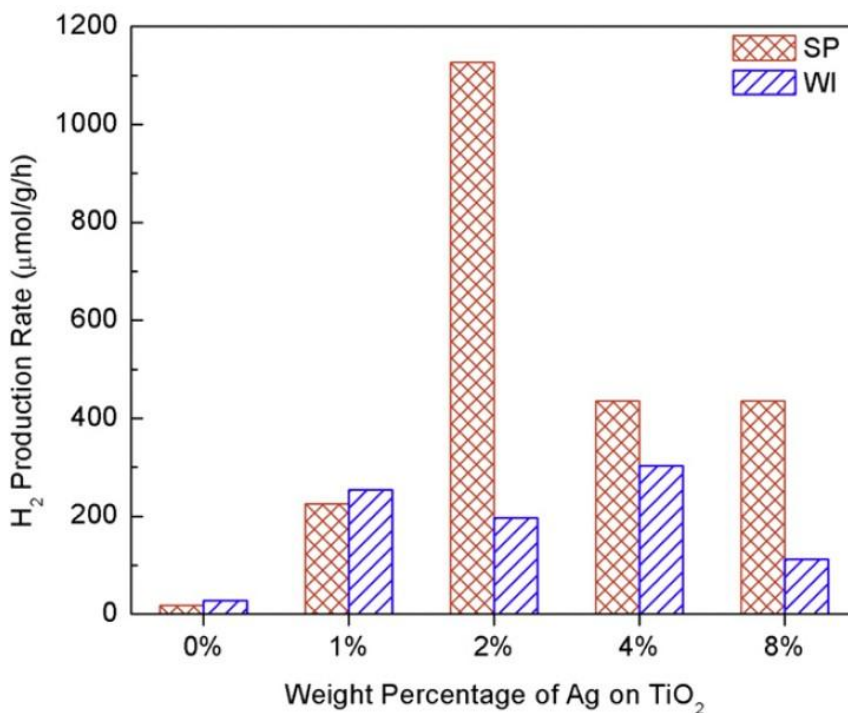
Figure 4.7 Rates of photocatalytic H_2 production for Ag/TiO_2-SP and Ag/TiO_2-WI samples at different Ag concentration (the reaction gas was a mixture of 2.2% H_2O and 0.6% CH_3OH balanced with N_2).

The H_2 production rate of the 2% Ag/TiO_2-SP was compared with the literature data. Park et al. [53]reported that the H_2 production rate was 8560 mmol/g/h by a Ag/TiO_2(rutile) powder catalyst suspended in a methanol/water (1:1 v/v) solution under 365 nm UV irradiation at an intensity of 36 W/cm^2. The relatively high yield was attributed to the extremely high light intensity. Alenzi N. et al. [100]reported the average H_2 production rate of Ag/TiO_2 (anatase) film was 148 mmol/h/g in a methanol/water (1:1 v/v) solution system (4.7 mmol/h/g if without Ag) under UV irradiation at 10 mW/cm^2. Onsuratoom et al. [99]reported the highest H_2 production rate was 4 $cm^3/g/h$ or 178 mmol/g/h on an optimized Ag/TiO_2-ZrO_2 photocatalyst (Ag = 0.5 wt%) in a methanol/water (1:1 v/v) aqueous system under UV light at 2.3 mW/cm^2. In this work, the H_2 production rate of 2% Ag/TiO_2-SP was 1130 mmol/g/h, with a comparable light intensity of 12.5 mW/cm^2 (for $200 < l < 400$ nm) and a much lower methanol/water ratio (0.6:2.2 v/v). Comparisons with the literature data indicate that the 2% Ag/TiO_2-SP catalyst we synthesized is a very effective photocatalyst toward H_2 production.

The experiments of photocatalytic CO_2 reduction were carried out by using CO_2 as the carrier gas to bubble through the methanol/water mixture. **Fig. 4.8** shows the photocatalytic activity of CO_2 reduction with the same sets of catalysts used in the H_2 production tests. CO was found to be the major product with minor CH_4 production. Like the trend observed for H_2 production, the incorporation of Ag on TiO_2 significantly increased the CO_2 reduction rate and the SP samples generally had higher activity than WI samples. The production rates of both CO and CH_4 were also affected by the Ag concentration. As shown in **Fig. 4.8a** 2% Ag/TiO_2-SP demonstrates the highest CO production rate at 87 mmol/h/g, 50% more than that of 2% Ag/TiO_2-WI (57 mmol/h/g). As

shown in **Fig. 4.8b**, the production rates of CH_4 are one order of magnitude lower than those of CO. Ag/TiO_2-SP samples with a silver concentration in the range of 2-8% had the highest and very close CH_4 production rates at approximately 10 mmol/h/g, more than twice as much as the average rates of WI samples in the range of 2-8% Ag. The production rate of CO was generally one order of magnitude higher than that of CH_4, as shown in **Fig. 4.8**. The selectivity of CO and CH_4 from CO_2 photoreduction, however, has not been well understood in the literature. It has been reported in our previous work [5] that pure TiO_2 favors CO production from CO_2 photoreduction with water vapor, while the selectivity of CH_4 increases if copper species are deposited on TiO_2 surface. The results in this work on Ag-deposited TiO_2 demonstrate the same trend that Ag species promote CH_4 production rate. However, CO is the major product (>90% selectivity) in both this work and our previous work. [5] The reasons that the production rate of CH_4 is much smaller than CO may be: (1) it is more difficult to proceed an eight-electron transfer to generate CH_4 compared with a two-electron process for CO, and (2) CH_4 may be mainly derived from further reduction of CO and thus CH_4 formation rate is limited by that of CO. The deposited metal species on TiO_2 facilitate electron trapping and transport to the catalyst surface, and thus, can potentially enhance multi-electron transfer processes, leading to a higher rate of CH_4.
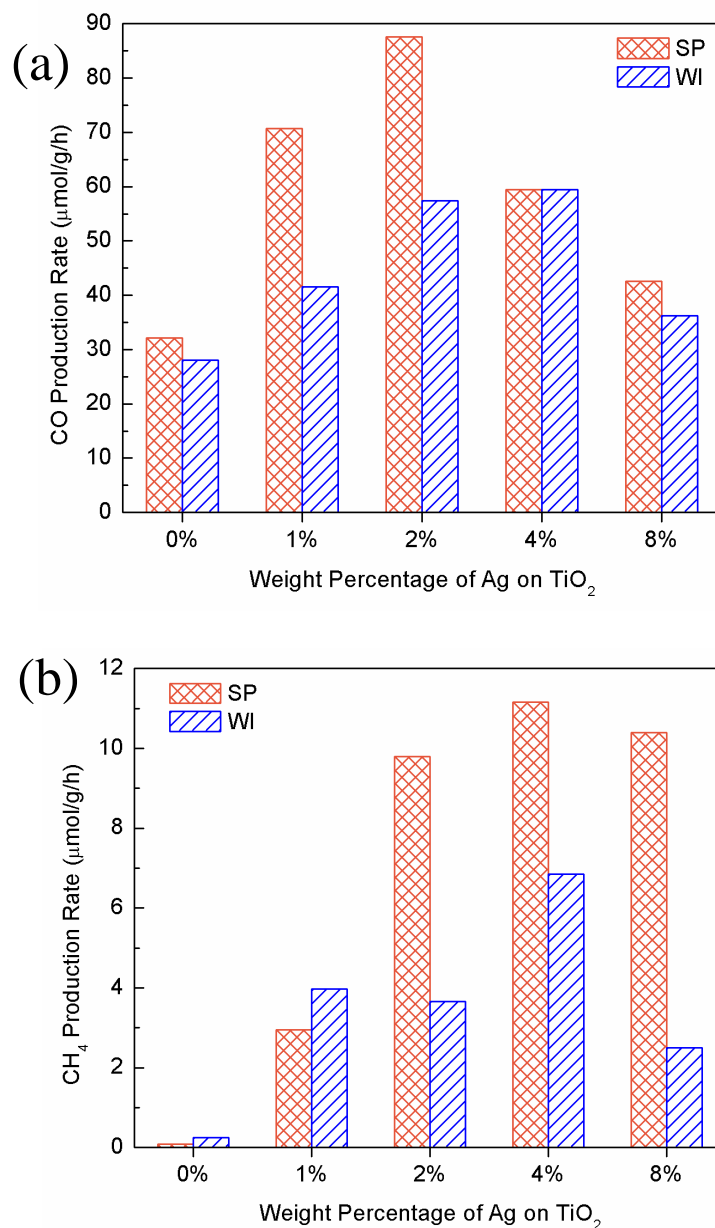
Figure 4.8 Rates of photocatalytic CO_2 reduction to CO (a) and CH_4 (b) for Ag/TiO_2-SP and Ag/TiO_2-WI samples at different Ag concentration (the reaction gas was a mixture of 97.2% CO_2, 2.2% H_2O and 0.6% CH_3OH).

The CO_2 reduction results again confirm that SP samples are advantageous over WI samples and 2% Ag/TiO_2-SP seems to have the highest overall activity in terms of both H_2 production and CO_2 reduction. By correlating to the material property data, the higher activities of SP samples compared with WI samples are mainly ascribed to the larger

specific surface area (**Table 4.1**) and better dispersion of the Ag nanoparticles (**Fig. 4.5**). It is well known that the Schottky barrier at the metal-semiconductor (Ag-TiO$_2$) interface facilitates electron transfer from the semiconductor to the metal, and consequently enhancing electron-hole separation and improving photocatalytic activity. It should be noted that the actual among of Ag on SP samples was only approximately half of that on WI samples (**Table 4.1**). Hence, it is reasonable to also compare the activity of 2% Ag/TiO$_2$-SP with 1% Ag/TiO$_2$-WI where the two samples have similar actual Ag concentration (~1%). Again, the 2% Ag/TiO$_2$-SP sample is much more active than 1% Ag/TiO$_2$-WI with regard to both H$_2$ production and CO$_2$ reduction.

Table 4.2 Production rates and product selectivity of the 2% Ag/TiO$_2$-SP sample under simulated solar illumination.

Reactant gas components and their volume fractions in percentage	Production Rate (μmol/h/g)				Selectivity (%)			H$_2$/CO ratio
	H$_2$	CO	CH$_4$	Total	H$_2$	CO	CH$_4$	
Case1: H$_2$O/CH$_3$OH=2.2/0.6 [a]	1130	18	0.8	1149	98.3	1.6	0.1	63
Case2: CO$_2$/H$_2$O/CH$_3$OH=10/2.2/0.6 [a]	439	43	0.3	482	91.0	8.9	0.1	10.2
Case3: CO$_2$/H$_2$O/CH$_3$OH=50/2.2/0.6 [a]	321	78	0.7	400	80.3	19.5	0.2	4.1
Case4: CO$_2$/H$_2$O/CH$_3$OH=97.2/2.2/0.6 [a]	220	103	12	335	65.7	30.7	3.6	2.1
Case5: CO$_2$/H$_2$O/CH$_3$OH=96.6/2.2/1.2 [a]	429	100	2	531	80.8	18.8	0.4	4.3

a The reactant was balanced with N$_2$.

As described in the Experimental Section that it is not accurate to measure both H$_2$ and CO in a single photo-activity experiment because of the very low sensitivity of H$_2$ measurement when He was used as the GC carrier gas to measure CO. Hence, separate experiments were conducted (by using N$_2$ as the GC carrier gas) to measure the potential H$_2$ production by the same catalyst 2% Ag/TiO$_2$-SP using a reaction gas mixture of CO$_2$/H$_2$O/CH$_3$OH. By combining the two sets of experiments of H$_2$ and CO measurements,

the feasibility of syngas (H_2 + CO) production can be evaluated. The CO_2 partial pressure in the reaction gas was varied from 0% to nearly 100% to examine the potential influence on H_2/CO ratio in the products. The experimental results are summarized in **Table 4.2**, and related chemical reactions involved in the photocatalytic syngas production are listed in Reactions (1)-(6).

$$TiO_2 \xrightarrow{hv} e_{cb}^- + h_{vb}^+ \tag{1}$$

$$2H_2O + 4h^+ \longrightarrow 4H^+ + O_2 \tag{2}$$

$$CH_3OH + h^+ \longrightarrow CH_3O \bullet + H^+ \xrightarrow{multi-stepdecomp.} CO + nH^+ \tag{3}$$

$$2H^+ + 2e^- \longrightarrow H_2 \tag{4}$$

$$CO_2 + 2H^+ + 2e^- \longrightarrow CO + H_2O \tag{5}$$

$$CO_2 + 8H^+ + 8e^- \longrightarrow CH_4 + 2H_2O \tag{6}$$
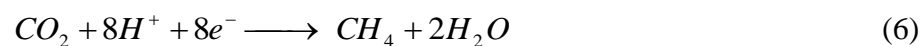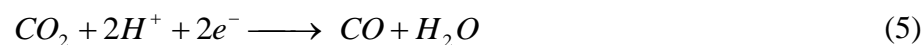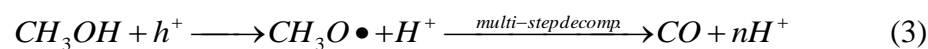
As shown in **Table 4.2**, for Case 1 when H_2O + CH_3OH was the reactant gas in the absence of CO_2, the majority of final products is H_2 (rate = 1130 mmol/h/g; selectivity = 98.3%), with minor CO (rate = 18 mmol/h/g; selectivity = 1.6%) and negligible CH_4. The result indicates that direct decomposition of CH_3OH to H_2 and CO is not likely because the CO selectivity was far less than the stoichiometry where CO/H_2 should be 1:2 for complete decomposition. The minor CO produced may be from multi-step decomposition process where protons are released in each step while photo-induced holes are scavenged (Reaction (3)). In Cases 2 to 4, CO_2 + H_2O+ CH_3OH mixture were used as the reactant gas where the CO_2 partial pressure varied at three levels (10%, 50% and 97.2%), while the H_2O and CH_3OH partial pressure maintained constant at 2.2% and 0.6%, respectively. Compared to Case 1, the production rate of H_2 in the presence of CO_2 (Cases 2-4) decreased while that

of CO significantly increased and that of CH_4 remained negligible. The result clearly indicates that H_2 production (Reaction (4)) and CO_2 reduction (Reactions (5 and 6)) are competing with each other for consumption of electrons and protons, in agreement with the scheme plotted in **Fig. 1.5**. This competition mechanism is also supported by the result that a higher CO_2 partial pressure resulted in a higher CO production rate but a lower H_2 production rate (Cases 2-4). Accordingly, the H_2/CO ratio in the products varied from about 10 to 2, indicating that the ratio is controllable by varying the CO_2 partial pressure or the CO_2/H_2O ratio in the reactants. Another way to control the H_2/CO ratio is to vary the concentration of hole scavenger, CH_3OH, in the reaction gas. By doubling the CH_3OH volume fraction from 0.6% to 1.2% while maintaining the same volume fractions of CO_2 and H_2O (comparing Cases 4 and 5), the H_2/CO ratio also doubled from 2.1 to 4.3, due to the reason that more protons are made available by CH_3OH to favor H_2 production.

It should be noted that the produced CO was mainly derived from CO_2 (Reaction (5)) and not from CH_3OH (Reaction (3)), which is supported by the following evidences. First, in the absence of CO_2, the selectivity of CO production is only 1.6% (Case 1), indicating that generation of CO from direct decomposition of CH_3OH is insignificant. Second, in the presence of CO_2, the selectivity of CO production proportionally increased with the CO_2 concentration in the reaction gas (Cases 2-4), indicating that CO production is directly correlated with CO_2. Third, at the same CO_2 concentration, increasing the CH_3OH concentration enhanced H_2 production rate but the CO production rate remained at the same level (Cases 4 and 5). This suggests that CO production rate is limited by CO_2 and not by CH_3OH. If CO were derived from CH_3OH, an increased CH_3OH concentration could have led to a higher CO production rate. All the above experimental evidences

strongly indicate that CO is indeed a product from CO_2 and not from the hole scavenger, CH_3OH. The production of H_2, however, could come from both H_2O and CH_3OH.

4.4 Conclusion

This work has demonstrated the feasibility of syngas (H_2 and CO) production from a gas mixture of CO_2, H_2O and CH_3OH through a photocatalytic reduction process on Ag/TiO_2 nanocomposite catalysts under solar irradiation. Although the H_2 production and CO_2 reduction processes compete for electrons and protons in the photocatalytic process, the final product selectivity (H_2/CO ratio as low as 2, with negligible CH_4) is in the appropriate range for subsequent Fischer-Tropsch process for liquid hydrocarbon fuel production. The selectivity is tunable by varying the reaction gas composition and the H_2/CO ratio in the range from 2 to 10 has been achieved. In addition, the material property analysis and photocatalytic activity results showed that the ultrasonic spray pyrolysis method is much superior to conventional wet impregnation process with the advantages of smaller Ag nanoparticles, a better Ag dispersion on TiO_2, and a higher fraction of metallic Ag species, which facilitate charge transfer and improve photocatalytic activity. The rates of photocatalytic conversion in this work were among the highest ones reported in the literature.

CHAPTER 5   SYNTHESIS OF NOVEL MGAL LAYERED DOUBLE OXIDES GRAFTED TIO₂ CUBOIDS AND THEIR PHOTOCATALYTIC ACTIVITY ON CO₂ REDUCTION WITH WATER VAPOR

5.1 Introduction

As mentioned in Chapter 1, photocatalytic CO_2 reduction with water using TiO_2 as the photocatalyst typically has low energy conversion efficiency.[109-112] This is because of the major obstacles including the fast recombination rate of photo-generated electron-hole (e-h) pairs, the wide band gap of TiO_2 (3.2 eV for anatase), and the fast backward reactions.[11-12] Approaches such as loading noble metal or metal oxides and doping with non-metal elements have been applied to improve the CO_2 photoreduction activity of TiO_2.[113-115] In addition to these well-known challenges, there are other factors that hinder the photocatalytic activity but are rarely studied in the literature, such as the weakened CO_2 adsorption on TiO_2 at the solid-gas interface in the presence of water vapor and limited desorption of reaction products or intermediates from the catalyst surface.[116-117] As a result, to enhance the CO_2 adsorption on the photocatalyst, a prior step to photoreduction, is important to improve the CO_2 photoreduction efficiency to hydrocarbon fuels.

Our previous studies have report MgO-TiO_2 composites as hybrid adsorbent/photocatalyst materials for enhanced CO_2 photoreduction.[116-117] MgO was chosen as the CO_2 adsorbent because of its good CO_2 adsorption capability that is boosted in the presence of H_2O vapor.[118-120] We found that MgO-TiO_2 possessed much higher activity and more stable performance than pristine TiO_2, particularly at a medium

temperature range (around 150 ℃), which may be due to the easier desorption of reaction intermediates and the enhanced CO_2 adsorption by MgO at a higher temperature. We also reported that the concentration and dispersion of MgO on the MgO/TiO_2 composite strongly influenced the CO_2 photoreduction activity and 5% MgO was the optimum loading on TiO_2 surface. However, since both MgO and TiO_2 were in the form of nanoparticles in the MgO/TiO_2 composites, it was difficult to distinguish the two components by microscopic analysis and to correlate the catalytic activity with materials morphology or structure. In addition, MgO has been reported to have a relatively low kinetics in CO_2 adsorption.[121-122] Hence, other medium temperature CO_2 sorbents with different morphologies and faster adsorption kinetics may be of greater interest to serve as the adsorbent component of the hybrid material for enhanced CO_2 photoreduction.

Layered double hydroxides (LDHs), also known as hydrotalcite-like compounds, and their post-calcination product, layered double oxides (LDOs) have been investigated as CO_2 sorbent.[123-125] LDHs can be chemically expressed by a general formula $M_{1-x}^{2+}M_x^{3+}(OH)_2A_x \cdot nH_2O$, where M^{2+} and M^{3+} present metal ions and A stands for exchangeable anions (Cl⁻, NO$_3$⁻, CO$_3$²⁻, SO$_4$²⁻).[126-129] The characteristics of LDHs provide the LDOs properties with a large number of Brønsted basic sites, and thus LDOs is considered as a promising candidate for CO_2 adsorption,[130] and activated MgAl-LDOs are found to have a high sorption capacity for CO_2.[123, 125, 131] It is reported that MgAl-LDOs can capture much more CO_2 than MgO at the medium temperature range 150-450 ℃.[132-133] Hence, MgAl-LDOs could be a good candidate in replacement of MgO to combine with TiO_2 photocatalyst to improve CO_2 photoreduction operated at a medium temperature (~150 ℃).

The objective of this work is to design a novel hybrid adsorbent/photocatalyst material by grafting MgAl-LDOs (as the CO_2 adsorbent component) onto the surface of micrometer size TiO_2 cuboids (as the photocatalyst component) and to investigate the catalytic activity of CO_2 photoreduction in correlation with the materials properties. To obtain such a hybrid material structure, it is desirable to have micrometer size TiO_2 for MgAl-LDOs to be grafted on because MgAl-LDOs are reported to be micrometer or sub-micrometer size platelets. The platelet-shape MgAl-LDOs can be distinct from the micrometer-size TiO_2 cuboids, and thus, the morphology and concentration of the two components can be easily manipulated.

5.2 Materials and Methods

The micron size TiO_2 were prepared via a hydrothermal method that has been described in the literature. Typically, 1.0 g TiO_2 (Aeroxide P90) was dispersed in 60 ml 10 M NaOH aqueous solution with 1:1 H_2O/ethanol volume ratio. The solution was kept stirring for 30 min and then transferred to a Teflon-lined autoclave. The TiO_2 sample obtained after 16 h hydrothermal at 180 ˚C was washed with 0.1 M HCl aqueous solution until pH equal to 3-4 and then washed with deionized (DI) water until pH 7.   MgAl-LDH grafted TiO_2 cuboids were prepared by a coprecipitation method. The as-prepared TiO_2 was re-dispersed in 30 ml 3.0 M urea solution to form solution A. $Mg(NO_3)_2 \bullet 6H_2O$ and $Al(NO_3)_3 \bullet 9H_2O$ were dissolved in 30 ml DI water with $[Mg^{2+}]+[Al^{3+}]$=0.15 M, n(Mg)/n(Al)=2:1 to obtain solution B. Solution B was dropwise added into solution A under stirring. The mixture was transferred to a round bottom flask in an oil bath. The flask was equipped with a water condenser with cooling water. The temperature for the mixture was set to be ~95 ˚C and was kept under continuous magnetic stirring for 12 hours. The

obtained precipitate was washed with DI water until pH 7 and vacuum dried at 80 ºC overnight to form MgAl-LDH grafted TiO_2. Finally, the powder was calcined at 400 ˚C for 3 hours to form MgAl-LDO grafted TiO_2. To find the optimum MgAl-LDO concentration in the composites to obtain the best photocatalytic CO_2 reduction activity, the samples with different mass ratio of MgAl-LDO to TiO_2 were prepared. The samples were denoted as x% MgAl-LDO/TiO_2, in which x represents the nominal weight percentage of MgAl-LDO in the sample. To obtain pristine TiO_2 cuboids as a control, the MgAl-LDO/TiO_2 sample was washed with 60 ˚C 1 M HCl aqueous solution to remove the MgAl-LDO component.

The crystal structures of the MgAl-LDO/TiO_2 samples were identified by X-ray diffraction (XRD, Scintag XDS 2000) using Cu Kα irradiation at 45 kV, and a diffracted beam monochromator at 40 mA. The optical properties were examined by UV-vis diffuse reflectance spectroscopy using a UV-vis spectrometer (Ocean Optics) with $BaSO_4$ as the background. Scanning electron microscopy (SEM) (Hitachi S4800) was used to investigate the catalyst morphology. The dispersion of elements (Mg, Al, Ti, O) on MgAl-LDO/TiO_2 was analyzed by X-ray elemental mapping. Samples (15 mg) were examined under an air flow rate of 100 ml/min at a scan rate of 10 ˚C min^{-1} between room temperature and 600 ˚C.

The photocatalytic reduction of CO_2 with H_2O vapor was conducted using a home-made quartz tube photoreactor operating in a continuous flow mode, as shown in **Fig. 5.1**. For each test, 100 mg catalyst was used and evenly dispersed onto a rectangular glass-fiber filter that was placed alongside the wall of the quartz tube and facing the UV light illumination. Cylinder gas CO_2 (99.999%, Praxair) continuously passed through a DI water bubbler to bring a gas mixture of CO_2 + H_2O (with 2.3 vol.% H_2O) into the photoreactor.

A high gas flow rate was used initially to purge out air inside the reactor and then the flow rate was lowered and maintained at 2.0 ml min^{-1} during photoreaction. A home-made 100 W UV lamp was used as the UV light source, and the light intensity is about 10 mW cm^{-2} in the UV range ($\lambda < 390$ nm). To reach and maintain a reaction temperature at 150 ˚C, the optimum temperature found in our previous work for MgO–TiO$_2$ catalysts, a 250 W infrared lamp was used to heat up the photoreactor and the temperature can be adjusted by varying the distance between the IR lamp and the reactor. The gaseous products in the reactor effluent were continuously analyzed with a 15 min interval using a gas chromatograph (GC, Agilent 7890A) equipped with an automated gas valve and a thermal conductivity detector (TCD) and flame ionization detector (FID).
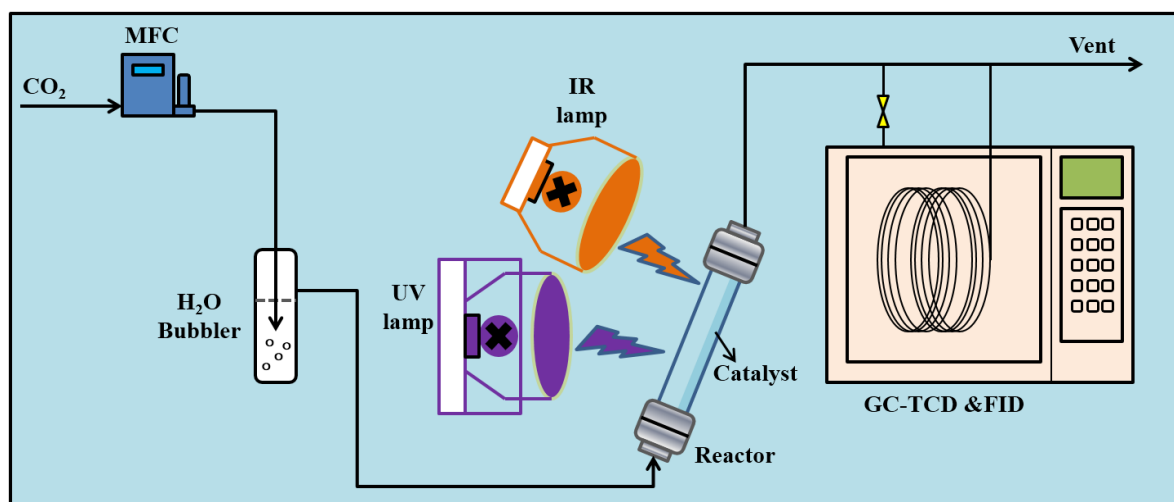
Figure 5.1 Experimental setup for photocatalytic CO$_2$ reduction with water vapor

5.3 Results and Discussions

The crystal structures of TiO$_2$ cuboids, MgAl-LDH, MgAl-LDOs, MgAl-LDH/TiO$_2$ and MgAl-LDO/TiO$_2$ composites were all characterized by XRD. **Fig. 5.2** shows the XRD patterns for uncalcined MgAl-LDH and 10% MgAl-LDH/TiO$_2$ samples.

The diffraction peaks in both patterns were indexed to MgAl-LDH[123, 127, 134] and weaker peaks were found for the MgAl-LDH/TiO$_2$ sample. No TiO$_2$ characteristic peaks were observed on the XRD patterns indicating that TiO$_2$ crystal phase was not formed before calcination. **Fig. 5.3** shows the XRD patterns of the samples after calcination, i.e., TiO$_2$ cuboids, MgAl-LDOs, and MgAl-LDO/TiO$_2$ composites. For TiO$_2$ cuboids, all the diffraction peaks were attributed to the anatase phase (JCPDS No. 21-1272).[110, 112, 135] For the MgAl-LDOs sample, all the diffraction peaks were indexed to MgO.[12, 19, 32] For MgAl-LDO/TiO$_2$ samples, as the MgAl-LDO concentration increases from 8 to 12 wt% (or TiO$_2$ concentration decreases from 53 to 34 wt%), both TiO$_2$ anatase diffraction peaks and MgO diffraction peaks can be observed while MgO peaks intensity increases. The Scherrer equation was applied to calculate the crystal size of TiO$_2$. The diffraction peaks of TiO$_2$ anatase in MgAl-LDO/TiO$_2$ composites are narrowed compared with TiO$_2$ cuboids, suggesting bigger crystal size of TiO$_2$ due to MgAl-LDH addition. The average crystal size of TiO$_2$ anatase in TiO$_2$ cuboids was 15 nm. By comparison, the average crystal sizes of TiO$_2$ anatase in MgAl-LDO/TiO$_2$ composites were 26 nm, 32 nm and 40 nm for 8% MgAl-LDO/TiO$_2$, 10% MgAl-LDO/TiO$_2$ and 12% MgAl-LDO/TiO$_2$, respectively. Obviously, the crystal size of TiO$_2$ anatase in the MgAl-LDO/TiO$_2$ composites increases as the MgAl-LDO content increases or TiO$_2$ content decreases. The possible reason is highly crystalline LDH phase was formed as MgAl concentration increased that inhibits TiO$_2$ crystalline growth. This result was similar with MgAl-LDO/CeO$_2$ result reported by Valente et.al.[136] that CeO$_2$ crystal size decreased as MgAl-LDO increased.
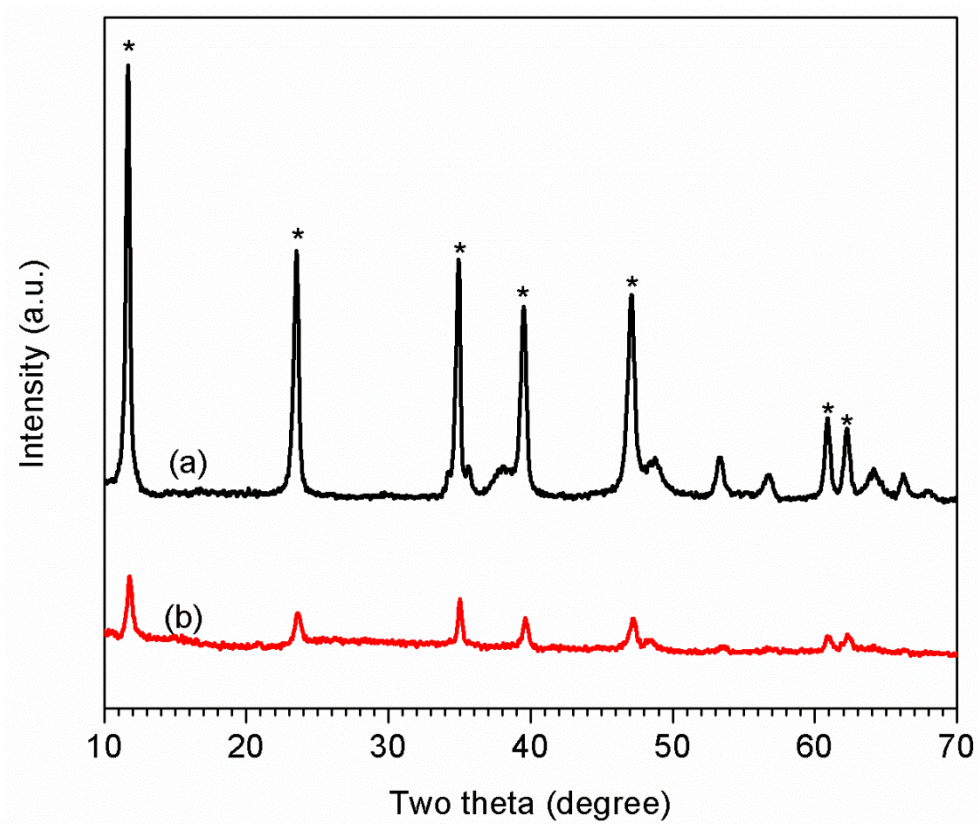
Figure 5.2 XRD patterns of the uncalcined samples: (a) MgAl-LDH and (b) 10% MgAl-LDH/TiO$_2$ (uncalcined samples; * represents MgAl-LDH characteristic peaks)
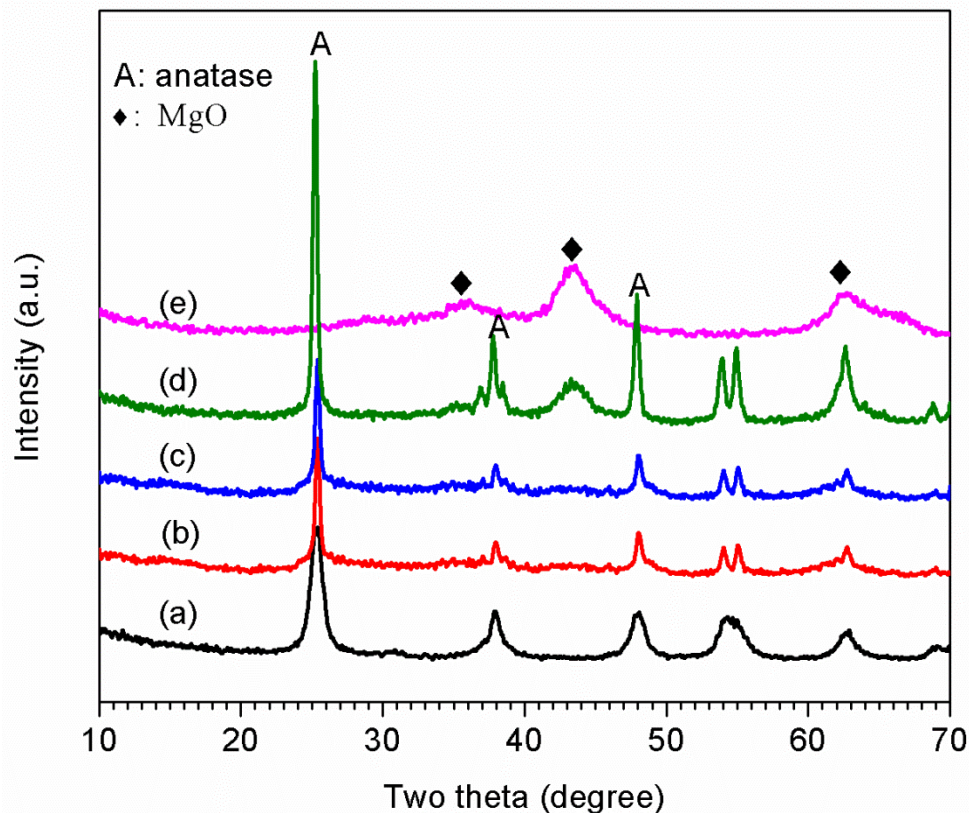
Figure 5.3 XRD patterns of the calcined TiO_2, MgAl-LDO, and MgAl-LDO/TiO_2 with different TiO_2 concentrations: (a) TiO_2 cuboids; (b) 8% MgAl-LDO/TiO_2; (c) 10% MgAl-LDO/TiO_2; (d) 12% MgAl-LDO/TiO_2; and (e) MgAl-LDO.

Fig. 5.4 shows the SEM images of MgAl-LDOs and TiO_2 cuboids. MgAl-LDOs consists of platelets around 2 μm in size. The length of the TiO_2 cuboids is in micrometer size range with a high aspect ratio. **Fig. 5.5** shows the SEM images of MgAl-LDO/TiO_2 samples with different compositions. The low magnification SEM images in **Fig. 5.5 a-c** show that the three samples were composed of MgAl-LDOs grafted on micrometer size TiO_2 cuboids. The platelet shape of MgAl-LDOs on the composites after calcination was almost the same as the as-prepared uncalcined composites MgAl-LDHs. In most of literature reported, MgAl-LDHs platelets morphology cannot be maintained after calcination.[129, 137] MgAl-LDOs platelets with a highly ordered layered array are proved

beneficial for the application as adsorbent and catalyst.[138-139]   The high magnification SEM images in **Fig. 5.5 d-f** show both the size and the coverage of MgAl-LDOs grafted on TiO_2 cuboids increased as the MgAl-LDO ratio increased. The distributions of Mg, Al, Ti and O elements in the MgAl-LDO/TiO_2 composites were analyzed by X-ray elemental mapping, and the results are shown in **Fig. 5.6**. The elemental mapping images demonstrated that the cuboids skeleton were mainly composed of Ti element and the grafted platelets were composed of Mg and Al elements that were evenly distributed on the cuboids surface.
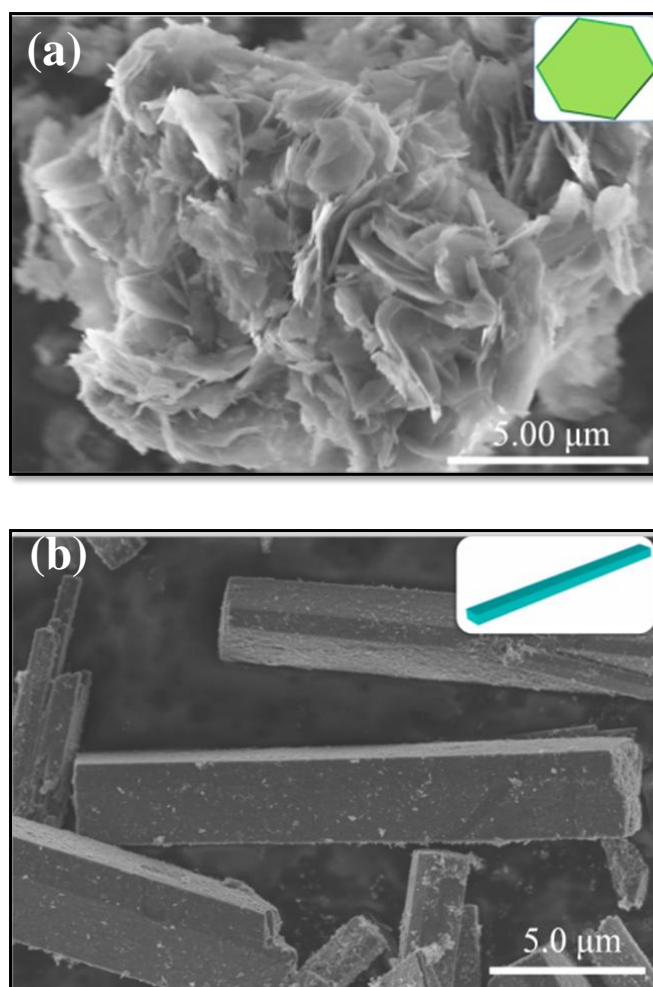
Figure 5.4 SEM images of (a) MgAl-LDOs and (b) TiO_2 cuboids
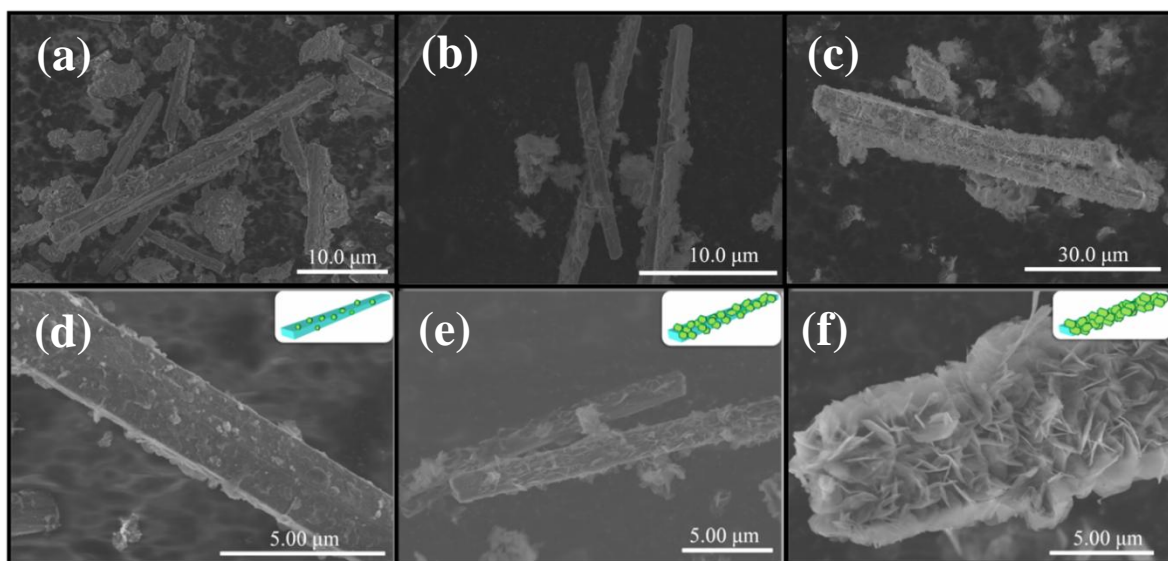
Figure 5.5 SEM images of the calcined MgAl-LDO/TiO$_2$ composites: (a,d) 8% MgAl-LDO/TiO$_2$, (b,e) 10% MgAl-LDO/TiO$_2$, and (c,f) 12% MgAl-LDO/TiO$_2$.
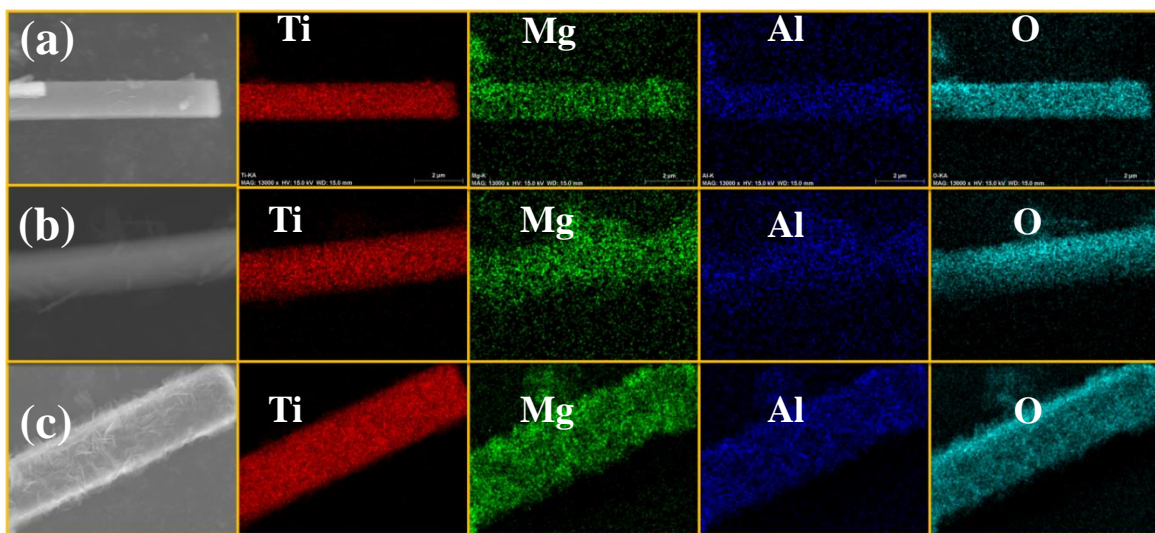
Figure 5.6 X-ray elemental mapping images of the MgAl-LDO/TiO$_2$ composites: (a) 8% MgAl-LDO/TiO$_2$, (b) 10% MgAl-LDO/TiO$_2$, and (c) 12% MgAl-LDO/TiO$_2$.

Diffuse reflectance UV-vis spectra were recorded to explore the influence of MgAl-LDOs addition on the optical property of TiO$_2$. As shown in **Fig. 5.7**, TiO$_2$ cuboids absorbs light at wavelength shorter than 400 nm, corresponding to a band gap of about 3.0 eV. MgAl-LDOs show no adsorption ability of light at the wavelength range between 300-600 nm. Incorporation of MgAl-LDOs in TiO$_2$ cuboids leads to a blue-shift in the adsorption

edge.
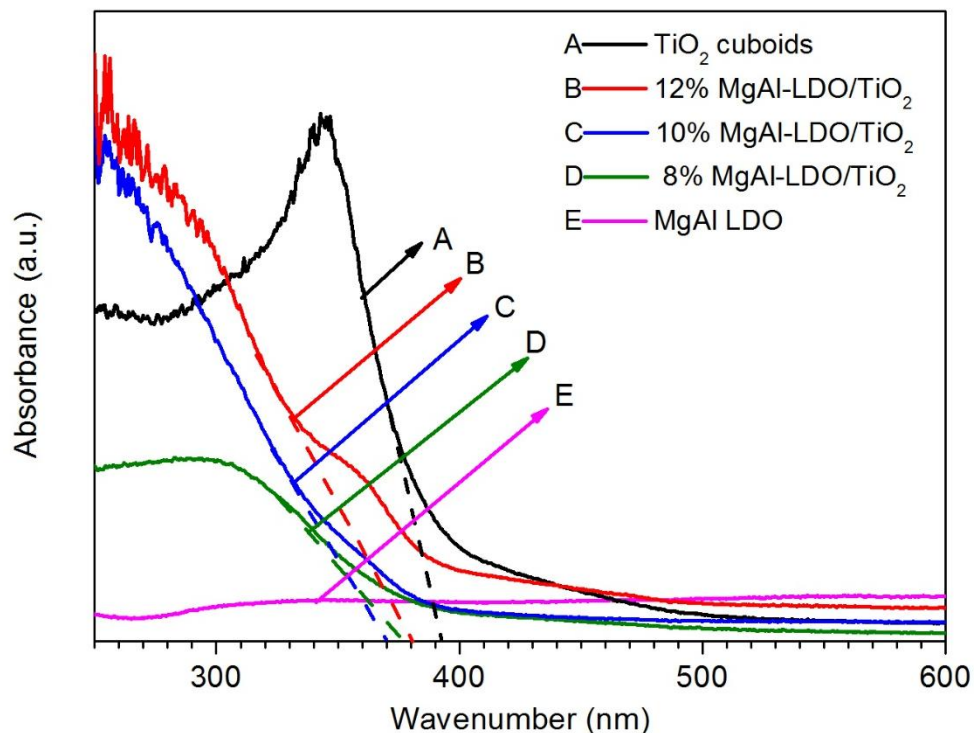
Figure 5.7 UV-vis diffuse reflectance spectra of TiO_2 cuboids, MgAl-LDO, and MgAl-LDO/TiO_2 composites with different MgAl-LDO concentrations.

Photocatalytic activity tests were carried out under UV light irradiation at 50 °C for 4 h and subsequently at 150 °C for another 8 h, and the results are shown in **Fig. 5.8**. CO was found to be the major product with a minor CH_4 concentration that was one or two orders of magnitude lower than CO. Thus, only CO production results were shown in **Fig. 5.8** to compare the activities of the different catalysts. **Fig. 5.8a** shows bare TiO_2 cuboids had a CO production rate around 1.0 μmol g^{-1} h^{-1} at 50 °C while pure MgAl-LDO had no activity for CO production. MgAl-LDOs addition on TiO_2 cuboids had no significant improvement for CO production rate. The possible reason is MgAl platelets partially or fully covered TiO_2 cuboids which blocks CO_2 contact with TiO_2. Moreover, MgAl-LDOs has weak adsorption ability of CO_2 at mild room temperature that also leads to poor CO_2 contacting with TiO_2.[130]

For the proceeding 8 hours test under UV light at 150 ˚C, CO production rate for TiO$_2$ cuboids was almost the same as the first 4 hours at 50 ˚C. Pure MgAl-LDOs still showed no activity of CO$_2$ reduction. Interestingly, 10% MgAl-LDO/TiO$_2$ exhibited an obvious enhancement of CO production rate with a maximum 4.8 μmol g^{-1} h^{-1}, 2.5 times higher than that under 50 ˚C. For MgAl-LDO/TiO$_2$ samples, the activity of CO$_2$ photoreduction was in the order of 10% MgAl-LDO/TiO$_2$ > 8% MgAl-LDO/TiO$_2$ > 12% MgAl-LDO/TiO$_2$. The optimum concentration of MgAl-LDOs on the MgAl-LDO/TiO$_2$ was 10%. 12% MgAl-LDO/TiO$_2$ performed the lowest CO production rate amongst the MgAl-LDO/TiO$_2$ composites. Even though, it showed a similar CO production rate as TiO$_2$ cuboids under 150 ˚C. This indicates that MgAl-LDOs grafting on TiO$_2$ helps improve the photoactivity of CO$_2$ reduction. It is possibly because MgAl-LDOs absorbs more CO$_2$ at higher temperature (150 ˚C) onto the composites which creates more opportunity for CO$_2$ to be photoreduced to CO. On the other hand, as MgAl-LDOs concentration decreased to 8%, CO production rate is between that of 12% TiO$_2$-MgAl-LDOs and 10% TiO$_2$-MgAl-LDOs but still much lower than that of 10% TiO$_2$-MgAl-LDOs. This may be explained in terms of increased crystal size of the anatase TiO$_2$ nanoparticles.[140] Another reason could possibly be that MgAl-LDOs platelets covered the majority parts of TiO$_2$ cuboids surface either blocked the CO$_2$ and H$_2$O vapor contacting with TiO$_2$ or electrons transferring from TiO$_2$ to CO$_2$ and H$_2$O molecules.

To better understand the carbon source of CO, further photocatalytic activity tests were carried out by changing the CO$_2$+H$_2$O vapor atmosphere to Helium (He) + H$_2$O vapor atmosphere. As shown in **Fig. 5.8b**, the CO production rate were compared on 10% MgAl-LDO/TiO$_2$ under both conditions. Under UV irradiation, there was no CO production in

He atmosphere, indicating CO_3^{2-} in MgAl LDOs structure was stable under mild room temperature. Compared with CO_2 atmosphere, CO was produced on 10% MgAl-LDO/TiO$_2$ in the CO_2 under UV irradiation, which came from CO_2 photoreduction on this composite. After introducing IR irradiation (150 ˚C), CO production was shown in He atmosphere with a maximum rate of 1.3 μmol g^{-1} h^{-1}. The experiments was carried out several times to rule out other impurities that might produce CO. The results indicated that most of CO was attributed to CO_2 photoreduction and a small portion of CO was from CO_3^{2-} in MgAl LDOs.
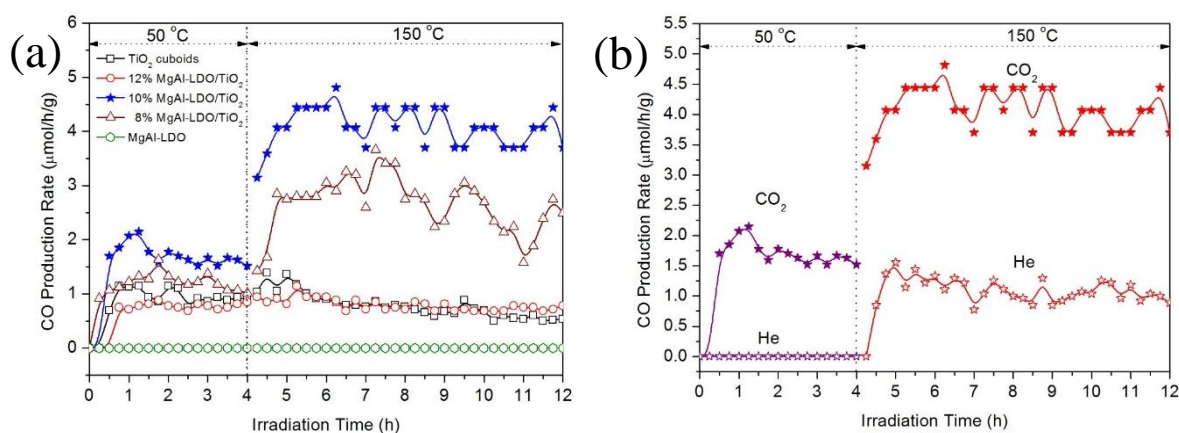
Figure 5.8 The rate of CO production from CO_2 photoreduction under UV light irradiation at 50 ˚C for 4 h and subsequently at 150 ˚C for 8 h using (a) TiO$_2$ cuboids, MgAl-LDO and three MgAl-LDO/TiO$_2$ composites in CO_2 + H_2O vapor atmosphere, and (b) 10% MgAl-LDO/TiO$_2$

5.4 Conclusion

This work has demonstrated that the successful synthesis for novel hybrid structure of MgAl-LDOs platelets grafted on TiO$_2$ cuboids with high length to width ratio. MgAl-LDOs addition has no impact on the optical propertied of TiO$_2$. The morphology of TiO$_2$-MgAl-LDOs showed that the surface coverage on TiO$_2$ on MgAl-LDOs platelets could be controlled by tuning the MgAl-LDOs to TiO$_2$ ratio. As the MgAl-LDOs concentration increases, TiO$_2$ crystal size was increased. MgAl-LDOs grafting on TiO$_2$ cuboids may help

improve the adsorption ability of CO_2 onto TiO_2 which improves the photocatalytic activity of CO_2 reduction. The optimum MgAl-LDOs concentration was found to be 10% which performed the highest CO production rate. The proposed reason for this is: at higher MgAl-LDOs concentration, MgAl-LDOs platelets covered the majority parts of TiO_2 cuboids surface either blocked the CO_2 and H_2O vapor contacting with TiO_2 or electrons transferring from TiO_2 to CO_2 and H_2O molecules; Moreover, the crystal size increase of TiO2 anatase may also lead to a poor CO2 photoreduction activity. At lower MgAl-LDOs concentration, less CO_2 and H_2O amount may be adsorbed onto the composites which also leads to lower CO production rate.

CHAPTER 6 FACILE SYNTHESIS OF CARBON-TIO₂ NANOCOMPOSITES WITH ENHANCED REVERSIBLE CAPACITY AND CYCLIC PERFORMANCE AS ANODES FOR LITHIUM-ION BATTERIES

6.1 Introduction

As mentioned in Chapter 1, Graphitic carbons are most commonly used as conventional commercial anode materials owing to its low cost, relatively high energy density and very low flat working potential. However, graphitic carbon anode materials suffer the disadvantages of severe safety issues because of its low operating voltage (~0.1 V vs Li/Li$^+$), poor life cycle performance due to solid-electrolyte interface (SEI) film and the formation of dendritic lithium on the surface of graphitic carbons anode.[141-144]

Thus, it is essential to make improvements such as safety, cost, high efficiency and long cycle life of the anode materials for LIBs. Researchers in the scientific and industrial communities have investigated different materials such as silicon, tin (II) based oxide[145-146] and TiO$_2$ as LIBs anode to replace graphite materials in order to eliminate the safety issue and meanwhile improve LIBs performance. Different from tin (II) based oxides and silicon, TiO$_2$ material is structural stable during lithium insertion and extraction which means a very low volume change (<4% for Li$_x$TiO$_2$, 0≤x≤1) for electrode.[147-148] This advantage guarantees its good stability during charge/discharge process at high current density rate. Moreover, its high working voltage (> 1.5 V vs Li/Li$^+$) avoids reactions with organic electrolyte and short circuit caused by electrode expansion during cycling that

make it safer than graphite anode material.[149-153] TiO_2 offers a theoretical capacity of 335 mAh g^{-1} based on the complete reduction of Ti^{4+} to Ti^{3+}, which is comparable to that of conventional graphite anode materials.[154-156] Being abundant, low cost and environmentally benign,[109, 111, 143, 156] TiO_2 has been considered as a promising candidate as LIBs anode material.

It is well known that TiO_2 exists in three different polymorphs in nature: anatase, brookite and rutile, among which, it was reported that brookite and rutile phase TiO_2 can only accommodate limited small amount of Li^+ ions, while anatase phase has superior accommodation capacity of lithium insertion.[157-158] However, TiO_2 anodes practical capacity is only 168 mAh g^{-1} because of the poor electronic and ionic conductivity in its bulk form, limiting TiO_2 anode practical applications.[143-144, 151, 154, 156] Two general approaches are widely used to improve the electronic and ionic conductivity associated with Li^+ ions in the active materials of the anode. One approach is tailoring the bulk state TiO_2 to nanoscale dimensions to reduce Li^+ ions diffusion length and increase the energy storage capacity.[143, 159] The other approach is blending TiO_2 with conductive material such as conductive carbon to improve its electronic conductivity.[144, 160] Various materials based on the above two aspects consideration have been investigated and exhibited relatively superior performance as anode for LIBs, including 3D TiO_2-mesoporous carbon nanocomposite,[143] TiO_2-C composites nanotubes,[144] ordered mesoporous C-TiO_2,[147] TiO_2@C composites nanofibers,[160] etc. TiO_2 in these composites are commonly synthesized via hydrothermal, template and other post-treatment procedures. Specifically, hydrothermal method usually requires a relatively long reaction time at high temperature and pressure condition. The template method for TiO_2 synthesis takes further steps to

remove the template, which makes the method unfavorable for practical application. Furthermore, none of the electrode materials exhibited capacities higher than 300 mA h g^{-1} between the potentials of 1.0 V to 3.0 V.

Herein, we report carbon decorated TiO_2 nanocomposites (C-TiO_2) synthesized via a facile carbonization process as an excellent candidate for anode materials in LIBs. The fabrication process is the first time reported for carbon decorated directly on commercial TiO_2 materials under relative mild temperature condition, with special focus on the carbon growth control on TiO_2 and application as LIBs anode material. Conductive carbon material directly decorated on TiO_2 particles without any post-treatment processes. In this trial, the objective is to generate a synthesis process for C-TiO_2 used as anode material for LIBs which is cost-effective and easy to be applied in commercial system. The starting materials used for preparation are commercial TiO_2 products (P25 and P90), which are easily available and inexpensive. Sucrose is also used to form the carbon on TiO_2 being carbonized with very little amount of sulfuric acid. The preparation process is quite simple and easy to be scaled up. This nanocomposites structure offers advantages such as: (1) an improved Li^+ ion transport due to the size of the individual TiO_2 anatase nanoparticles, (2) an improvement in the electronic conductivity achieved via amorphous carbon coating. The battery performance results demonstrate that C-TiO_2 nanocomposites exhibit significantly enhanced capacity and rate capability as compared to bare TiO_2 nanoparticles when used as LIBs anode material.

6.2 Experimental Method and Characterization

C-TiO_2 were prepared via three simple steps (**Fig. 6.1**). Firstly, sucrose in sulfuric acid solution was mixed with TiO_2 (Evonik P25 or P90) with a designated C:TiO_2 weight

ratio. After thoroughly mixing, the mixture was transferred to a round-bottom flask and heated up to 90 ˚C in an oil bath under vigorous stirring. The round-bottom flask was equipped with cooling water reflux condenser to condense the vapor and ensure a constant solution amount in the flask. Secondly, the obtained brown color precipitate after 24 hours sucrose dehydration was washed until its pH value to 7. The resultant mixture was dried at 80 ˚C for 12 hours. Finally, the as-dried composite was calcined in N_2 atmosphere at 450 ˚C for 3 hours. For comparison purpose, P25 and P90 were also treated following the same procedure of C-TiO$_2$ synthesis without sucrose and sulfuric acid addition. The corresponding composites were denoted as a%C-P25 and a%C-P90 (a% represents carbon weight percentage).
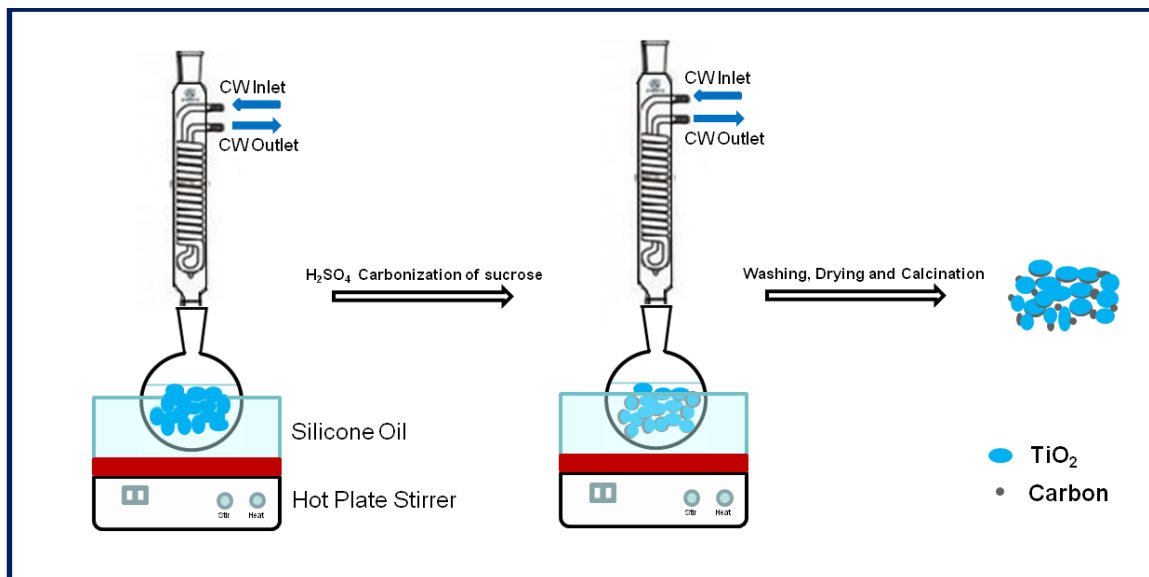
Figure 6.1 Schematic diagram of decorating TiO$_2$ with carbon process in a round bottom flask connected to a cooling water (CW) condenser and formation of C-TiO$_2$ nanocomposites

The crystal structures of the products were identified by X-ray diffraction (XRD) (Scintag XDS 2000) using Cu Kα irradiation at 45 kV and a diffracted beam monochromator operated at 40 mA in the 2θ range from 20˚ to 80˚ at a scan rate of 2˚

/min. Scanning electron microscopy (SEM) equipped with energy-dispersive X-ray (EDX) spectroscopy (Hitachi S4800) was used to analyze the nanocomposites morphology and surface elemental composition. Transmission electron microscopy (TEM, Hitachi H9000NAR) and high-resolution TEM (HRTEM, Hitachi H9000NAR) were used to examine the particle size and dispersion of amorphous carbon on TiO_2 as well as the lattice information. The Brunauer-Emmett-Teller (BET) specific surface area of the composites was measured by nitrogen adsorption at 77 K on a surface area and porosity analyzer (Micrometrics ASAP 2020). Before each adsorption measurement, approximate 0.10 g sample was degassed at 100 °C for 18 hours. The BET surface area was determined by a multipoint BET method using the adsorption data in a relative pressure (P/P_0) range 0.05-0.3. Pore size distribution was determined via Barret-Joyner-Halender (BJH) method using desorption isotherm. The N_2 adsorption volume at the relative pressure of 0.998 was used to determine the total pore volume and average pore size. The thermal stability of electrode materials were carried out on a thermalgravimetric analyzer (TGA-DAT-2960 SDT) at a heating rate of 20 °C min^{-1} from 25 to 1000 °C in air.

80 wt.% active material (C-TiO_2 or TiO_2) powder with 10 wt.% carbon black and 10 wt.% Poly(vinylydene fluoride) (PVDF) binder was homogeneously mixed in N-methyl pyrolidinone (NMP). The slurry was well deposited by doctor blading onto a copper foil, and the as-coated copper foils were dried under vacuum at 100 °C overnight. Each electrode was carefully weighed before use and several electrodes were tested to ensure the reproducibility of the electrochemical behavior.

The working electrodes and Li metal foil counter electrode were assembled into cells by using Celgard 2400 as the separator and 1 M solution of $LiPF_6$ in ethylene

carbonate (EC) and dimethyl carbonate (DMC) (EC: DMC volume ratio 1:1) as the electrolyte. The cells were constructed in an Argon-filled glove box. The charge/discharge curves were measured using a LAND Cell tester (Wuhan, China) at a cutoff voltage of 1.0-3.0 V under current densities of 30, 60, 300 mA g^{-1}. The specific capacity and current density were calculated based on TiO_2 mass only. Cyclic voltammetric curves were recorded in a voltage range of 1.0-3.0 V at a scan rate of 0.2 mV s^{-1}. The electrochemical impedance spectra results were recorded by applying an alternating current of 5 mV in a frequency range from 0.01 Hz to 100 kHz.

6.3 Results and Discussion

Fig. 6.2 shows the XRD patterns of TiO_2 and C-TiO_2 nanocomposites. The phase contents and crystal sizes of anatase and rutile were calculated and summarized in **Table 6.1**. P25 exhibited characteristic peaks for both anatase (JCPDS No. 21-1272) and rutile (JCPDS No. 21-1276) with 85.9% anatase and 14.1% rutile. The phase composition in P25 sample is consistent with the reported literature.[161] The average crystal size for anatase and rutile in P25 is 18.5 and 21.3 nm, respectively, according to the Scherrer equation. In comparison, P90 exhibited prominent characteristic peaks for anatase (92.6%) and very small peaks for rutile (7.4%). The phase composition in P90 also agrees with the results reported.[162-163] The crystal size of anatase and rutile in P90 are 11.7 and 15.9 nm, respectively, smaller than that in P25. There was no significant phase fraction change for P90 after carbon decoration, while its crystal size slightly increased. Similar phenomena were found on P25. The increased crystal size can be explained by the additional calcinations process for the carbon decorated samples.[164] From XRD patterns of C-P90 and C-P25, no peak shift was observed compared with carbon free samples, indicating the

absence of any chemical bonding or reaction between the TiO_2 nanoparticles and carbon.

Furthermore, there are no characteristic peaks of carbon detected indicating the formation

of amorphous carbon.[153]

Table 6.1 Fractional phase content, crystal size and BET specific surface area of P25, P90, C-P90 and C-TiO_2 anatase samples

Samples	Phase content (%)		Crystal size (nm)		S_{BET} (m^2/g)
	A	R	A	R	
P25	85.9	14.1	18.5	21.3	57
P90	92.6	7.4	11.7	15.9	99
1.8% C-P25	87.6	12.4	18.1	24.6	54
1.9% C-P90	95.5	4.5	12.8	32.8	97
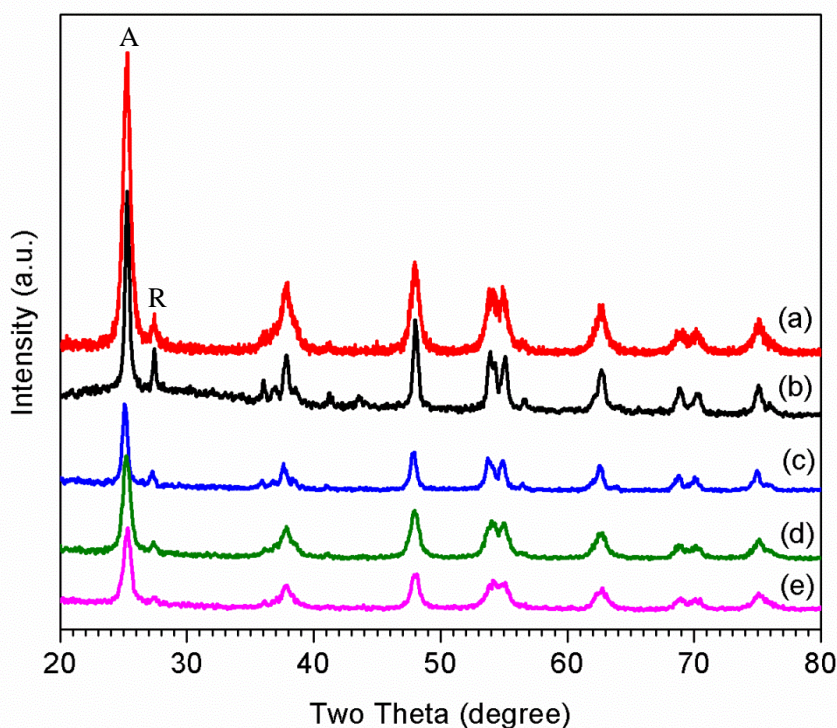
Figure 6.2 XRD pattern of (a) P90 (b) P25 (c) 1.8%C-P25 (d) 1.9%C-P90 and (e) 9.5%C-P90.

The textural properties and morphology of C-TiO$_2$ samples were characterized by BET, SEM, EDX-X-ray elemental mapping and HRTEM. **Fig. 6.3** shows the N$_2$ adsorption-desorption isotherms of TiO$_2$ and C-TiO$_2$ samples. P25, P90, 1.8% C-P25 and 1.9% C-P90 samples exhibited mesoporosity in the form of typical type IV isotherms with a H3 hysteresis loop. According to IUPAC classification, mesoporous materials characterizing with the type H3 loop are commonly observed with aggregates of plate-like particles, leading to the slit-shaped pores.[165] **Table 6.1** compares the BET surface areas for TiO$_2$ (P25, P90) and C-TiO$_2$ samples. Bare TiO$_2$ and 1.8%C-P25 displayed a comparable surface area, probably because a small amount of carbon were deposited on the surface of TiO$_2$. Notably, P90 and 1.9%C-P90 have a larger specific surface area than P25 and 1.8%C-P25, likely due to the smaller particle size of P90 as evidenced by SEM images described later in this paper. The surface area of the sample was slightly decreased for both carbon decorated TiO$_2$, which was reasonable due to the agglomeration during the carbonization and calcination process. It is notable that 1.9% C-P90 still possesses a higher specific surface area (96.8 m^2/g) compared with 1.8% C-P25 (54.2 m^2/g).
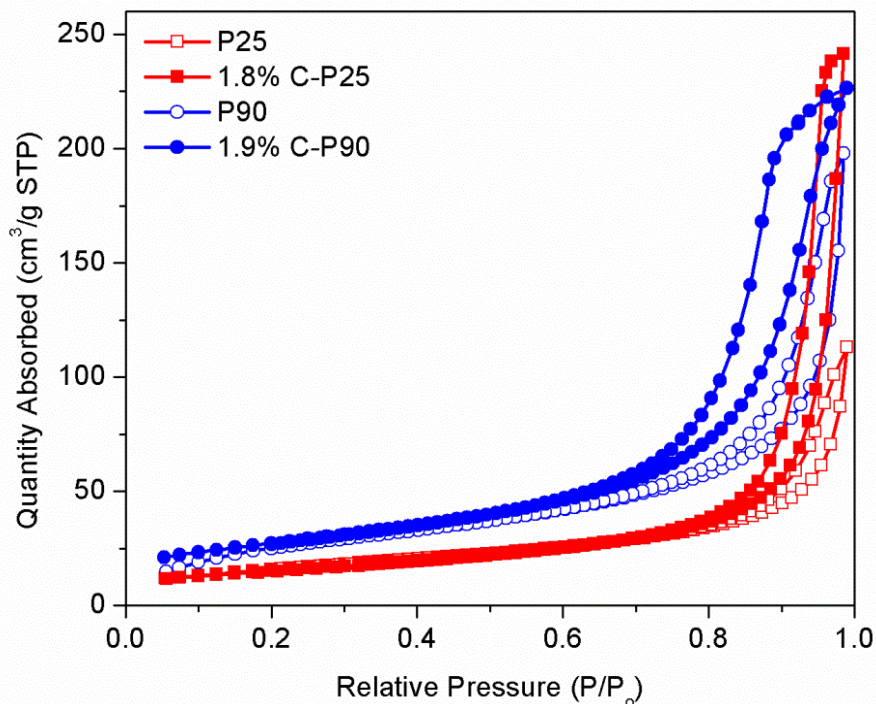
Figure 6.3 N_2 adsorption/desorption isotherms of P25, P90, 1.8% C-P25 and 1.9% C-P90.

SEM images for 1.9%C-P90 and 1.8%C-P25 shown in **Fig. 6.4** confirmed that 1.9%C-P90 is composed of primary nanoparticles with a particle size around 20~30 nm, while 1.8% C-P25 is composed of bigger size nanoparticles around 40~50 nm. The smaller particles will tend to form higher specific surface area. This is in consistent with the BET results that 1.9% C-P90 exhibits a higher specific surface area than 1.8% C-P25 does. There are short slit-pores formed by the TiO_2 particles overlaying, which is in good agreement with the N_2 sorption isotherms results. The X-ray elemental mapping results in **Fig. 6.5** suggest that the carbon species (red color) were well dispersed in the TiO_2 particles surface.
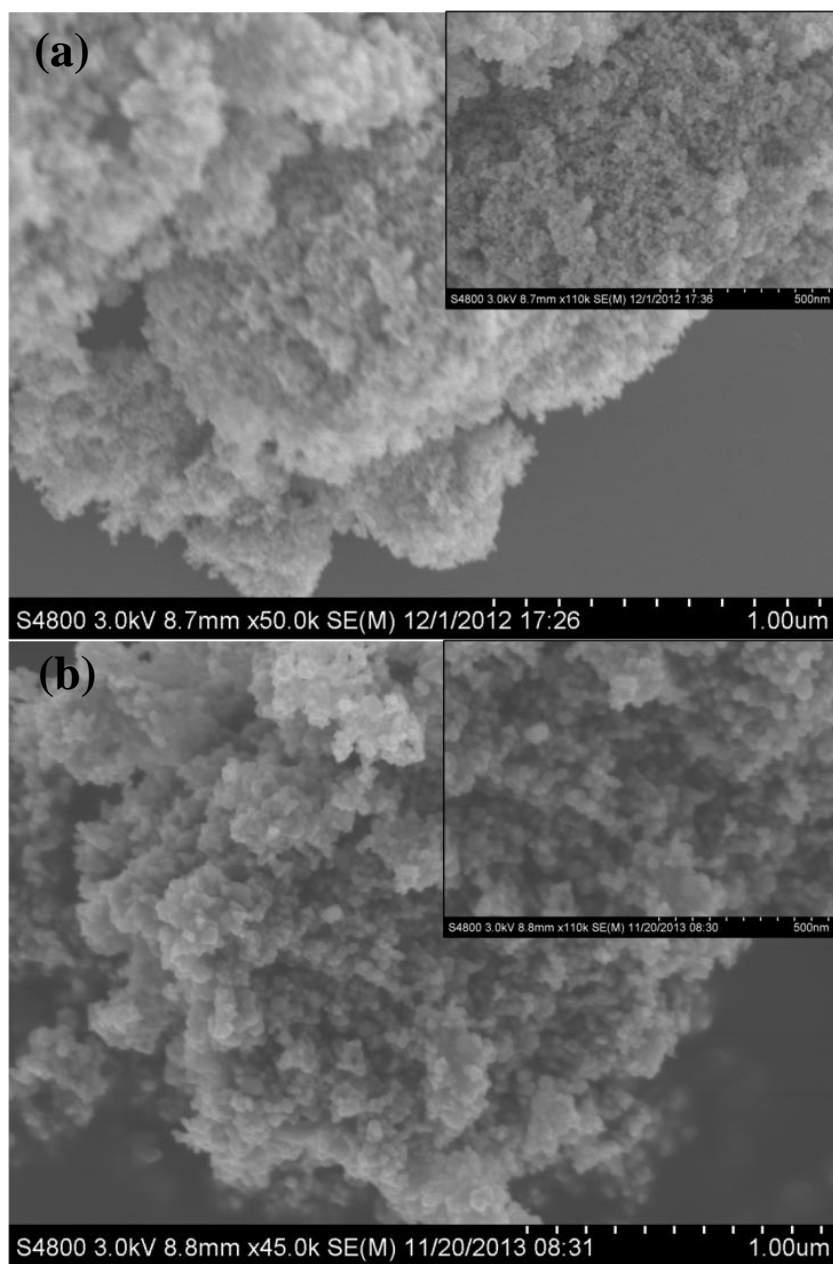
Figure 6.4 SEM Images of (a) 1.9% C-P90 and (b) 1.8% C-P25 (insets are different magnification images, respectively)
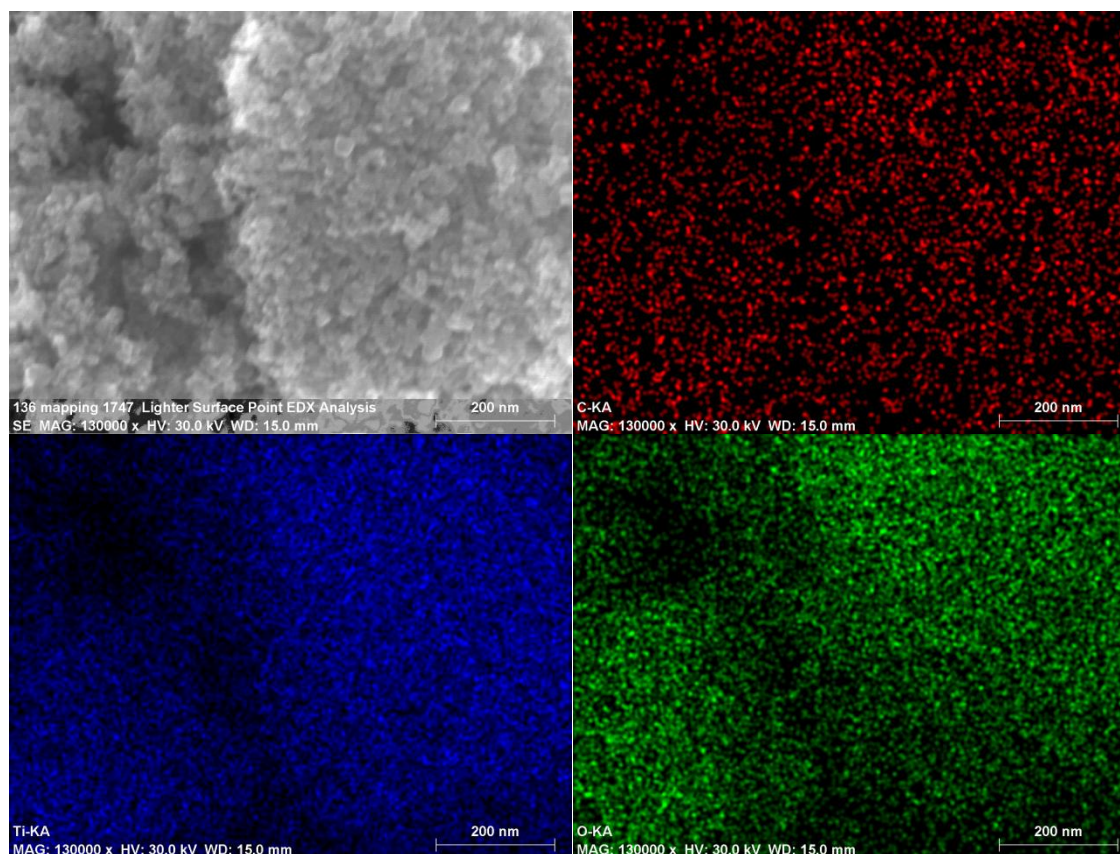
Figure 6.5 X-ray mapping images of 1.9% C-P90.

HRTEM was conducted on 1.9%C-P90 and 9.5%C-P90 to explore the location and thickness of carbon layers. **Fig. 6.6** shows that clear lattice fringes of nanocrystal with an interplanar space of 0.35 nm were observed on 1.9% C-P90 and 9.5% C-P90, which correspond to the (101) plane of anatase TiO_2. The lattice fringes of rutile TiO_2 were not seen under the observed projections that could be explained by the small fraction amount rutile phase. Carbon existence can be evidenced by the sample color (inset picture in **Fig. 6.6a**). Fig. 6a exhibited a thin carbon layer on some particles of TiO_2 with a thickness of ~0.4 nm (pointed out with blue arrows). In **Fig. 6.6a**, some crystalline particles (circled with dashed red line) with no continuous layer can also be observed. It can be confirmed that this continuous edge is carbon layer on the proof of the appearance comparison of coated and uncoated crystalline particles. In contrast, **Fig. 6.6b** showed a thicker carbon

layer which was around 5 nm on 9.5% C-P90. As carbon concentration increases, it tends
to form a layer on TiO_2 particles. The layer becomes thicker as the carbon content increases.
No lattice fringes were observed for the carbon layer which indicated carbon species were
composed of amorphous carbon.
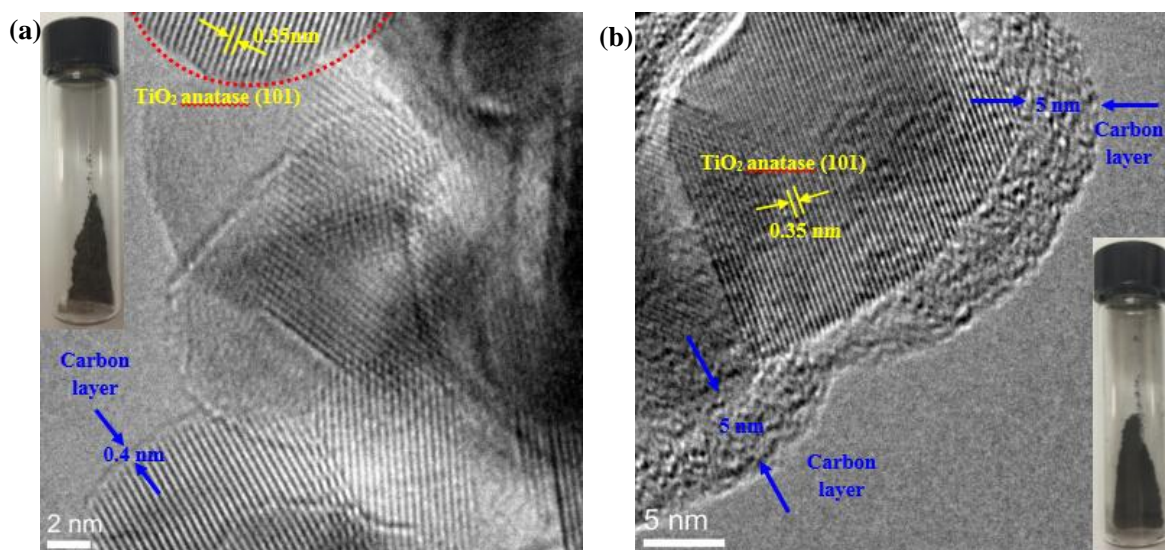
Figure 6.6 HRTEM images of (a) 1.9% C-P90, and (b) 9.5% C-P90.
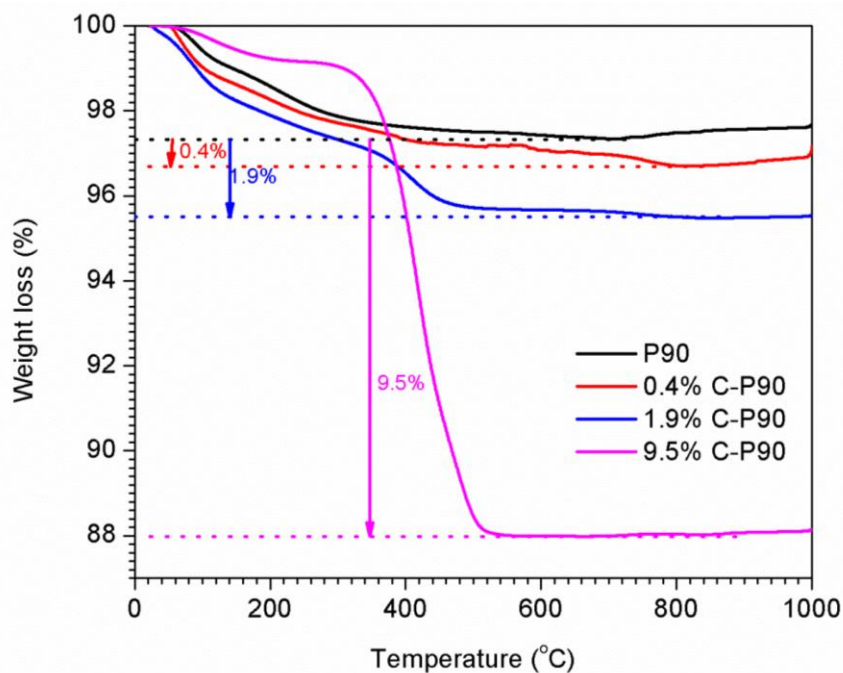
Figure 6.7 Thermogravimetry analysis (TGA) for P90 and C-P90 with various carbon concentration

The carbon content of C-P90 samples were confirmed using thermogravmetric analysis (TGA) (**Fig. 6.7**). The samples were heated from 25 °C to 800 °C at a rate of 10 °C min^{-1}. There are two steps weight loss of C-P90 samples in the temperature range between 25 and 800 °C. The weight loss below 200 °C is due to the adsorbed water while weight loss between 200 °C and 800 °C is attributed to the decomposition of amorphous carbon. The weight loss was estimated 0.4, 1.9 and 9.5 wt% of the total weight for various C-P90 materials in the range of 200-800 °C. It is noted that the carbon concentration on TiO$_2$ can be tuned via this simple preparation procedure.
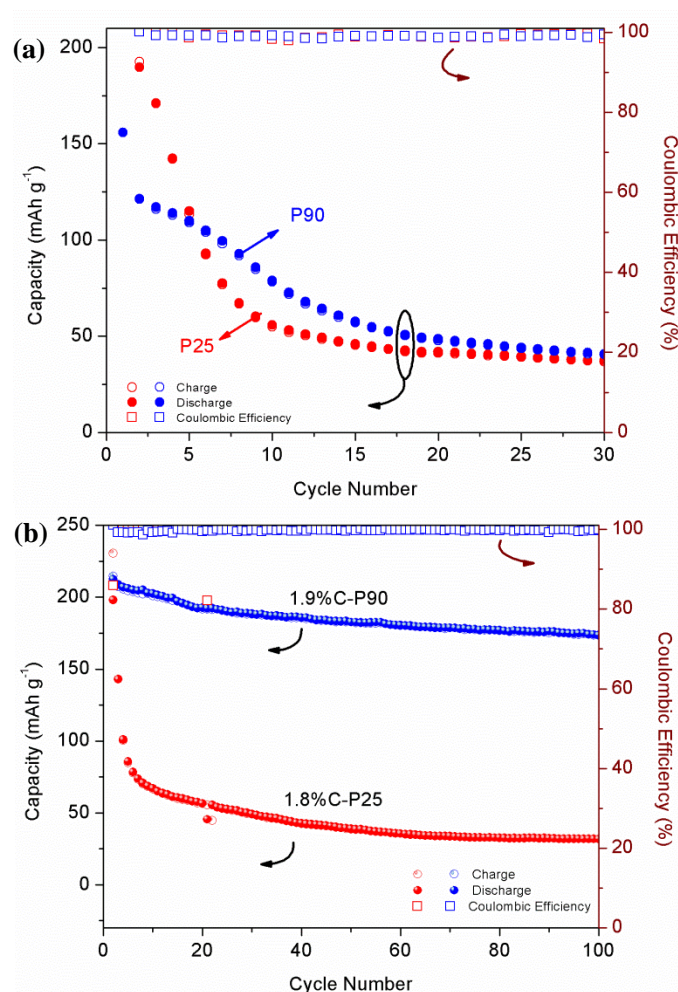
Figure 6.8 Cycling performance of (a) pristine TiO$_2$ (P25 and P90) and (b) C-TiO$_2$ (1.8% C-P25 and 1.9% C-P90) nanocomposites at a current density of 30 mA g^{-1}.

To investigate the effects of crystal phases and carbon deposition on lithium storage performances of TiO_2, two common commercial TiO_2 P25, TiO_2 P90, 1.8% C-P25 and 1.9% C-P90 s were assembled in cells and tested in the range of 1.0-3.0 V at a 30 mA g^{-1} current density. **Fig. 6.8a** shows the electrical performance of pure TiO_2. Both P25 and P90 electrodes showed a fast capacity fading from 200 mAh/g to 50 mAh/g in the initial 30 cycles, possibly due to the intrinsically poor electronic conductivity of pristine TiO_2. Li^+ insertion/ extraction into/out of TiO_2 mechanism can be expressed as TiO_2 $+x(Li^++e^-)\leftrightarrow Li_xTiO_2$, where x depends on the materials crystallography and microstructure. And x is limited to 0.5 for pure TiO_2 due to its poor electronic conductivity and Li^+ diffusivity.[166] Interestingly, depositing carbon (1.8%) on P25 induced a high initial discharge capacity of 260 mA h g^{-1}, but still suffers from the capacity fading problem, as shown in **Fig. 6.8b**. By contrast, 1.9% C-P90 exhibited an initial discharge capacity of 231 mA h g^{-1} ($0.7Li^+$) and an excellent cyclic performance. The capacity was retained at 173 mA h g^{-1} after 100 cycles (75% retention), much superior to pure TiO2 and 1.8%C-P25. The superiority of 1.9% C-P29 was probably due to two reasons. First, as the carbon concentration on both samples is almost the same, the drastic capacity decay of 1.8% C-P25 can be ascribed to the higher rutile phase fraction in the structure of TiO_2 which largely influence the electrochemical performance. It is reported that the diffusion coefficient of Li^+ ions in rutile TiO_2 (1.42×10^{-13} cm^2 s^{-1}), which is smaller than that of anatase TiO_2 (1.81 $\times10^{-13}$ cm^2 s^{-1}).[167] This can be possibly explained that the channels of rutile TiO_2 are narrower than those of anatase TiO_2, which is proved by the superior electrochemical performance of 1.9% C-P90 due to its less rutile phase fraction and more anatase phase fraction. Second, the higher specific surface area of 1.9% C-P90 than that of 1.8% C-P25

helps to store more Li$^+$ ions to a certain extent. [168]
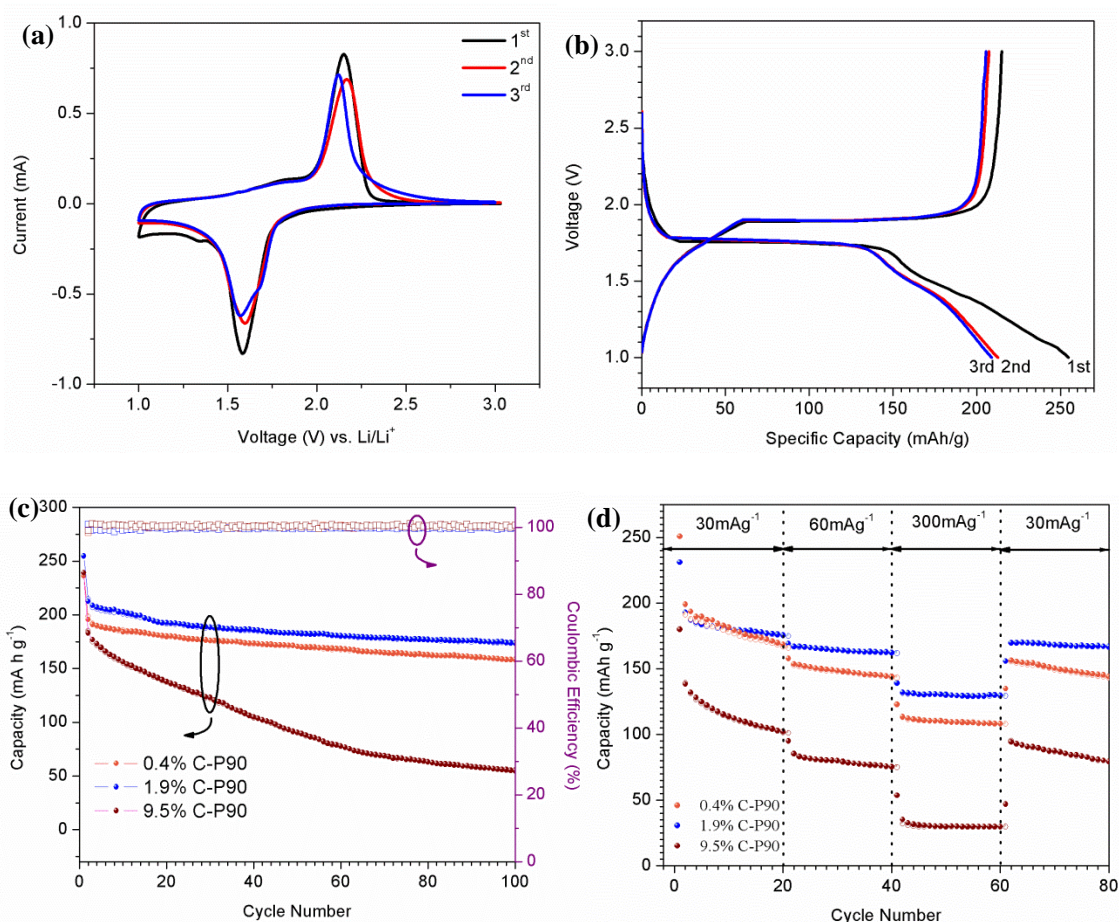
Figure 6.9 Electrochemical performance of (a) Representative cyclic voltammograms (CV) of 1.9% C-P90 sample at a scan rate of 0.2 mV s^{-1} between 1 V and 3 V; (b) Charge-discharge voltage profiles of the first 3 cycles for 1.9% C-P90 at 30 mA g^{-1}; (c) performance of C-P90 nanocomposites at 30 mA g^{-1}; (d) Rate capability of C-P90 nanocomposites at difference rates;

Fig. 6.9 a shows representative cyclic voltammograms (CV) of 1.9% C-P90. It is obvious that the sample demonstrates a CV curve pattern with a pair of redox peaks indicating the Li+ insertion (cathodic sweep, 1.51 V) and Li$^+$ extraction (anodic sweep, 2.15 V) into and out of TiO$_2$ processes. The cathodic and anodic peaks from CV are in close correspondence with the voltage plateaus obtained from the galvanostatic cycling in **Fig. 6.9 b**. This result is consistent with the results reported in the literature.[169] The anodic peak with almost the same current density as the cathodic peak proves that the Li$^+$ ions

extraction takes place to the equal extent, indicating a nearly perfect Coulombic efficiency. Furthermore, the galvanostatic charge-discharge curve in **Fig. 6.9 a** shows no substantial change after 2nd cycles, showing the high reversibility of the Li^+ insertion/extraction reactions.

Due to the superior electrochemical performance of C-P90, we further studied different C-P90 materials in order to optimize the electrochemical performance by tuning the carbon concentration. **Fig. 6.9 c** showed the cycling performance of various C-P90 at a current density of 30 mA g^{-1}. 0.4% C-P90 exhibited a relatively lower cycling capacity, although its initial capacity is higher (255 mA h g^{-1}). The lower cycling capacity can be explained by that less carbon decoration on P90 is ineffective to provide electronic conductivity. As the carbon concentration increased from 1.9% to 9.5%, an even poor cycling performance was exhibited. Only 55 mA h g^{-1} capacity was retained after 100 cycles for 9.5% C-P90.

Fig. 6.9 d showed the cycling performance at different current density (30 mA g^{-1}, 60 mA g^{-1}, 300 mA g^{-1} and 30 mA g^{-1}). 1.9%C-P90 has superior rate capability comparing with 0.4%C-P90 or 9.5%C-P90 materials, which also proves the proposal reason that the optimized carbon concentration improves the electronic conductivity. 1.9%C-P90 exhibited the best cyclabiliy and rate capability comparing with 0.4%C-P90 and 9.5%C-P90. The electrochemical performance that 1.9%C-P90 possesses is even comparable to some hierarchical carbon-TiO_2 composites reported in some literature. As mentioned above, 1.9% C-P90 exhibited a high initial discharge capacity of 231 mA h g^{-1} at a current density of 30 mA g^{-1} and a capacity of 130 mA h g^{-1} at a current density of 300 mA g^{-1}.
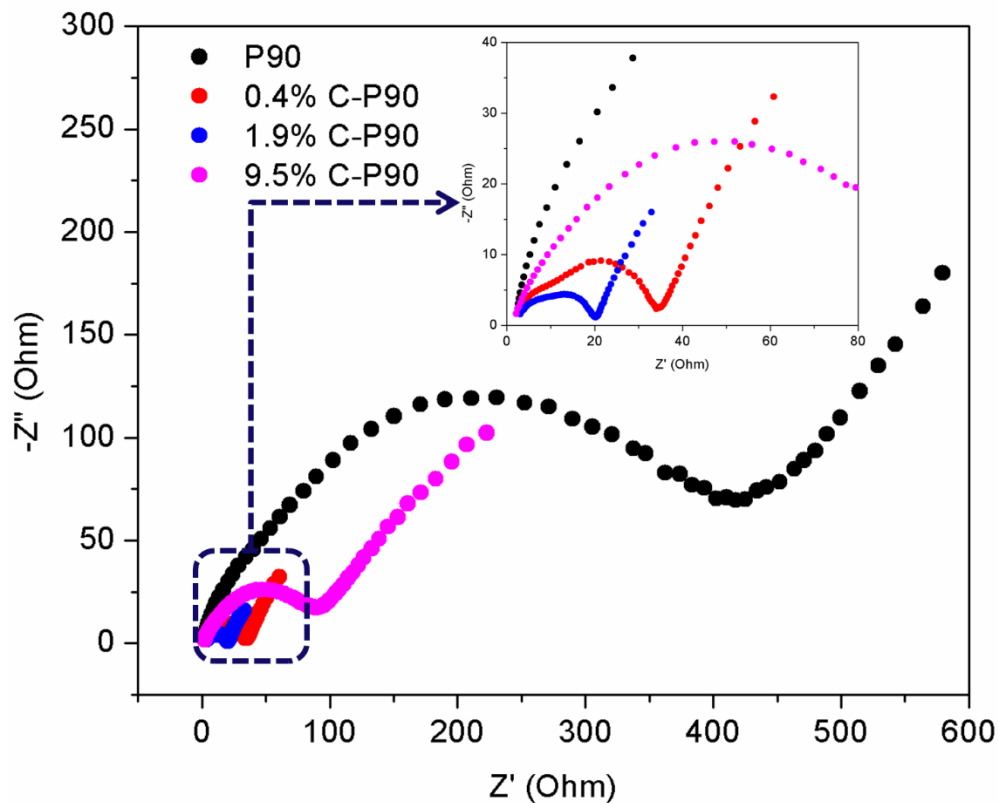
Figure 6.10 Electrochemical impedance spectra of carbon decorated TiO_2 (P90)

Electrochemical impedance experiments were applied to explore the effect of carbon decoration on TiO_2 (P90) nanoparticles on the interface impedance of C-TiO_2 composites. **Fig. 6.10** shows the Nyquist plots of the carbon decorated TiO_2 (P90) particles after 3 cycles charge-discharge process. The semicircle in the intermediate frequency is related to the charge transfer resistance at the electrode/electrolyte interface, while the sloping line at the low frequency end represents the Warburg impedance caused by a semi-infinite diffusion of Li^+ ion in the electrode.[170-172] It can be seen clearly that the interfacial resistance (R_{ct}) is much smaller for the C-P90 electrode than for the pristine P90 electrode, which indicates that carbon decoration could enable much easier charge transfer at the electrode and electrolyte interface. As a result, carbon decoration decreases the overall battery internal resistance. For various carbon concentration electrode C-P90, the

interfacial resistance is with this order $R_{ct\ 1.9\%\ C\text{-}P90} < R_{ct\ 0.4\%\ C\text{-}P90} < R_{ct\ 9.5\%\ C\text{-}P90}$. It shows that less carbon concentration (e.g. 0.4%) is unable to provide good conductivity, while more carbon integration (e.g. 9.5%) into TiO_2 can increase charge transfer resistance.[173] This can explain that 1.9% C-P90 exhibits the best electrochemical performance due to the optimum carbon concentration.

Comparing with the reported results in the open literature, 1.9%C-P90 prepared with a simpler method, which exhibited a very promising electrochemical performance result. Shen, et al.[143] reported a three dimensional coherent titania-mesoporous carbon nanocomposite, which was prepared by a template method. This material exhibited a reversible capacity of ~150 mA h g^{-1} at a current density of 200 mA h g^{-1}. Zhen, et al.[166] studied a TiO_2 on reduced graphene oxides composite, which was synthesized by a two-step hydrothermal method. This composites performed a 200 mA h g^{-1} capacity at 1.2 C (1 C=167.5 mA g^{-1}). Liu, et al.[174] prepared a sandwich-like TiO_2-carbon hollow sphere structure composite via two-step hydrothermal method, which exhibited a 200 mA h g^{-1} capacity at 1 C. These reported materials were either synthesized by hydrothermal, template method or involved with organic precursors as carbon source. In comparison, our C-P90 sample is prepared by one-step carbonization at mild conditions with commercial materials. 1.9% C-P90 material exhibited a comparable performance mainly due to its unique carbon decoration nanostructure and anatase-rutile phase composition that facilitate efficient lithium insertion and extraction.

To illustrate the mechanism of carbon layer function on TiO_2 P90, **Fig. 6.11** shows the scheme according to the characterization results. At lower carbon concentration (0.4%), carbon cannot form a uniform layer on TiO_2 P90 nanoparticles, which results in poor

conductivity. At higher carbon concentration (9.5%), it tends to form a thicker layer on TiO$_2$ P90 nanoparticles, which inhibits Li$^+$ insertion/extraction. By comparison, on the TiO$_2$ P90 with moderate carbon content materials, carbon layer provides conductivity for the composites and the thickness of which enables Li$^+$ insert into TiO$_2$.
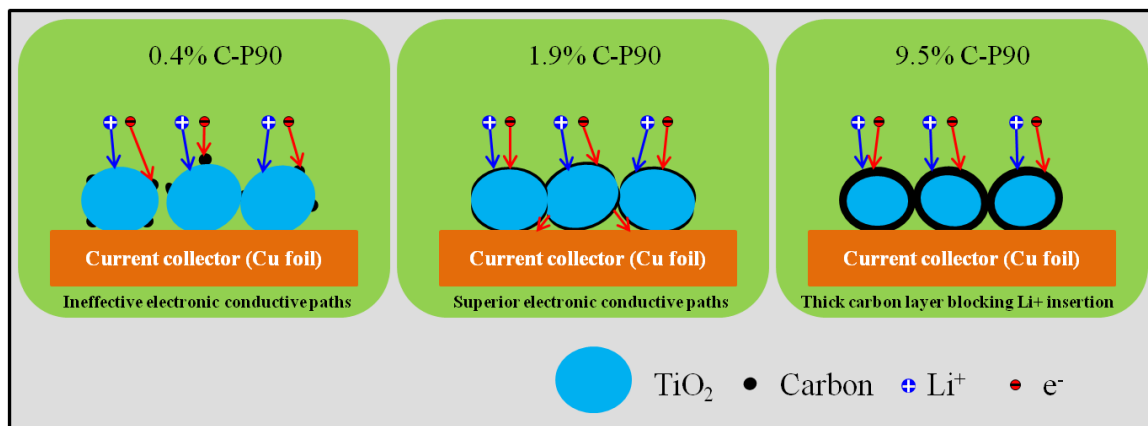
Figure 6.11 Schematic representation of the nanostructure and lithium ion insertion and electron transport of the C-P90 nanocomposites.

6.4 Conclusion

In conclusion, carbon decorated TiO$_2$ were synthesized using commercial TiO$_2$ product (P25 and P90) in large scale through a simple carbonization process. C-P90 possesses higher specific area and larger fraction of anatase comparing to C-P25 with the same carbon concentration, which guaranteed its superior electrochemical performance as anode for LIBs. Carbon concentration had been optimized to obtain the best battery performance for P90. 1.9% C-P90 showed a significant stable cyclablity which was attributed to its unique carbon decoration nanostructure that facilitates efficient lithium insertion and extraction. The easy preparation together with the advantage of stable cyclability of C-P90 makes the composite a very promising anode material for LIBs.

CHAPTER 7 HIERARCHICAL SULFUR-INFILTRATED POROUS MICROSPHERES CARBON FOR HIGH ENERGY LITHIUM-SULFUR BATTERIES

7.1 Introduction

As mentioned in Chapter 1, scientists fabricated different carbon framework to constrain sulfur to obtain better performance cathode for lithium-sulfur batteries. Regardless of the various carbon frameworks, pore structure and sizes are important factors that determine the electrochemical performance. So far, only a few studies reported sulfur/carbon composites with a bi-modal or tri-modal pore structure as cathodes for Li-S batteries.[57, 175-176] Schuster et al.[57] developed a spherical ordered bi-modal (3.1 nm and 6 nm) mesoporous carbon/sulfur nanocomposite, and they claimed that the bimodal pore distribution and nano-carbon dimensions were beneficial for more sulfur incorporation and improved electrolyte accessibility compared with single pore size structure, resulting in an initial discharge capacity at 1,200 mA h g^{-1} and 730 mA h g^{-1} after 100 cycles at 1 C rate. On the other hand, it has been reported that Li$^+$ diffusion within an ordered porous sulfur/carbon framework may be inhibited or limited due to fully or partially filled carbon pores by sulfur.[175] Moreover, for high-rate electrochemical performance, mesopores larger than 10 nm or even macropores are required for better electrolyte diffusion and fast ion transport. [175, 177]

However, no research has aimed to integrate micropores, mesopores and macropores in a single carbon framework with a controllable manner to achieve a satisfied electrochemical performance for Li-S batteries. In this work, we have designed and fabricated a novel 3D multi-modal porous microsphere carbon framework (PMC) that

integrates interconnected micropores, mesopores, and macropores with easily tunable pore size distribution. The pore distribution can be controlled by adjusting the silica nanoparticles (NPs) sizes (40 and 10 nm) and the ratio of different sized silica NPs. Unlike conventional wet-chemistry methods to prepare porous carbon, an aerosol-based spray pyrolysis method was used in this work to synthesize the multi-modal PMC (see **Fig. 7.1**).
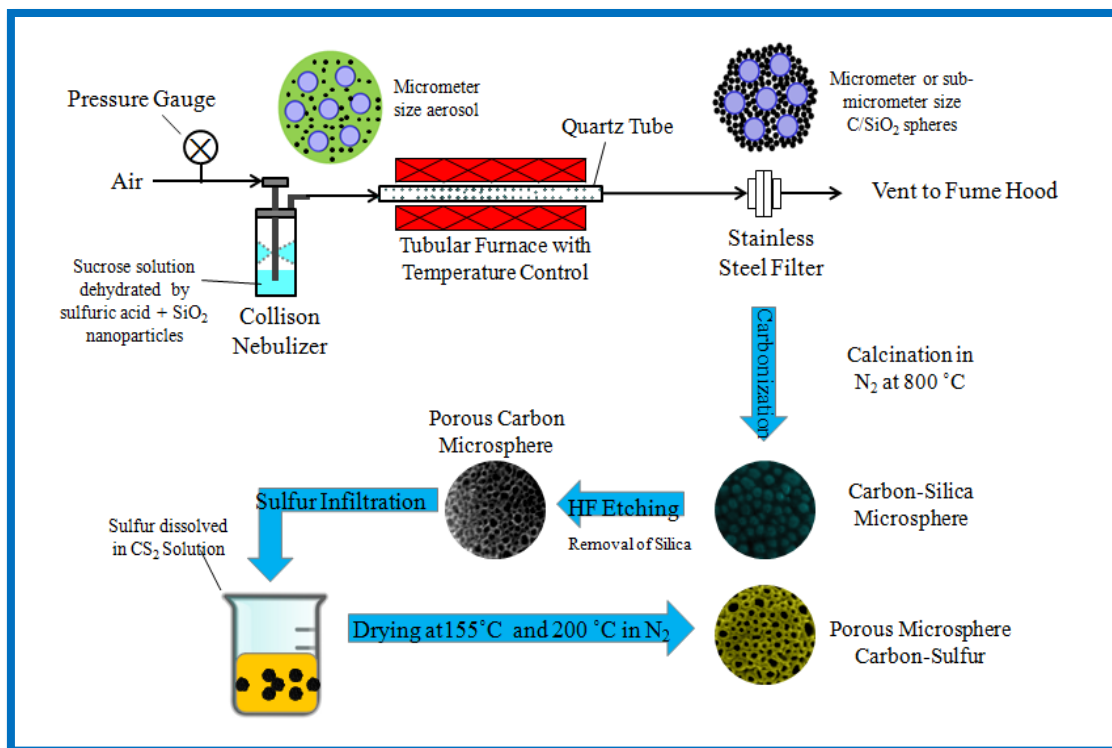
Figure 7.1 Schematic of experimental setup and process for synthesizing porous carbon/sulfur microspheres.

7.2 Experimental Method and Characterization

Porous Microsphere Carbon (PMC): The PMC was synthesized through a spray pyrolysis method with the aid of silica templates. In brief, a mixture of 4.2 g sucrose and 20 ml 20 wt.% silica sol (Nissan Chemical) with 1:2 weight ratio of carbon/silica was first prepared. 0.25 ml 95% sulfuric acid was then added into the evenly mixed solution. The solution was then heated up to 90 ˚C in an oil bath under vigorous stirring. The round-

bottom flask was equipped with a cooling water reflux condenser to condense the vapor and ensure a constant solution amount in the flask. After reflux for 30 h for sucrose carbonization, the solution was then transferred to a Collison nebulizer (BGI Inc.) for spray pyrolysis through a cylindrical quartz tube placed inside a tube furnace. The tube furnace temperature was set at 600 ˚C during spray pyrolysis and compressed air was used as the carrier gas. Powder samples were collected on a glass fiber filter and then finally were calcined in N_2 at 800 ˚C for 4 hours. Carbon/silica (C/SiO_2) microspheres were thus obtained. The PMC was produced by removing the silica templates in a 10% HF solution. Silica sols with different particle sizes (mode at 40 nm or 10 nm, or a mixture of 40/10 nm at 1:1 volume ratio) were used as templates for PMC. The PMC materials using different silica NP sizes were denoted as PMC-40, PMC-10, and PMC-40:10, respectively.

Porous Microsphere Carbon loaded with Sulfur (PMC/S): Elemental sulfur (SigmaAldrich, 99.99%) was loaded onto the PMC via liquid phase infiltration by using a freshly made solution of sulfur in carbon desulfide (CS_2). The infiltration of sulfur was carried out through impregnation and drying process to obtain samples with designated loadings. After each cycle of impregnation and drying, the sample was annealed at 155˚C for 1 hour and 200˚C for another hour in the N_2 atmosphere. Typically, five such cycles were applied to reach the desired total loading of sulfur. The corresponding PMC/S materials using different size silica as templates were denoted as PMC/S-40, PMC/S-10, and PMC/S-40:10, respectively.

The thermal stability of electrode materials were carried out on a thermalgravimetric analyzer (TGA-DAT-2960 SDT) at a heating rate of 20 ˚C min^{-1} from 25 to 500 ˚C in argon. Scanning electron microscopy (SEM) equipped with energy-

dispersive X-ray (EDX) spectroscopy (Hitachi S4800) was used to analyze the material morphology and elemental composition. To carry out x-ray elemental mapping on a cross section of the PMC/S, we used a special resin to embed the PMC/S sample and prepared SEM specimen according to the method reported by Holdorf et al. [178] The Brunauer-Emmett-Teller (BET) specific surface area of the composites was measured by nitrogen adsorption at 77 K on a surface area and porosity analyzer (Micrometrics ASAP 2020). Before each adsorption measurement, 0.10 g PMC sample was degassed at 300 °C for 4 h. It is not possible to follow the conventional protocol to degas the PMC/S samples above 155 °C before BET measurements owing to the volatility of the sulfur, and thus no pretreatment was done for PMC/S. The pore size distribution plot was derived from the adsorption branch of the isotherm based on the density functional theory (DFT).

The active material powder was mixed with carbon black and Poly(vinylydene fluoride), PVDF, dissolved in n-methyl pyrolidinone, NMP, 8 wt.%, in a weight ratio 75:15:10. The slurry was mixed to obtain a homogeneous black paste which was then coated on an aluminum foil. The as-coated aluminum foils were dried under vacuum at 60°C for 1 h. The working electrode and Li metal foil counter electrode were assembled into coin cells by using Celgard 2400 as the separator and 1 M LiTFSI in DOL/DME 50:50 was used as the electrolyte. The cells were constructed in an Argon-filled glove box. The charge/discharge curves were measured using an Arbin potentiostat at a cutoff voltage of 1.5-3.0 V under a current density of 1 C. The specific capacity and current density were calculated based on sulfur mass only. Cyclic voltammetric curves were recorded in a voltage range of 1.5-2.8 V at a scan rate of 0.1 mV s^{-1}. The electrochemical impedance spectra were recorded by applying an alternating current of 5 mV in a frequency range

from 1 Hz to 100 kHz.

7.3 Results and Discussion

Scanning electron microscopy (SEM) coupled with energy-dispersive X-ray (EDX) spectroscopy were employed to identify the morphology, pore structure, and the distribution of sulfur in the 3D multi-modal PMC/S. **Fig. 7.2a** shows C/SiO$_2$-40 microspheres where 40 nm silica NPs are clearly seen imbedded in a carbon matrix. **Fig. 7.2b** shows porous carbon microspheres (PMC-40) after 40 nm silica templates were etched out. Because silica NPs have a size range of 30 to 50 nm with a mode diameter of 40 nm, some size variation of the pores is discernible. EDX analysis was conducted, and no Si was present on the PMC-40. PMC-40 could be completely burned off, further confirming silica templates were completely removed.   This also suggests that the carbon walls in between the silica NPs were porous, allowing HF etching solution to penetrate into the entire microsphere. **Fig. 7.2c** and its inset show the SEM image of PMC-10, which is composed of smaller pores (~10 nm). SEM images of PMC-40:10, prepared by using mixed 40 and 10 nm silica templates at 1:1 ratio, are exhibited in **Fig. 7.2d-f**. Figure 1d clearly shows a mixed larger pores and smaller pores on the surface of PMC-40:10, agreeing well with the pore sizes of the two silica NP templates. The inner structure of the porous framework can be identified by a broken microsphere of PMC-40:10 (**Fig. 7.2e**) and a magnified image (**Fig. 7.2f**). Because of the equal total volume of 40 and 10 nm pores, the number of 10 nm pores is far more than that of the 40 nm pores. Hence, one can see that the large pores are surrounded by many smaller pores, and the smaller pores themselves are connected by carbon walls that are microporous (see pore size analysis in a later section).
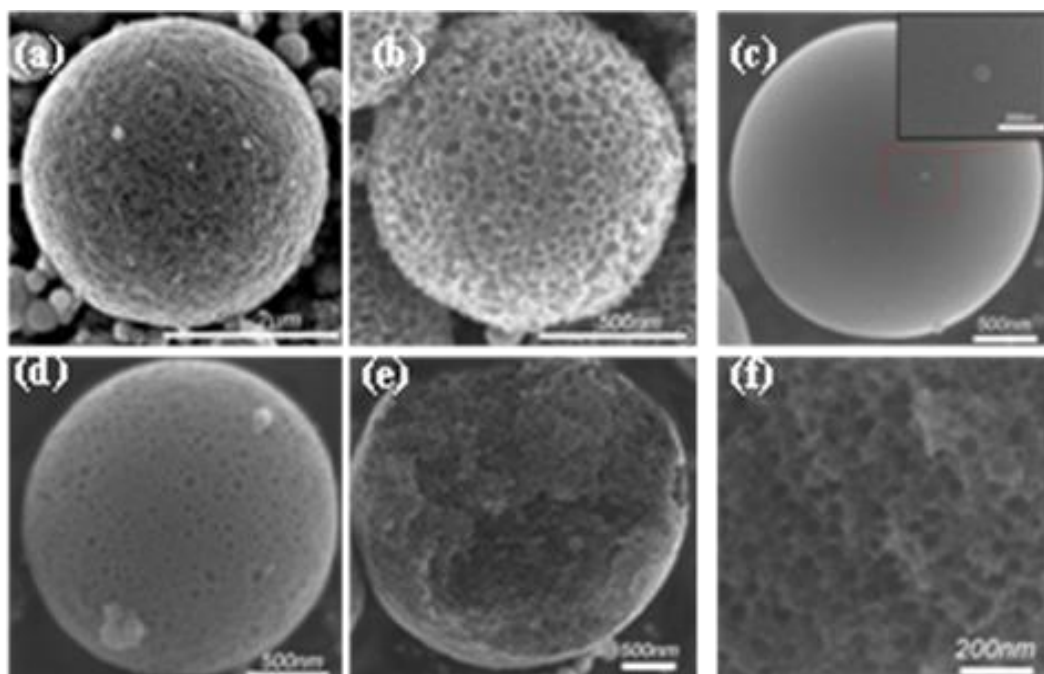
Figure 7.2 SEM Images of (a) C/SiO_2-40, (b) PMC-40, (c) PMC-10 (inset showing magnified surface pore structures), (d) PMC-40:10, (e) PMC-40:10 with exposed inner surface, and (f) magnified image of PMC-40:10 inner pore structure.

The interconnected pores, although at different sizes, ensure uniform sulfur loading, and a high sulfur concentration is achievable. Upon sulfur infiltration and infusion, the pores on PMC-40 were partially occupied by sulfur without changing the spherical morphology (**Fig. 7.3a**). **Fig. 7.3b** shows the corresponding SEM image of PMC/S-40:10. After sulfur infiltration, the larger pores on PMC/S-40:10 still remain open, while the smaller pores were fully or partially blocked. The SEM image of PMC/S-10 is shown in **Fig. 7.3c**, which suggests that sulfur fully covered the surface due to the small pore size not easily discernible from SEM images. EDX and X-ray elemental mapping (XREM) results (see **Fig. 7.4**) demonstrate that carbon and sulfur are evenly distributed on the microsphere. To confirm the distribution of sulfur within the porous carbon, the PMC/S-40 sample was cut in the middle and its cross section was subject to XREM (see **Fig. 7.5**). The results confirm that sulfur was also uniformly dispersed in the entire inner pores of the

carbon framework. The sulfur weight percentage in the PMC/S composites ranged from

60.5% to 63.9% for the three samples
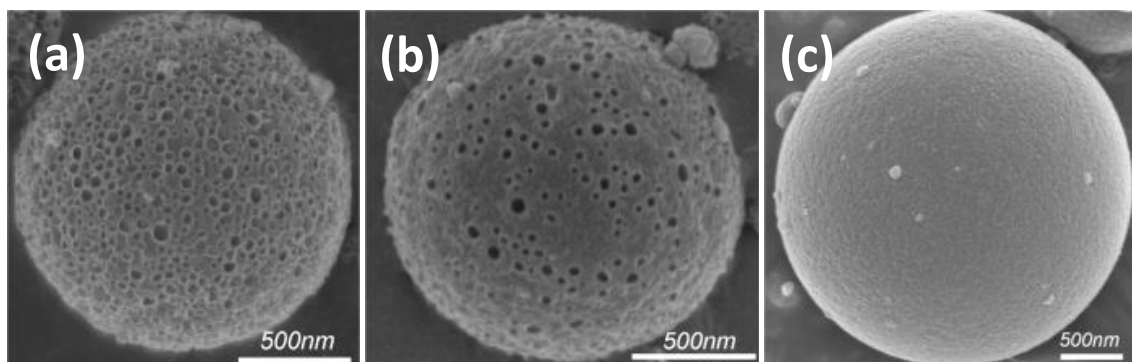
Figure 7.3 SEM Images of (a) PMC/S-40, (b) PMC/S-40:10, and (c) PMC/S-10
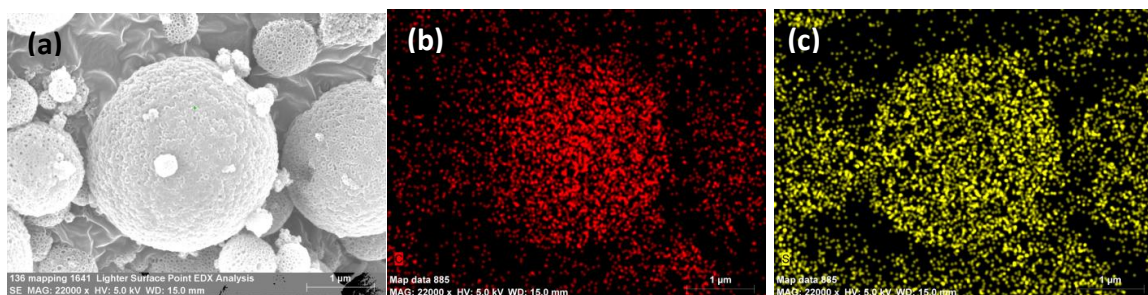
Figure 7.4 SEM image (a), and X-ray elemental mapping of PMC/S-40: (b) Carbon element, and (c) Sulfur element.
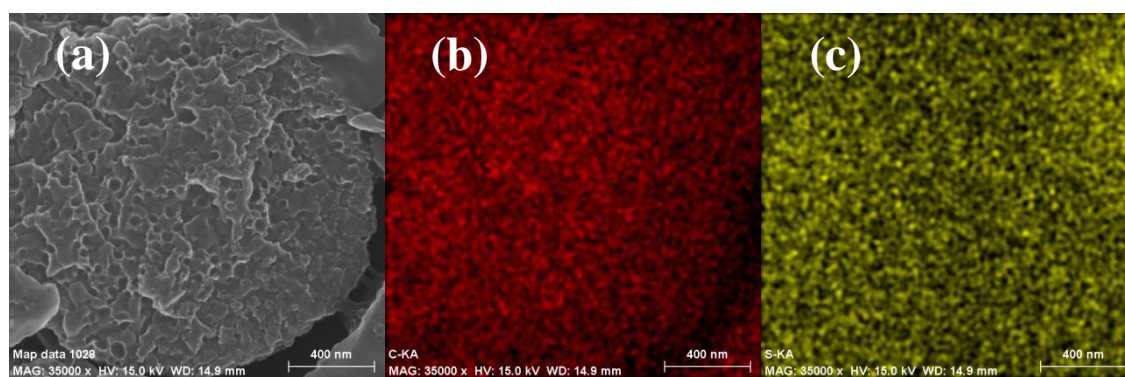
Figure 7.5 SEM image of the cross-section of PMC/S-40 (a), and X-ray elemental mapping images of the cross section of PMC/S-40: (b) carbon element, (c) sulfur element.

Fig. 7.6 shows the XRD patterns of the pristine sulfur and PMC/S composites. The

sharp diffraction peaks centered at $2\theta = 23.4°$ and $28.0°$ in the XRD pattern of pristine

sulfur match well with orthorhomic phase sulfur (JCPDS no. 08-0247).[179] The XRD patterns for PMC/S composites are quite different from that of pristine sulfur. Only one broad peak can be observed at about 23.0˚ represents the presence of partially graphitized carbon structure in PMC. Sulfur diffraction peaks completely disappear for all the PMC/S composites, which suggests that sulfur is highly dispersed inside the pores of the carbon microsphere.[73]
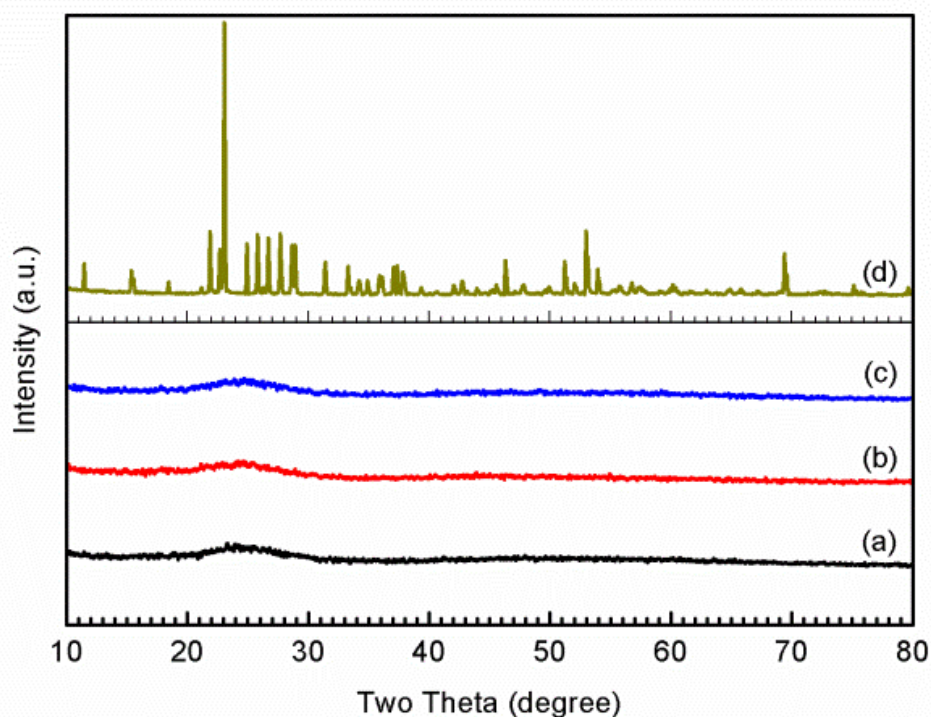
Figure 7.6 XRD patterns of (a) PMC/S-40, (b) PMC/S-40:10, (c) PMC/S-10, and (d) pristine sulfur

Table 7.1 summarizes the physical characteristics of PMC and PMC/S nanocomposites derived from Brunauer-Emmett-Teller (BET) measurements. T-plot method, the most commonly method to determine the properties of microporous materials, is used to indicate micropore surface area and micropore volume of the PMC and PMC/S composites. The PMC materials have high specific surface areas and large pore volumes. Significantly, PMC-10 has an extraordinary high specific surface area of 2,776 m^2 g^{-1},

followed by PMC-40:10 at 2,485 m^2 g^{-1} and PMC-40 at 1,236 m^2 g^{-1}. After sulfur infiltration in the porous carbon, the specific surface area and pore volume decrease remarkably, indicating that the pores of PMC are partially filled.

Table 7.1 BET specific surface area and pore volume of PMC and PMC/S nanocomposites

Samples	BET specific surface area (m^2 g^{-1})	Pore volume (cm^3 g^{-1})	Micropore surface area (m^2 g^{-1})
PMC-40	1236	3.1	173
PMC-40:10	2485	5.1	118
PMC-10	2776	4.3	67
PMC/S-40	242	1.1	14.9
PMC/S-40:10	134	0.4	6.6
PMC/S-10	82	0.2	1.9

The porous structure and pore size distribution of PMC and PMC/S samples were investigated by N_2 adsorption-desorption isotherms. The results in **Fig. 7.7a** and **7.7b** show that both PMC and PMC/S materials had a typical IV-type isotherm, corresponding with a mesoporous structure. The sharp incremental of N_2 adsorption amount on the isotherms for PMC-40 and PMC-40:10 materials at the relative pressure $p/p_0 = 0.93–1.0$ indicates the existence of macroporosity.[74] PMC-10 exhibited no such characteristic sharp incremental N_2 adsorption at $p/p_0 = 0.93-1$ (i.e., absence of macropores) because only 10 nm template SiO_2 NPs were used. Compared with bare PMC in **Fig. 7.7a**, the quantity of adsorbed N_2 in **Fig. 7.7b** significantly decreased in PMC/S due to the sulfur infiltration into the porous carbon, in agreement with the BET measurements of specific surface area. The calculated pore size distribution (PSD) curves of PMC (**Fig. 7.8a**) and PMC/S (**Fig. 7.8b**) further reveal the feature of multi-modal porous structure. **Table 7.2** summarizes the pore size

distribution obtained from **Fig. 7.8**. All PMC samples had micropores around 1.5 nm, likely originated within the carbon walls (due to the interspaces of carbon nanoparticles and/or formed by gas releasing during HF etching). The macropores represented as a weak shoulder on the PSD curve at the mode of 55 nm for PMC-40 and PMC-40:10 are likely due to the relatively wide size range of silica NPs that contain a portion of NPs greater than 40 nm. Besides the sharp characteristic peaks around 10 and 40 nm, mesopores at other sizes are also observed. For the PMC/S composites, the micropores disappeared, indicating that micropores were fully occupied by sulfur. There are some new peaks (e.g. 20 nm) formed on PMC/S-40 and PMC/S-40:10, which are likely due to partial occupation of the 40 nm pores by sulfur.
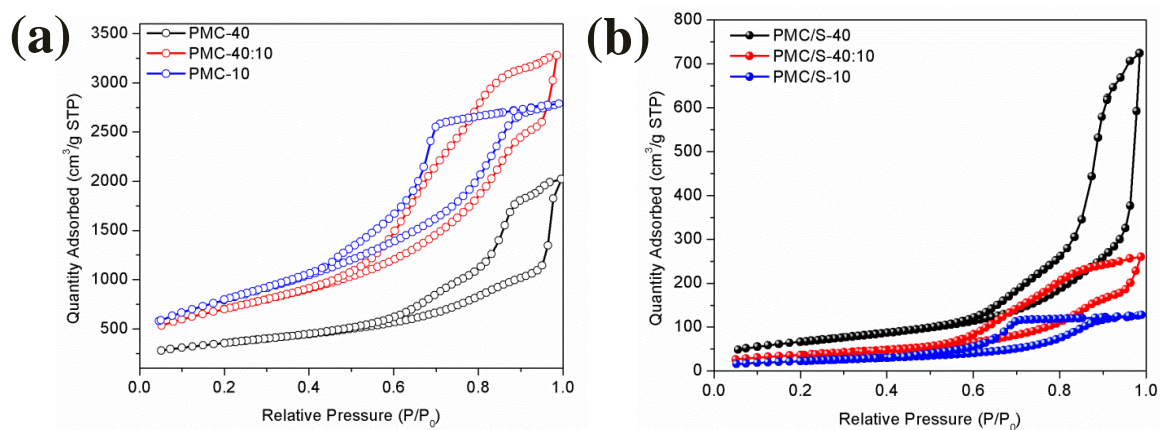
Figure 7.7 N_2 adsorption/desorption isotherms of (a) PMC and (b) PMC/S

Table 7.2 Summary of pore size distribution and modes for PMC and PMC/S nanocomposites

Samples	Micropores (< 2 nm)	Mesopores (2~50 nm)	Macropores (> 50 nm)
PMC-40	1.5	8, 36[D]	55
PMC-10	1.5	4, 10[D]	No
PMC-40:10	1.5	6, 10[D], 30~44[D]	55
PMC/S-40	No	9, 14, 20, 32~44[D]	55
PMC/S-10	No	9[D]	No
PMC/S-40:10	No	9[D], 20, 28~40[D]	55

Note: "(D)" indicates dominating pore size mode.
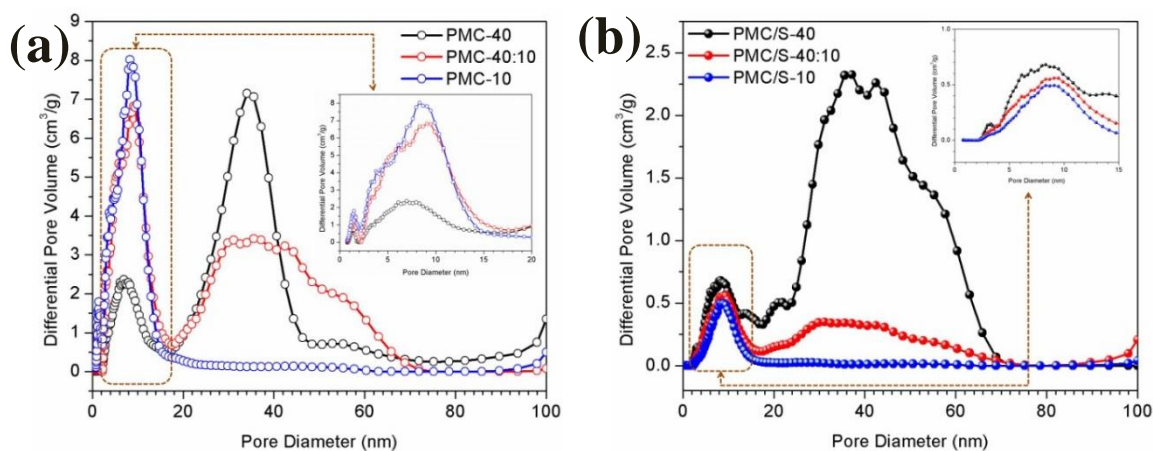
Figure 7.8 Pore size distribution of (a) PMC and (b) PMC/S (insets showing magnified pore size distribution in the dashed rectangular area)

Fig. 7.9a shows the charge/discharge voltage profile for the initial cycle of PMC/S at a high current density rate of 1 C (1 C = 1,675 mA g^{-1}). Two voltage plateaus during the discharge process can be observed for all PMC/S materials. An impressive high initial discharge capacity of 1,278 mAh g^{-1} was achieved on PMC/S-40:10, corresponding with 76.3 % of the theoretical capacity of sulfur. In comparison, PMC/S-40 and PMC/S-10 exhibited an initial discharge capacity of 1,158 mAh g^{-1} and 940 mAh g^{-1}, respectively, lower than that of PMC/S-40:10.

The rate capability of the PMC/S composites at various current densities from C/10 to 2C is shown in **Fig. 7.9b**. PMC/S-40:10 composite shows an excellent rate performance, with specific capacities of 1462, 1053, 937, 855, 778 mAh g^{-1} at C/10, C/5, C/2, 1C and 2C, respectively. PMC/S-40:10 exhibits the highest capability at all rates compared with PMC/S-40 and PMC/S-10. In addition, the superior rate capability of PMC/S-40:10 is also demonstrated by the easier recovery of capacity when the current density was changed from 2C to C/10 at the end of the test.

Cycle performance and Coulombic efficiency of the three samples and pristine sulfur were compared over 100 cycles at 1 C rate, as shown in **Fig. 7.9c**. The initial discharge capacity follows the order of PMC/S-40:10 > PMC/S-40 > PMC/S-10 > sulfur. The discharge capacities at the 100th cycle were 904, 660, 680 and 419 mAh g^{-1} for PMC/S-40:10, PMC/S-40, PMC/S-10, and sulfur, respectively. Again, in agreement with the trend as seen in the rate capability performance, the PMC/S-40:10 had the best long term performance, with 70.7% capacity retention after 100 cycles compared with its initial capacity. For PMC/S-40:10, the initial Coulombic efficiency was 98.4% and slightly dropped to 90% after 40 cycles, but remained stable thereafter at around 90%. As comparison, PMC/S-40 and PMC/S-10 had a Coulombic efficiency of 88% and 87%, respectively, over 100 cycles. The results indicate that all the PMC/S samples exhibited superior cycle performance and mitigated shuttle effect compared with pristine sulfur.
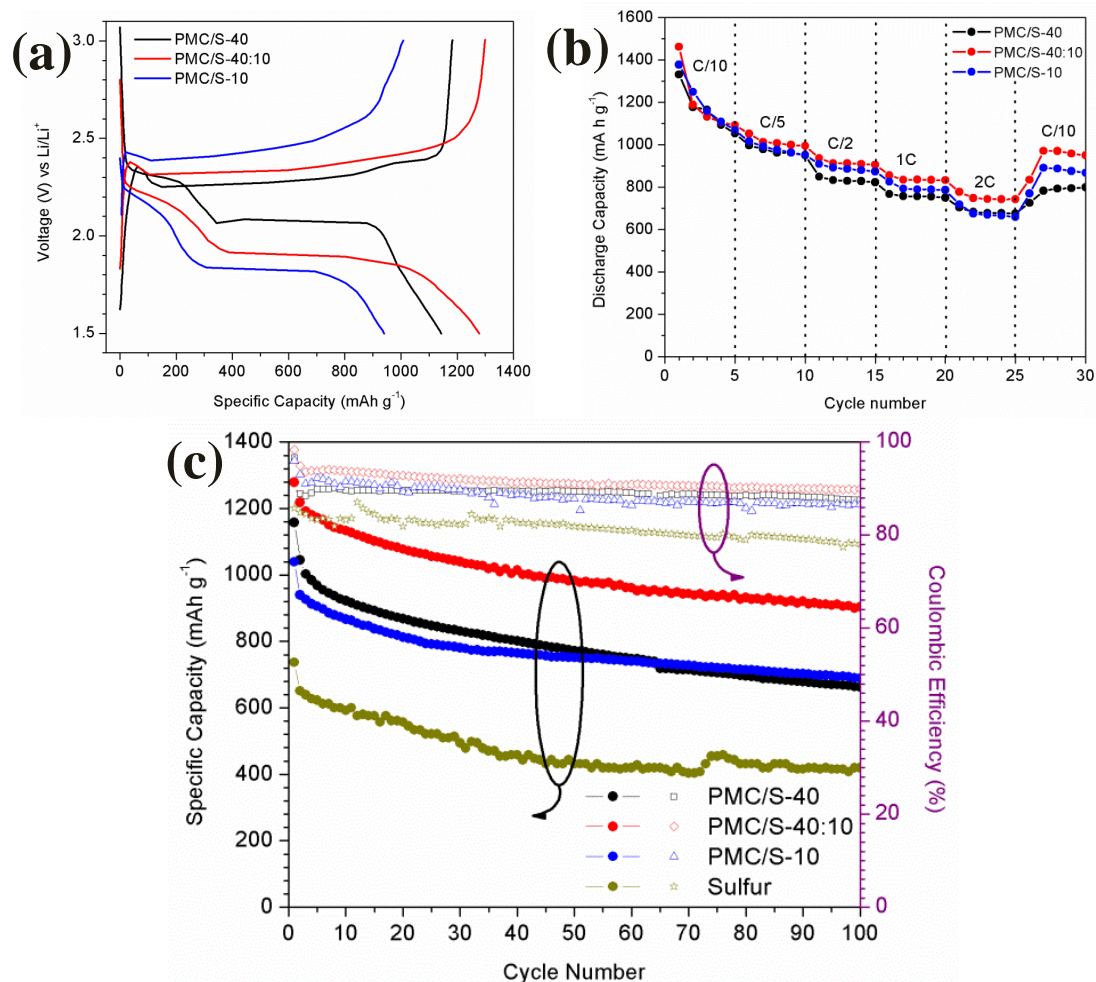
Figure 7.9 Electrochemical characterization and battery performance results of PMC/S: (a) initial cycle charge-discharge profiles between 1.5 V and 3.0 V at a current density of 1 C rate, (b) comparison of the rate capability of PMC/S at current density from C/10 to 2 C, and (c) cycle performance and Coulombic efficiency of PMC/S and pristine sulfur samples over 100 cycles at 1 C rate.

The higher electrochemical performance of PMC/S-40:10 than those of PMC/S-40 and PMC/S-10 can be explained by the differences in their pore structures (see **Table 7.2**); i.e., PMC/S-40:10 has a unique combination of macropores, mesopores, and micropores. First, the macropores (~55 nm) and large mesopores (~40 nm) allow easy electrolyte diffusion and Li$^+$ transport, and in the meantime, accommodate sulfur volume expansion during cycling. Second, the small mesopores (~10 nm) bridge the larger pores (40~55 nm) and provide passages and easy access in between the larger pores, thus lower the resistance

in charge transfer and diffusion. Third, the very small mesopores (4~6 nm) and micropores (< 2 nm) enhance the contact between carbon and sulfur due to their extremely small size, and they help trap polysulfides and prevent active sulfur material from escaping the carbon framework to a certain extent. In short, the hierarchical structure of macropore-mesopore-micropore network with differential pore sizes provide easy access for sulfur infiltration, electrolyte diffusion, and ion transport through larger pores, while the smaller pores surrounding the larger pores to some extent prevent polysulfides from leaving the larger pores so that each microsphere acts as a good sulfur container.

Comparing PMC/S-40 with PMC/S-40:10, the lack of large population of small mesopores in the 10 nm range in PMC/S-40 may have caused difficulty for larger pores (40~55 nm) to "communicate" with each other (e.g., ion transport and electrolyte permeation between the large particles), as the larger pores are segregated by carbon walls that have only micropores. In addition, large size pores (like the 40~55 nm pores in PMC/S-40) cannot effectively trap lithium polysulfides.[17, 180] In another word, PMC/S-40:10 performed better than PMC/S-40 because the large number of 10 nm small mesopores in PMC/S-40:10 may have created easier passages for ion transport in between the 40~55 nm pores and at the same time mitigated the loss of active sulfur by confining polysulfides to some extent.   Comparing PMC/S-10 with PMC/S-40:10, the lack of large pores (40~55 nm) and the presence of only small mesopores (< 10 nm) in PMC/S-10 may have caused infiltrated sulfur to block the small pores, making electrolyte permeation and ion transport more difficult in PMC/S-10.[57, 60, 73] Micropores and small mesopores have advantages in constraining lithium polysulfides to inhibit the "shuttle effect",[57] but too small micropores (<0.7 nm) are not accessible to guest molecules or electrolyte ions.[68, 181] These could

explain that PMC/S-10 with only small pores exhibited lower initial capacity compared with those of PMC/S-40 and PMC/S-40:10 that have a considerable amount of large pores. The results from electrochemical impedance spectroscopy (EIS), as shown in **Fig. 7.10**, also confirm that PMC/S-40:10 has the lowest impedance, with PMC/S-10 having the highest impedance. The EIS results agree with our above analysis that PMC/S-40:10 has a unique hierarchical pore structure that is in favor of charge transport and reducing ohmic resistance.
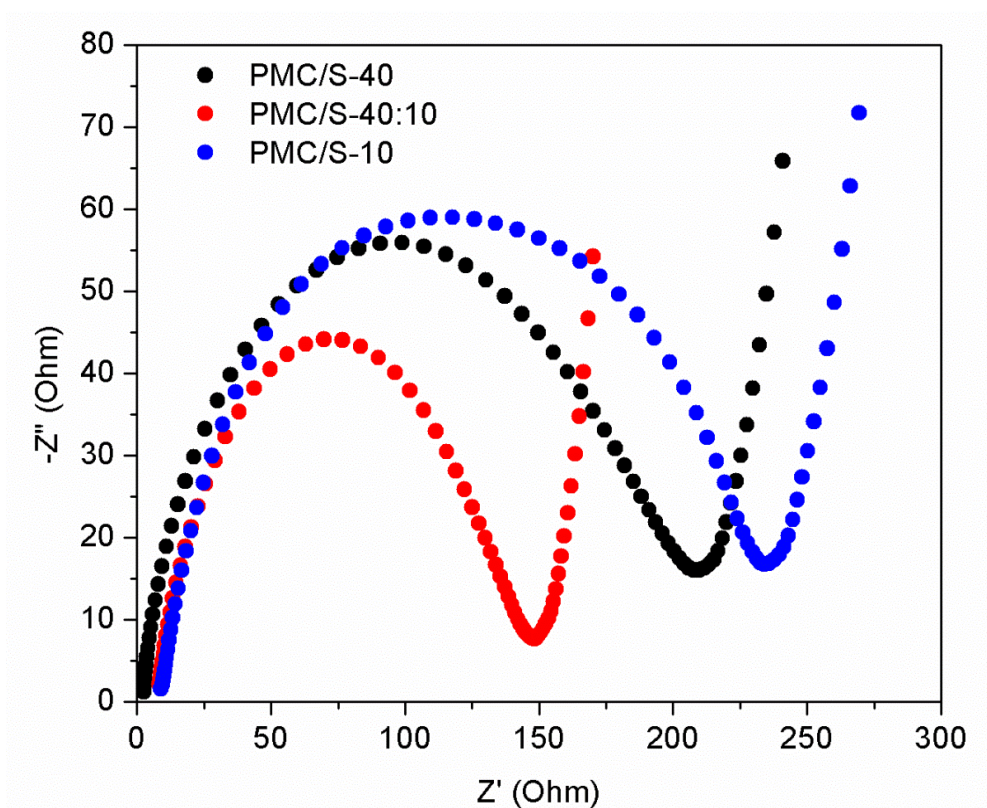
Figure 7.10 Electrochemical impedance spectroscopy (EIS) curves of PMC/S-40, PMC/S-40:10, and PMC-10 before initial discharge.

The electrochemical performance data obtained using our PMC/S-40:10 cathode material (1,278 mAh g^{-1} initial capacity, and 904 mAh g^{-1} after 100 cycles at 1 C rate with stable 90% Coulombic efficiency) are comparable to the results in the leading literature on Li-S battery with sulfur loaded on porous carbon. But our material synthesis method is

relatively simple and our raw materials used are cheaper with promising scale-up potential. Based on our results in this work and the above literature review, we believe the shuttle effect still exists to some extent in our PMC/S materials because of the open porous structure that allows free access of electrolyte to the sulfur. However, the shuttle effect was significantly mitigated compared with the pristine sulfur without the carbon framework. Our work demonstrated that multi-modal porous carbon with relatively wide pore size distributions is also an excellent substrate for Li-S cathodes. Among the three porous PMC/S samples, the one with the mixed pore sizes, PMC/S-40:10, has the highest capacity and Coulombic efficiency (reduced shuttle effect), although its surface area is less than that of PMC/S-10. This is an original finding in this work in terms of a new material design. Magasinski et al.[182] indicated in a Li-ion battery study that an aperiodic porous network would allow for the redirection of the ion traffic if the path of Li ions is blocked or impeded in a narrow channel. Similarly, the hierarchically interconnected porous network with wide PSD warrants our PMC/S-40:10 nanocomposite the similar ability of redirecting the ion traffic to maintain rapid charging capability.

7.4 Summary and Conclusion

In summary, this work proves a novel concept that a sulfur infiltration 3D multi-modal PMC with interconnected micropores, mesopores and macropores can serve as a promising cathode material for Li-S batteries. The developed hierarchical pore structure offers several advantages: (1) interconnected multi-modal porous carbon framework in close contact with sulfur assures superb electrical conductivity (or low impedance), fast ion transport, and excellent electrolyte permeation to active sulfur within the entire framework; (2) large pores facilitate sulfur infiltration and small pores help trap

polysulfides and inhibit sulfur loss to some extent; and (3) sufficient total pore volume to accommodate sulfur volume expansion during cycling. The unique structure of small mesopores (~10 nm) as bridging agents between larger pores (40~55 nm) is indispensible in providing the above three advantages, rendering the PMC/S-40:10 material the best electrochemical performance among the PMC/s samples tested.   We have demonstrated that a discharge capacity of 1,278 mA h g^{-1} was achieved at 1 C current density and the capacity maintained at 904 mA h g^{-1} even after 100 cycles. This electrochemical performance is among the highest ones reported in the open literature. It is possible that further tuning the pore size distribution of PMC/S (by adjusting silica template sizes and their ratios) will lead to higher and more stable cycling performance. In addition, coating a conductive layer on the PMC/S microspheres may further prohibit the shuttle effect and enhance the Coulombic efficiency. The aerosol-based spray pyrolysis synthesis process is simple, inexpensive, and can be easily scaled up, providing promising opportunities to commercialize the PMC materials that could be applied in a variety of electrode materials.

CHAPTER 8   SUMMARY OF RESEARCH WORK AND PROPOSED FUTURE WORK

8.1 Summary of Research Work

1. Nanostructured Ce-TiO$_2$/SBA-15 Composites for CO$_2$ Photoreduction

Ce-TiO$_2$/SBA-15 were synthesized via sol-gel method to help facilitate e-h pairs separation and improve catalysts dispersion.   Modification of TiO$_2$ with Ce significantly stabilized the TiO$_2$ anatase phase and increased the specific surface area, which contributed to an improvement of CO production from CO$_2$ reduction. Dispersing Ce-TiO$_2$ nanoparticles on the mesoporous SBA-15 support further enhanced both CO and CH$_4$ production. We proposed that the superior catalytic activity may be related to the partially embedded Ce–TiO$_2$ nanoparticles in the ordered 1-D pores in SBA-15 that form synergies between the different components of the catalysts and enhance the diffusion and adsorption of CO$_2$. This mechanism also correlates well the results that using SBA-15 as the support led to more than 10 times higher activity in CO$_2$ photoreduction than using amorphous silica as the support. Findings in this work demonstrate the feasibility of solar fuel production from CO$_2$ and H$_2$O using the prepared nanocomposite photocatalysts.

2. Ag/TiO$_2$ Nanocomposite Photocatalysts For Simultaneous H$_2$ Production And CO$_2$ Reduction

Ag/TiO$_2$ were fabricated via ultrasonic spray pyrolysis technique. The material property analysis and photocatalytic activity results showed that the ultrasonic spray pyrolysis method is much superior to conventional wet impregnation process with the advantages of smaller Ag nanoparticles, a better Ag dispersion on TiO$_2$, and a higher fraction of metallic Ag species, which facilitate charge transfer and improve photocatalytic

activity. The rates of photocatalytic conversion in this work were among the highest ones reported in the literature. This work has also demonstrated the feasibility of syngas (H_2 and CO) production from a gas mixture of CO_2, H_2O and CH_3OH through a photocatalytic reduction process on Ag/TiO_2 nanocomposite catalysts under solar irradiation. Although the H_2 production and CO_2 reduction processes compete for electrons and protons in the photocatalytic process, the final product selectivity (H_2/CO ratio as low as 2, with negligible CH_4) is in the appropriate range for subsequent Fischer-Tropsch process for liquid hydrocarbon fuel production. The selectivity is tunable by varying the reaction gas composition and the H_2/CO ratio in the range from 2 to 10 has been achieved.

3. Hybrid MgAl-LDO/TiO$_2$ Composites for CO$_2$ Photoreduction

MgAl-LDO/TiO_2 composites were prepared by a combination of hydrothermal and co-precipitation method. This work has demonstrated that the successful synthesis for novel hybrid structure of MgAl-LDOs platelets grafted on TiO_2 cuboids with high length to width ratio. MgAl-LDOs addition has no impact on the optical propertied of TiO_2. The morphology of TiO_2-MgAl-LDOs showed that the surface coverage on TiO_2 on MgAl-LDOs platelets could be controlled by tuning the MgAl-LDOs to TiO_2 ratio. As the MgAl-LDOs concentration increases, TiO_2 crystal size was increased. MgAl-LDOs grafting on TiO_2 cuboids may help improve the adsorption ability of CO_2 onto TiO_2 which improves the photocatalytic activity of CO_2 reduction. The optimum MgAl-LDOs concentration was found to be 10% which performed the highest CO production rate. The proposed reason for this is: at higher MgAl-LDOs concentration, MgAl-LDOs platelets covered the majority parts of TiO_2 cuboids surface either blocked the CO_2 and H_2O vapor contacting with TiO_2 or electrons transferring from TiO_2 to CO_2 and H_2O molecules; Moreover, the

crystal size increase of TiO2 anatase may also lead to a poor CO2 photoreduction activity. At lower MgAl-LDOs concentration, less CO_2 and H_2O amount may be adsorbed onto the composites which also leads to lower CO production rate.

4. Carbon-TiO₂ Nanocomposites Prepared With Simple Method For Lithium-Ion Batteries (LIBs)

Carbon decorated TiO_2 were synthesized using commercial TiO_2 product (P25 and P90) in large scale through a simple carbonization process. C-P90 possesses higher specific area and larger fraction of anatase comparing to C-P25 with the same carbon concentration, which guaranteed its superior electrochemical performance as anode for LIBs. Carbon concentration had been optimized to obtain the best battery performance for P90. 1.9% C-P90 showed a significant stable cyclablity which was attributed to its unique carbon decoration nanostructure that facilitates efficient lithium insertion and extraction. The easy preparation together with the advantage of stable cyclability of C-P90 makes the composite a very promising anode material for LIBs.

5. Hierarchical Sulfur-infiltrated porous microsphere carbon as cathode for Li-S batteries

PMC materials were synthesized via aerosol method. The aerosol-based spray pyrolysis synthesis process is simple, inexpensive, and can be easily scaled up, providing promising opportunities to commercialize the PMC materials that could be applied in a variety of electrode materials. This work proves a novel concept that a sulfur infiltration 3D multi-modal PMC with interconnected micropores, mesopores and macropores can serve as a promising cathode material for Li–S batteries. The developed hierarchical pore structure offers several advantages: (1) an interconnected multi-modal porous carbon framework in close contact with sulfur assures superb electrical conductivity (or low

impedance), fast ion transport, and excellent electrolyte permeation to active sulfur within the entire framework; (2) large pores facilitate sulfur infiltration and small pores help trap polysulfides and inhibit sulfur loss to some extent; and (3) sufficient total pore volume to accommodate sulfur volume expansion during cycling. The unique structure of small mesopores (~10 nm) as bridging agents between larger pores (40–55 nm) is indispensable in providing the above three advantages, giving the PMC/S-40:10 material the best electrochemical performance among the PMC/S samples tested. It is possible that further tuning the pore size distribution of PMC/S (by adjusting silica template sizes and their ratios) will lead to a higher and more stable cycling performance. In addition, coating a conductive layer on the PMC/S microspheres may further prohibit the shuttle effect and enhance the Coulombic efficiency.

8.2 Proposed Future Work

1. PMC/S Composites for Li-S Batteries

As demonstrated in Chapter 4, PMC/S with multi-modal pore size distribution materials have been synthesized using aerosol technique for Li-S battery. The further work will be carried out to improving the electrochemical performance of Li-S battery.

In 2009, Nazar and co-workers reported a pioneering work in the Li-S cathode material by incorporating sulfur into a highly ordered mesoporous carbon (CMK-3) and coating sulfur-CMK-3 with polyethylene glycol (PEG).[15] Those materials exhibited good stability over 20 cycles tested and had high initial discharge capacities at 1,320 mA h g^{-1} and 1,005 mA h g^{-1} at 0.1 C rate (1 C = 1,675 mA/g) with and without PEG modification, respectively. Nazar's work inspired the investigation of many carbon materials as sulfur substrates such as porous carbon frameworks,[29, 56-60] carbon nanotubes,[34, 61-62] hollow carbon nanofibers,[16] graphene,[63-64] and conductive polymers.[15, 65-66] Cui et al.[65] reported a poly (3,4-ethylenedioxythiophene):poly (styrene sulfonate) (PEDOT:PSS) coated CMK-3/sulfur that could achieve 96-98% Coulombic efficiency. Following this direction, PMC/S materials can be further modified such as coating with conductive polymer to confine sulfur more efficiently.

Wang et al. [34] reported a sulfur-impregnated disordered carbon nanotubes cathode for lithium-sulfur batteries. They prepared this materials at 300-500 ˚C and they proposed that carbon and sulfur could obtain bonding function to avoid sulfur loss during charge-discharge process. Following this direction, we can also improve our PMC/S preparation procedure to obtain "bonded" carbon-sulfur materials.

The proposed future work for Li-S battery project is summarized as follows:

- To find a better way to modify the PMC/S materials.

- The resulting nanomaterials will be characterized using various techniques, such as scanning electron microscopy (SEM), transmission electron microscopy (TEM), high-resolution TEM (HRTEM), X-ray diffraction (XRD), and thermogravimetric analysis (TGA). And the nanomaterials will be used as cathode materials for lithium-sulfur batteries.

- Electrodes and half-coin cell will be prepared and their performance will be investigated.

- The performance of PMC/S nanomaterials as cathode will be optimized.

REFERENCES

1. EPA Overview of Greenhouse Gases. http://www.epa.gov/climatechange/ghgemissions/usinventoryreport.html.

2. Aurian-Blajeni, B.; Halmann, M.; Manassen, J., Photoreduction of carbon dioxide and water into formaldehyde and methanol on semiconductor materials. *Solar Energy* **1980,** *25* (2), 165-170.

3. Kohno, Y.; Tanaka, T.; Funabiki, T.; Yoshida, S., Photoreduction of CO_2 with H_2 over ZrO_2. A study on interaction of hydrogen with photoexcited CO_2. *Physical Chemistry Chemical Physics* **2000,** *2* (11), 2635-2639.

4. Tsuneoka, H.; Teramura, K.; Shishido, T.; Tanaka, T., Adsorbed Species of CO_2 and H_2 on Ga_2O_3 for the Photocatalytic Reduction of CO_2. *Journal of Physical Chemistry C* **2010,** *114* (19), 8892-8898.

5. Li, Y.; Wang, W. N.; Zhan, Z. L.; Woo, M. H.; Wu, C. Y.; Biswas, P., Photocatalytic reduction of CO_2 with H_2O on mesoporous silica supported Cu/TiO_2 catalysts. *Applied Catalysis B-Environmental* **2010,** *100* (1-2), 386-392.

6. Varghese, O. K.; Paulose, M.; LaTempa, T. J.; Grimes, C. A., High-Rate Solar Photocatalytic Conversion of CO_2 and Water Vapor to Hydrocarbon Fuels. *Nano Letters* **2009,** *9* (2), 731-737.

7. Yang, H. M.; Zhang, K.; Shi, R. R.; Tang, A. D., Sol-gel synthesis and photocatalytic activity of CeO2/TiO2 nanocomposites. *Journal of the American Ceramic Society* **2007,** *90* (5), 1370-1374.

8. Wen, C.; Deng, H.; Tian, J. Y.; Zhang, J. M., Photocatalytic activity enhancing for TiO2 photocatalyst by doping with La. *Transactions of Nonferrous Metals Society of China* **2006,** *16*, S728-S731.

9. Yuan, C. S.; Lo, C. C.; Hung, C. H.; Wu, J. F., Photoreduction of carbon dioxide with H_2 and H_2O over TiO_2 and ZrO_2 in a circulated photocatalytic reactor. *Solar Energy Materials and Solar Cells* **2007,** *91* (19), 1765-1774.

10. Jiang, D.; Zhang, S. C.; Tang, T.; Li, J. H.; Xu, Y.; Shen, W. L.; Xu, J.; Deng, F., TiO_2/SBA-15 photocatalysts synthesized through the surface acidolysis of $Ti(O_nBu)_4$ on carboxyl-modified SBA-15. *Catalysis Today* **2010,** *158* (3-4), 329-335.

11. Zhang, Q. Y.; Li, Y.; Ackerman, E. A.; Gajdardziska-Josifovska, M.; Li, H. L., Visible light responsive iodine-doped TiO_2 for photocatalytic reduction of CO_2 to fuels. *Applied Catalysis a-General* **2011,** *400* (1-2), 195-202.

12. Tseng, I. H.; Wu, J. C. S.; Chou, H. Y., Effects of sol-gel procedures on the photocatalysis of Cu/TiO_2 in CO_2 photoreduction. *Journal of Catalysis* **2004,** *221* (2), 432-440.

13. Green, M. A., *Third Generation Photovoltaics: Advanced Solar Energy Conversion* Springer: Berlin Germany, 2004.

14. Barnham, K. W. J.; Mazzer, M.; Clive, B., Resolving the energy crisis: nuclear or photovoltaics? *Nature Materials* **2006,** *5* (3), 161-164.

15. Ji, X. L.; Lee, K. T.; Nazar, L. F., A highly ordered nanostructured carbon-sulphur cathode for lithium-sulphur batteries. *Nature Materials* **2009,** *8* (6), 500-506.

16. Zheng, G. Y.; Yang, Y.; Cha, J. J.; Hong, S. S.; Cui, Y., Hollow Carbon Nanofiber-Encapsulated Sulfur Cathodes for High Specific Capacity Rechargeable Lithium Batteries. *Nano Letters* **2011,** *11* (10), 4462-4467.

17. Ji, X. L.; Nazar, L. F., Advances in Li-S batteries. *Journal of Material Chemistry* **2010,** *20* (44), 9821-9826.

18. Marom, R.; Amalraj, S. F.; Leifer, N.; Jacob, D.; Aurbach, D., A review of advanced and practical lithium battery materials. *Journal of Material Chemistry* **2011,** *21* (27), 9938-9954.

19. Xin, S.; Gu, L.; Zhao, N. H.; Yin, Y. X.; Zhou, L. J.; Guo, Y. G.; Wan, L. J., Smaller Sulfur Molecules Promise Better Lithium-Sulfur Batteries. *Journal of the American Ceramic Society* **2012,** *134* (45), 18510-18513.

20. Manthiram, A.; Fu, Y. Z.; Su, Y. S., Challenges and Prospects of Lithium-Sulfur Batteries. *Acc. Chem. Res.* **2012**.

21. Xiao, L. F.; Cao, Y. L.; Xiao, J.; Schwenzer, B.; Engelhard, M. H.; Saraf, L. V.; Nie, Z. M.; Exarhos, G. J.; Liu, J., A Soft Approach to Encapsulate Sulfur: Polyaniline Nanotubes for Lithium-Sulfur Batteries with Long Cycle Life. *Advanced Materials* **2012,** *24* (9), 1176-1181.

22. Elazari, R.; Salitra, G.; Garsuch, A.; Panchenko, A.; Aurbach, D., Sulfur-Impregnated Activated Carbon Fiber Cloth as a Binder-Free Cathode for Rechargeable Li-S Batteries. *Advanced Materials* **2012,** *23* (47), 5641-5644.

23. Combs, S. Transportation. http://www.window.state.tx.us/specialrpt/energy/uses/transportation.php.

24. C2ES Natural Gas Use in The Transportation Sector. http://www.c2es.org/publications/natural-gas-use-transportation-sector.

25. TSPORT New all-solid sulfur-based battery outperforms lithium-ion technology. http://www.electric-vehiclenews.com/2013/07/new-all-solid-sulfur-based-battery.html.

26. Kudo, A.; Miseki, Y., Heterogeneous photocatalyst materials for water splitting. *Chemical Society Reviews* **2009,** *38* (1), 253-278.

27. Zou, Z. G.; Ye, J. H.; Sayama, K.; Arakawa, H., Direct splitting of water under visible light irradiation with an oxide semiconductor photocatalyst. *Nature* **2001,** *414* (6864), 625-627.

28. Ni, M.; Leung, M. K. H.; Leung, D. Y. C.; Sumathy, K., A review and recent developments in photocatalytic water-splitting using TiO_2 for hydrogen production. *Renewable & Sustainable Energy Reviews* **2007,** *11* (3), 401-425.

29. Liang, C. D.; Dudney, N. J.; Howe, J. Y., Hierarchically Structured Sulfur/Carbon Nanocomposite Material for High-Energy Lithium Battery. *Chem. Mater.* **2009,** *21* (19), 4724-4730.

30. Su, W. Y.; Zhang, Y. F.; Li, Z. H.; Wu, L.; Wang, X. X.; Li, J. Q.; Fu, X. Z., Multivalency iodine doped TiO_2: Preparation, characterization, theoretical studies, and visible-light photocatalysis. *Langmuir* **2008,** *24* (7), 3422-3428.

31. Evers, S.; Nazar, L. F., New Approaches for High Energy Density Lithium-Sulfur Battery Cathodes. *Acc. Chem. Res.* **2012**.

32. Bruce, P. G.; Freunberger, S. A.; Hardwick, L. J.; Tarascon, J. M., Li-O_2 and Li-S batteries with high energy storage. *Nature Materials* **2012,** *11* (1), 19-29.

33. Zheng, G. Y.; Yang, Y.; Cha, J. J.; Hong, S. S.; Cui, Y., Hollow Carbon Nanofiber-Encapsulated Sulfur Cathodes for High Specific Capacity Rechargeable Lithium Batteries. *Nano Letters* **2011,** *11* (10), 4462-4467.

34. Guo, J. C.; Xu, Y. H.; Wang, C. S., Sulfur-Impregnated Disordered Carbon Nanotubes Cathode for Lithium-Sulfur Batteries. *Nano Letters* **2011,** *11* (10), 4288-4294.

35. Xu, Y. H.; Zeng, Z. X., The preparation, characterization, and photocatalytic activities of Ce-TiO$_2$/SiO$_2$. *Journal of Molecular Catalysis a-Chemical* **2008,** *279* (1), 77-81.

36. Reddy, B. M.; Khan, A.; Lakshmanan, P.; Aouine, M.; Loridant, S.; Volta, J. C., Structural characterization of nanosized CeO$_2$-SiO$_2$, CeO$_2$-TiO$_2$, and CeO$_2$-ZrO$_2$ catalysts by XRD, raman, and HREM techniques. *Journal of Physical Chemistry B* **2005,** *109* (8), 3355-3363.

37. Ogura, K.; Kawano, M.; Yano, J.; Sakata, Y., Visible-Light-Assisted Decomposition of H$_2$O and Photomethanation of CO$_2$ over CeO$_2$-TiO$_2$ Catalyst. *Journal of Photochemistry and Photobiology a-Chemistry* **1992,** *66* (1), 91-97.

38. Xie, J. M.; Jiang, D. L.; Chen, M.; Li, D.; Zhu, J. J.; Lu, X. M.; Yan, C. H., Preparation and characterization of monodisperse Ce-doped TiO$_2$ microspheres with visible light photocatalytic activity. *Colloids and Surfaces a-Physicochemical and Engineering Aspects* **2010,** *372* (1-3), 107-114.

39. Li, G. S.; Zhang, D. Q.; Yu, J. C., Thermally stable ordered mesoporous CeO$_2$/TiO$_2$ visible-light photocatalysts. *Physical Chemistry Chemical Physics* **2009,** *11* (19), 3775-3782.

40. Sun, X. J.; Liu, H.; Dong, J. H.; Wei, J. Z.; Zhang, Y., Preparation and Characterization of Ce/N-Codoped TiO$_2$ Particles for Production of H$_2$ by Photocatalytic Splitting Water Under Visible Light. *Catalysis Letters* **2010,** *135* (3-4), 219-225.

41. Magesh, G.; Viswanathan, B.; Viswanath, R. P.; Varadarajan, T. K., Photocatalytic behavior of CeO$_2$-TiO$_2$ system for the degradation of methylene blue. *Indian Journal of Chemistry Section a-Inorganic Bio-Inorganic Physical Theoretical & Analytical Chemistry* **2009,** *48* (4), 480-488.

42. Sasirekha, N.; Basha, S. J. S.; Shanthi, K., Photocatalytic performance of Ru doped anatase mounted on silica for reduction of carbon dioxide. *Applied Catalysis B-Environmental* **2006,** *62* (1-2), 169-180.

43. Srinivas, B.; Shubhamangala, B.; Lalitha, K.; Reddy, P. A. K.; Kumari, V. D.; Subrahmanyam, M.; De, B. R., Photocatalytic Reduction of CO$_2$ over Cu-TiO(2)/Molecular Sieve 5A Composite. *Photochemistry and Photobiology* **2011,** *87* (5), 995-1001.

44. Zhang, S. C.; Jiang, D.; Tang, T.; Li, J. H.; Xu, Y.; Shen, W. L.; Xu, J.; Deng, F., TiO$_2$/SBA-15 photocatalysts synthesized through the surface acidolysis of Ti(O$_n$Bu)$_4$ on carboxyl-modified SBA-15. *Catalysis Today* **2010,** *158* (3-4), 329-335.

45. Wu, J. C. S., Photocatalytic Reduction of Greenhouse Gas CO$_2$ to Fuel. *Catalysis Surveys from Asia* **2009,** *13* (1), 30-40.

46. Yang, C. C.; Vernimmen, J.; Meynen, V.; Cool, P.; Mul, G., Mechanistic study of hydrocarbon formation in photocatalytic CO$_2$ reduction over Ti-SBA-15. *Journal of Catalysis* **2011,** *284* (1), 1-8.

47. Yang, H. C.; Lin, H. Y.; Chien, Y. S.; Wu, J. C. S.; Wu, H. H., Mesoporous TiO$_2$/SBA-15, and Cu/TiO$_2$/SBA-15 Composite Photocatalysts for Photoreduction of CO$_2$ to Methanol. *Catalysis Letters* **2009,** *131* (3-4), 381-387.

48. Koci, K.; Mateju, K.; Obalova, L.; Krejcikova, S.; Lacny, Z.; Placha, D.; Capek, L.; Hospodkova, A.; Solcova, O., Effect of silver doping on the TiO$_2$ for photocatalytic reduction of CO$_2$. *Applied Catalysis B-Environmental* **2010,** *96* (3-4), 239-244.

49. Sasirekha, N.; Basha, S. J. S.; Shanthi, K., Photocatalytic performance of Ru doped anatase mounted on silica for reduction of carbon dioxide. *Applied Catalysis B:*

Environmental **2006,** *62* (1-2), 169-180.

50. Subrahmanyam, M.; Kaneco, S.; Alonso-Vante, N., A screening for the photo reduction of carbon dioxide supported on metal oxide catalysts for C1-C3 selectivity. *Applied Catalysis B: Environmental* **1999,** *23* (2-3), 169-174.

51. Mizuno, T.; Adachi, K.; Ohta, K.; Saji, A., Effect of CO_2 pressure on photocatalytic reduction of CO_2 using TiO_2 in aqueous solutions. *Journal of Photochemistry and Photobiology A: Chemistry* **1996,** *98* (1-2), 87-90.

52. Zhang, Q.; Gao, T.; Andino, J. M.; Li, Y., Copper and iodine co-modified TiO_2 nanoparticles for improved activity of CO_2 photoreduction with water vapor. *Applied Catalysis B: Environmental* **2012,** *123-124* (0), 257-264.

53. Park, M. S.; Kang, M., The preparation of the anatase and rutile forms of Ag-TiO_2 and hydrogen production from methanol/water decomposition. *Materials Letters* **2008,** *62* (2), 183-187.

54. Yu, J.; Qi, L.; Jaroniec, M., Hydrogen Production by Photocatalytic Water Splitting over Pt/TiO_2 Nanosheets with Exposed (001) Facets. *The Journal of Physical Chemistry C* **2010,** *114* (30), 13118-13125.

55. Park, J. W.; Kang, M., Synthesis and characterization of AgxO, and hydrogen production from methanol photodecomposition over the mixture of AgxO and TiO_2. *International Journal of Hydrogen Energy* **2007,** *32* (18), 4840-4846.

56. Lai, C.; Gao, X. P.; Zhang, B.; Yan, T. Y.; Zhou, Z., Synthesis and Electrochemical Performance of Sulfur/Highly Porous Carbon Composites. *J. Phys. Chem. C* **2009,** *113* (11), 4712-4716.

57. Schuster, J.; He, G.; Mandlmeier, B.; Yim, T.; Lee, K. T.; Bein, T.; Nazar, L. F., Spherical Ordered Mesoporous Carbon Nanoparticles with High Porosity for Lithium-Sulfur Batteries. *Angew. Chem. Int. Edn.* **2012,** *51* (15), 3591-3595.

58. Kim, T. W.; Park, I. S.; Ryoo, R., A synthetic route to ordered mesoporous carbon materials with graphitic pore walls. *Angew. Chem. Int. Edn.* **2003,** *42* (36), 4375-4379.

59. He, G.; Ji, X. L.; Nazar, L. F., High "C" rate Li-S cathodes: sulfur imbibed bimodal porous carbons. *Energy Environ. Sci.* **2011,** *4* (8), 2878-2883.

60. Jayaprakash, N.; Shen, J.; Moganty, S. S.; Corona, A.; Archer, L. A., Porous Hollow Carbon@Sulfur Composites for High-Power Lithium-Sulfur Batteries. *Angew. Chem. Int. Edn.* **2011,** *50* (26), 5904-5908.

61. Zhou, G. M.; Wang, D. W.; Li, F.; Hou, P. X.; Yin, L. C.; Liu, C.; Lu, G. Q.; Gentle, I. R.; Cheng, H. M., A flexible nanostructured sulphur-carbon nanotube cathode with high rate performance for Li-S batteries. *Energy Environ. Sci.* **2012,** *5* (10), 8901-8906.

62. Chen, J. J.; Zhang, Q. F.; Shi, Y. N.; Qin, L. L.; Cao, Y. L.; Zheng, M. S.; Dong, Q. F., A hierarchical architecture S/MWCNT nanomicrosphere with large pores for lithium sulfur batteries. *Phys. Chem. Chem. Phys.* **2012,** *14* (16), 5376-5382.

63. Park, M. S.; Yu, J. S.; Kim, K. J.; Jeong, G.; Kim, J. H.; Jo, Y. N.; Hwang, U.; Kang, S.; Woo, T.; Kim, Y. J., One-step synthesis of a sulfur-impregnated graphene cathode for lithium-sulfur batteries. *Phys. Chem. Chem. Phys.* **2012,** *14* (19), 6796-6804.

64. Wang, H. L.; Yang, Y.; Liang, Y. G.; Robinson, J. T.; Li, Y. G.; Jackson, A.; Cui, Y.; Dai, H. J., Graphene-Wrapped Sulfur Particles as a Rechargeable Lithium-Sulfur Battery Cathode Material with High Capacity and Cycling Stability. *Nano Letters.* **2011,** *11* (7), 2644-2647.

65. Yang, Y.; Yu, G. H.; Cha, J. J.; Wu, H.; Vosgueritchian, M.; Yao, Y.; Bao, Z. A.; Cui,

Y., Improving the Performance of Lithium-Sulfur Batteries by Conductive Polymer Coating. *ACS Nano* **2011,** *5* (11), 9187-9193.

66. Zheng, G. Y.; Zhang, Q. F.; Cha, J. J.; Yang, Y.; Li, W. Y.; Seh, Z. W.; Cui, Y., Amphiphilic Surface Modification of Hollow Carbon Nanofibers for Improved Cycle Life of Lithium Sulfur Batteries. *Nano Letters.* **2013,** *13* (3), 1265-1270.

67. Jiang, H.; Lee, P. S.; Li, C. Z., 3D carbon based nanostructures for advanced supercapacitors. *Energy Environment&Science.* **2013,** *6* (1), 41-53.

68. Zhang, L.; Zhang, F.; Yang, X.; Long, G. K.; Wu, Y. P.; Zhang, T. F.; Leng, K.; Huang, Y.; Ma, Y. F.; Yu, A.; Chen, Y. S., Porous 3D graphene-based bulk materials with exceptional high surface area and excellent conductivity for supercapacitors. *Scientific Report.* **2013,** *3*, 1-9.

69. Tiwari, J. N.; Tiwari, R. N.; Kim, K. S., Zero-dimensional, one-dimensional, two-dimensional and three-dimensional nanostructured materials for advanced electrochemical energy devices. *Prog. Mater Sci.* **2012,** *57* (4), 724-803.

70. Xin, X.; Zhou, X. F.; Wang, F.; Yao, X. Y.; Xu, X. X.; Zhu, Y. M.; Liu, Z. P., A 3D porous architecture of Si/graphene nanocomposite as high-performance anode materials for Li-ion batteries. *Journal of Material Chemistry.* **2012,** *22* (16), 7724-7730.

71. Xu, G. Y.; Ding, B.; Shen, L. F.; Nie, P.; Han, J. P.; Zhang, X. G., Sulfur embedded in metal organic framework-derived hierarchically porous carbon nanoplates for high performance lithium-sulfur battery. *Journal of Material Chemistry A* **2013,** *1* (14), 4490-4496.

72. Wei, S. C.; Zhang, H.; Huang, Y. Q.; Wang, W. K.; Xia, Y. Z.; Yu, Z. B., Pig bone derived hierarchical porous carbon and its enhanced cycling performance of lithium-sulfur batteries. *Energy Environment&Science.* **2011,** *4* (3), 736-740.

73. Zhang, K.; Zhao, Q.; Tao, Z. L.; Chen, J., Composite of sulfur impregnated in porous hollow carbon spheres as the cathode of Li-S batteries with high performance. *Nano Research.* **2013,** *6* (1), 38-46.

74. Zhao, S. R.; Li, C. M.; Wang, W. K.; Zhang, H.; Gao, M. Y.; Xiong, X.; Wang, A. B.; Yuan, K. G.; Huang, Y. Q.; Wang, F., A novel porous nanocomposite of sulfur/carbon obtained from fish scales for lithium-sulfur batteries. *Journal of Material Chemistry A* **2013,** *1* (10), 3334-3339.

75. Jing, L. Q.; Sun, X. J.; Xin, B. F.; Wang, B. Q.; Cai, W. M.; Fu, H. G., The preparation and characterization of La doped TiO_2 nanoparticles and their photocatalytic activity. *Journal of Solid State Chemistry* **2004,** *177* (10), 3375-3382.

76. Zhao, D. Y.; Feng, J. L.; Huo, Q. S.; Melosh, N.; Fredrickson, G. H.; Chmelka, B. F.; Stucky, G. D., Triblock copolymer syntheses of mesoporous silica with periodic 50 to 300 angstrom pores. *Science* **1998,** *279* (5350), 548-552.

77. Fang, J.; Bi, X. Z.; Si, D. J.; Jiang, Z. Q.; Huang, W. X., Spectroscopic studies of interfacial structures of CeO_2-TiO_2 mixed oxides. *Applied Surface Science* **2007,** *253* (22), 8952-8961.

78. Kidchob, T.; Malfatti, L.; Marongiu, D.; Enzo, S.; Innocenzi, P., An alternative sol-gel route for the preparation of thin films in CeO_2-TiO_2 binary system. *Thin Solid Films* **2010,** *518* (6), 1653-1657.

79. Liu, Z. L.; Guo, B.; Hong, L.; Jiang, H. X., Preparation and characterization of cerium oxide doped TiO_2 nanoparticles. *Journal of Physics and Chemistry of Solids* **2005,** *66* (1), 161-167.

80. Nie, X. L.; Zhuo, S. P.; Maeng, G.; Sohlberg, K., Doping of TiO_2 Polymorphs for Altered Optical and Photocatalytic Properties. *International Journal of Photoenergy* **2009**, -.

81. Wu, Z. B.; Dong, F.; Zhao, W. R.; Guo, S., Visible light induced electron transfer process over nitrogen doped TiO_2 nanocrystals prepared by oxidation of titanium nitride. *Journal of Hazardous Materials* **2008**, *157* (1), 57-63.

82. Sahu, D. R.; Hong, L. Y.; Wang, S. C.; Huang, J. L., Synthesis, analysis and characterization of ordered mesoporous TiO_2/SBA-15 matrix: Effect of calcination temperature. *Microporous Mesoporous Mat.* **2009**, *117* (3), 640-649.

83. Yang, J.; Zhang, J.; Zhu, L. W.; Chen, S. Y.; Zhang, Y. M.; Tang, Y.; Zhu, Y. L.; Li, Y. W., Synthesis of nano titania particles embedded in mesoporous SBA-15: Characterization and photocatalytic activity. *Journal of Hazardous Materials.* **2006**, *137* (2), 952-958.

84. Zhu, H. G.; Pan, Z. W.; Chen, B.; Lee, B.; Mahurin, S. M.; Overbury, S. H.; Dai, S., Synthesis of ordered mixed titania and silica mesostructured monoliths for gold catalysts. *Journal of Physics Chemistry B* **2004**, *108* (52), 20038-20044.

85. Henglein, A., Small-Particle Research - Physicochemical properties of extremely small colloidal metal and semiconductor particles. *Chemistry Review.* **1989**, *89* (8), 1861-1873.

86. Holgado, J. P.; Alvarez, R.; Munuera, G., Study of CeO2 XPS spectra by factor analysis: reduction of CeO_2. *Applied Surface Science* **2000**, *161* (3-4), 301-315.

87. Zhang, Q.; Li, Y.; Ackerman, E. A.; Gajdardziska-Josifovska, M.; Li, H., Visible light responsive iodine-doped TiO_2 for photocatalytic reduction of CO_2 to fuels. *Applied Catalysis A: General* **2011**, *400* (1-2), 195-202.

88. Liu, L.; Zhao, C.; Li, Y., Spontaneous Dissociation of CO_2 to CO on Defective Surface of Cu(I)/TiO_{2-x} Nanoparticles at Room Temperature. *Journal of Physical Chemistry C* **2012**, *116* (14), 7904-7912.

89. Tseng, I. H.; Chang, W.-C.; Wu, J. C. S., Photoreduction of CO_2 using sol-gel derived titania and titania-supported copper catalysts. *Applied Catalysis B: Environmental* **2002**, *37* (1), 37-48.

90. Wang, W.-N.; An, W.-J.; Ramalingam, B.; Mukherjee, S.; Niedzwiedzki, D. M.; Gangopadhyay, S.; Biswas, P., Size and Structure Matter: Enhanced CO_2 Photoreduction Efficiency by Size-Resolved Ultrafine Pt Nanoparticles on TiO_2 Single Crystals. *Journal of the American Chemical Society* **2012**, *134* (27), 11276-11281.

91. Galindo, F.; Gomez, R.; Aguilar, M., Photodegradation of the herbicide 2,4-dichlorophenoxyacetic acid on nanocrystalline TiO_2-CeO_2 sol-gel catalysts. *Journal of Molecular Catalysis a-Chemical* **2008**, *281* (1-2), 119-125.

92. Yang, J.; Zhu, L. W.; Zhang, J.; Zhang, Y. M.; Tang, Y., Synthesis of nanosized TiO2/SiO2 catalysts by the ultrasonic microemulsion method and their photocatalytic activity. *Reaction Kinetics and Catalysis Letters* **2007**, *91* (1), 21-28.

93. Choi, S.; Drese, J. H.; Jones, C. W., Adsorbent Materials for Carbon Dioxide Capture from Large Anthropogenic Point Sources. *ChemSusChem* **2009**, *2* (9), 796-854.

94. Zhao, B.; Chen, Y.-W., Ag/TiO_2 sol prepared by a sol-gel method and its photocatalytic activity. *Journal of Physics and Chemistry of Solids* **2011**, *72* (11), 1312-1318.

95. Lalitha, K.; Reddy, J. K.; Phanikrishna Sharma, M. V.; Kumari, V. D.; Subrahmanyam, M., Continuous hydrogen production activity over finely dispersed Ag_2O/TiO_2 catalysts from methanol:water mixtures under solar irradiation: A structure-activity correlation.

International Journal of Hydrogen Energy **2010,** *35* (9), 3991-4001.

96. Gurav, A.; Kodas, T.; Pluym, T.; Xiong, Y., Aerosol Processing of Materials. *Aerosol Science and Technology* **1993,** *19* (4), 411-452.

97. Messing, G. L.; Zhang, S. C.; Jayanthi, G. V., Ceramic Powder Synthesis by Spray-Pyrolysis. *Journal of the American Ceramic Society* **1993,** *76* (11), 2707-2726.

98. Tsai, S. C.; Song, Y. L.; Tsai, C. S.; Yang, C. C.; Chiu, W. Y.; Lin, H. M., Ultrasonic spray pyrolysis for nanoparticles synthesis. *Journal of Materials Science* **2004,** *39* (11), 3647-3657.

99. Onsuratoom, S.; Puangpetch, T.; Chavadej, S., Comparative investigation of hydrogen production over Ag-, Ni-, and Cu-loaded mesoporous-assembled TiO_2-ZrO_2 mixed oxide nanocrystal photocatalysts. *Chemical Engineering Journal* **2011,** *173* (2), 667-675.

100. Alenzi, N.; Liao, W. S.; Cremer, P. S.; Sanchez-Torres, V.; Wood, T. K.; Ehlig-Economides, C.; Cheng, Z. D., Photoelectrochemical hydrogen production from water/methanol decomposition using Ag/TiO_2 nanocomposite thin films. *International Journal of Hydrogen Energy* **2010,** *35* (21), 11768-11775.

101. Weast, R. C., CRC handbook of chemistry and physics 67th ed. CRC Press, Inc. *Biochemical Education* **1986**.

102. Lee, J. H.; Jung, K. Y.; Park, S. B., Modification of titania particles by ultrasonic spray pyrolysis of colloid. *Journal of Materials Science* **1999,** *34* (16), 4089-4093.

103. Georgekutty, R.; Seery, M. K.; Pillai, S. C., A highly efficient Ag-ZnO photocatalyst: Synthesis, properties, and mechanism. *Journal of Physical Chemistry C* **2008,** *112* (35), 13563-13570.

104. Seery, M. K.; George, R.; Floris, P.; Pillai, S. C., Silver doped titanium dioxide nanomaterials for enhanced visible light photocatalysis. *Journal of Photochemistry and Photobiology A: Chemistry* **2007,** *189* (2-3), 258-263.

105. Haugen, A. B.; Kumakiri, I.; Simon, C.; Einarsrud, M.-A., TiO_2, TiO_2/Ag and TiO_2/Au photocatalysts prepared by spray pyrolysis. *Journal of the European Ceramic Society* **2011,** *31* (3), 291-298.

106. Sobana, N.; Muruganadham, M.; Swaminathan, M., Nano-Ag particles doped TiO2 for efficient photodegradation of Direct azo dyes. *Journal of Molecular Catalysis a-Chemical* **2006,** *258* (1-2), 124-132.

107. Sobana, N.; Selvam, K.; Swaminathan, M., Optimization of photocatalytic degradation conditions of Direct Red 23 using nano-Ag doped TiO_2. *Separation and Purification Technology* **2008,** *62* (3), 648-653.

108. Du, J. M.; Zhang, J. L.; Liu, Z. M.; Han, B. X.; Jiang, T.; Huang, Y., Controlled synthesis of Ag/TiO_2 core-shell nanowires with smooth and bristled surfaces via a one-step solution route. *Langmuir* **2006,** *22* (3), 1307-1312.

109. Zhao, C. Y.; Kroll, A.; Zhao, H. L.; Zhang, Q. Y.; Li, Y., Ultrasonic spray pyrolysis synthesis of Ag/TiO_2 nanocomposite photocatalysts for simultaneous H_2 production and CO_2 reduction. *International Journal of Hydrogen Energy* **2012,** *37* (13), 9967-9976.

110. Liu, L. J.; Pitts, D. T.; Zhao, H. L.; Zhao, C. Y.; Li, Y., Silver-incorporated bicrystalline (anatase/brookite) TiO_2 microspheres for CO_2 photoreduction with water in the presence of methanol. *Applied Catalysis a-General* **2013,** *467*, 474-482.

111. Zhao, C.; Liu, L.; Zhang, Q.; Wang, J.; Li, Y., Photocatalytic Conversion of CO_2 and H_2O to Fuels by Nanostructured $Ce-TiO_2/SBA-15$ Composites. *Catalysis Science & Technology* **2012**.

112. Zhao, H. L.; Liu, L. J.; Andino, J. M.; Li, Y., Bicrystalline TiO_2 with controllable anatase-brookite phase content for enhanced CO_2 photoreduction to fuels. *Journal of Materials Chemistry A* **2013,** *1* (28), 8209-8216.

113. Zhao, C. Y.; Krall, A.; Zhao, H. L.; Zhang, Q. Y.; Li, Y., Ultrasonic spray pyrolysis synthesis of Ag/TiO_2 nanocomposite photocatalysts for simultaneous H_2 production and CO_2 reduction. *International Journal of Hydrogen Energy* **2012,** *37* (13), 9967-9976.

114. Asahi, R.; Morikawa, T.; Ohwaki, T.; Aoki, K.; Taga, Y., Visible-light photocatalysis in nitrogen-doped titanium oxides. *Science* **2001,** *293* (5528), 269-271.

115. Kohno, Y.; Hayashi, H.; Takenaka, S.; Tanaka, T.; Funabiki, T.; Yoshida, S., Photo-enhanced reduction of carbon dioxide with hydrogen over Rh/TiO_2. *Journal of Photochemistry and Photobiology a-Chemistry* **1999,** *126* (1-3), 117-123.

116. Liu, L.; Zhao, C.; Pitts, D.; Zhao, H.; Li, Y., CO_2 photoreduction with H_2O vapor by porous MgO-TiO_2 microspheres: effects of surface MgO dispersion and CO_2 adsorption-desorption dynamics. *Catalysis Science & Technology* **2014**.

117. Liu, L. J.; Zhao, C. Y.; Zhao, H. L.; Pitts, D.; Li, Y., Porous microspheres of MgO-patched TiO_2 for CO_2 photoreduction with H_2O vapor: temperature-dependent activity and stability. *Chemical Communications* **2013,** *49* (35), 3664-3666.

118. Kohno, Y.; Ishikawa, H.; Tanaka, T.; Funabiki, T.; Yoshida, S., Photoreduction of carbon dioxide by hydrogen over magnesium oxide. *Phys Chem Chem Phys* **2001,** *3* (6), 1108-1113.

119. Li, Q. Y.; Zong, L. L.; Li, C.; Yang, J. J., Photocatalytic reduction of CO_2 on MgO/TiO_2 nanotube films. *Appl Surf Sci* **2014,** *314*, 458-463.

120. Xie, S. J.; Wang, Y.; Zhang, Q. H.; Fan, W. Q.; Deng, W. P.; Wang, Y., Photocatalytic reduction of CO_2 with H_2O: significant enhancement of the activity of Pt-TiO_2 in CH_4 formation by addition of MgO. *Chemical Communications* **2013,** *49* (24), 2451-2453.

121. Xiao, G.; Singh, R.; Chaffee, A.; Webley, P., Advanced adsorbents based on MgO and K_2CO_3 for capture of CO_2 at elevated temperatures. *International Journal of Greenhouse Gas Control* **2011,** *5* (4), 634-639.

122. Chakradhar, A.; Burghaus, U., Carbon dioxide adsorption on MgO(001)–CO_2 kinetics and dynamics. *Surface Science* **2013,** *616* (0), 171-177.

123. Gao, Y. S.; Zhang, Z.; Wu, J. W.; Yi, X. F.; Zheng, A. M.; Umar, A.; O'Hare, D.; Wang, Q., Comprehensive investigation of CO_2 adsorption on Mg-Al-CO_3 LDH-derived mixed metal oxides. *Journal of Materials Chemistry A* **2013,** *1* (41), 12782-12790.

124. Wang, J. W.; Stevens, L. A.; Drage, T. C.; Wood, J., Preparation and CO_2 adsorption of amine modified Mg-Al LDH via exfoliation route. *Chemical Engineering Science* **2012,** *68* (1), 424-431.

125. Dadwhal, M.; Kim, T. W.; Sahimi, M.; Tsotsis, T. T., Study of CO_2 Diffusion and Adsorption on Calcined Layered Double Hydroxides: The Effect of Particle Size. *Industrial & Engineering Chemistry Research* **2008,** *47* (16), 6150-6157.

126. Bujdoso, T.; Patzko, A.; Galbacs, Z.; Dekany, I., Structural characterization of arsenate ion exchanged MgAl-layered double hydroxide. *Applied Clay Science* **2009,** *44* (1-2), 75-82.

127. Teramura, K.; Iguchi, S.; Mizuno, Y.; Shishido, T.; Tanaka, T., Photocatalytic Conversion of CO_2 in Water over Layered Double Hydroxides. *Angewandte Chemie-International Edition* **2012,** *51* (32), 8008-8011.

128.   Zhao, M. Q.; Zhang, Q.; Huang, J. Q.; Wei, F., Hierarchical Nanocomposites Derived from Nanocarbons and Layered Double Hydroxides - Properties, Synthesis, and Applications. *Advanced Functional Materials* **2012,** *22* (4), 675-694.

129.   Kuang, Y.; Zhao, L. N.; Zhang, S. A.; Zhang, F. Z.; Dong, M. D.; Xu, S. L., Morphologies, Preparations and Applications of Layered Double Hydroxide Micro-/Nanostructures. *Materials* **2010,** *3* (12), 5220-5235.

130.   Reddy, M. K. R.; Xu, Z. P.; Lu, G. Q.; Da Costa, J. C. D., Layered double hydroxides for CO2 capture: Structure evolution and regeneration. *Industrial & Engineering Chemistry Research* **2006,** *45* (22), 7504-7509.

131.   Leon, M.; Diaz, E.; Bennici, S.; Vega, A.; Ordonez, S.; Auroux, A., Adsorption of CO2 on Hydrotalcite-Derived Mixed Oxides: Sorption Mechanisms and Consequences for Adsorption Irreversibility. *Industrial & Engineering Chemistry Research* **2010,** *49* (8), 3663-3671.

132.   Yang, J.-I.; Kim, J.-N., Hydrotalcites for adsorption of CO_2 at high temperature. *Korean J. Chem. Eng.* **2006,** *23* (1), 77-80.

133.   Wang, X. P.; Yu, J. J.; Cheng, J.; Hao, Z. P.; Xu, Z. P., High-temperature adsorption of carbon dioxide on mixed oxides derived from hydrotalcite-like compounds. *Environmental Science & Technology* **2008,** *42* (2), 614-618.

134.   Wang, J.; Li, D. D.; Yu, X. A.; Zhang, M. L.; Jing, X. Y., Fabrication of layered double hydroxide spheres through urea hydrolysis and mechanisms involved in the formation. *Colloid and Polymer Science* **2010,** *288* (14-15), 1411-1418.

135.   Zhao, C. Y.; Liu, L. J.; Zhang, Q. Y.; Wang, J.; Li, Y., Photocatalytic conversion of CO2 and H2O to fuels by nanostructured $Ce-TiO_2$/SBA-15 composites. *Catalysis Science & Technology* **2012,** *2* (12), 2558-2568.

136.   Valente, J. S.; Tzompantzi, F.; Prince, J., Highly efficient photocatalytic elimination of phenol and chlorinated phenols by CeO_2/MgAl layered double hydroxides. *Applied Catalysis B: Environmental* **2011,** *102* (1–2), 276-285.

137.   Zhao, Y. S.; Li, J. G.; Fang, F.; Chu, N. K.; Ma, H.; Yang, X. J., Structure and luminescence behaviour of as-synthesized, calcined, and restored MgAlEu-LDH with high crystallinity. *Dalton Transactions* **2012,** *41* (39), 12175-12184.

138.   Ye, K.; Lina, Z.; Shuai, Z.; Fazhi, Z.; Mingdong, D.; Sailong, X., Morphologies, Preparations and Applications of Layered Double Hydroxide Micro-/Nanostructures. *Materials (1996-1944)* **2010,** *3* (12), 5220-5235.

139.   Valente, J. S.; Rodriguez-Gattorno, G.; Valle-Orta, M.; Torres-Garcia, E., Thermal decomposition kinetics of MgAl layered double hydroxides. *Materials Chemistry and Physics* **2012,** *133* (2–3), 621-629.

140.   Seftel, E. M.; Mertens, M.; Cool, P., The influence of the Ti^{4+} location on the formation of self-assembled nanocomposite systems based on TiO_2 and Mg/Al-LDHs with photocatalytic properties. *Applied Catalysis B-Environmental* **2013,** *134*, 274-285.

141.   Amine, K.; Belharouak, I.; Chen, Z. H.; Tran, T.; Yumoto, H.; Ota, N.; Myung, S. T.; Sun, Y. K., Nanostructured Anode Material for High-Power Battery System in Electric Vehicles. *Advanced Materials* **2010,** *22* (28), 3052-3057.

142.   Endo, M.; Kim, C.; Nishimura, K.; Fujino, T.; Miyashita, K., Recent development of carbon materials for Li ion batteries. *Carbon* **2000,** *38* (2), 183-197.

143.   Shen, L. F.; Uchaker, E.; Yuan, C. Z.; Nie, P.; Zhang, M.; Zhang, X. G.; Cao, G. Z., Three-Dimensional Coherent Titania-Mesoporous Carbon Nanocomposite and Its

Lithium-Ion Storage Properties. *ACS Applied Material Interfaces* **2012,** *4* (6), 2985-2992.

144.   Zhang, J. W.; Yan, X. X.; Zhang, J. W.; Cai, W.; Wu, Z. S.; Zhang, Z. J., Preparation and electrochemical performance of TiO_2/C composite nanotubes as anode materials of lithium-ion batteries. *Journal of Power Sources* **2012,** *198*, 223-228.

145.   An, G. M.; Na, N.; Zhang, X. R.; Miao, Z. J.; Miao, S. D.; Ding, K. L.; Liu, Z. M., SnO_2/carbon nanotube nanocomposites synthesized in supercritical fluids: highly efficient materials for use as a chemical sensor and as the anode of a lithium-ion battery. *Nanotechnology* **2007,** *18* (43), 6.

146.   Guo, Z. P.; Du, G. D.; Nuli, Y.; Hassan, M. F.; Liu, H. K., Ultra-fine porous SnO_2 nanopowder prepared via a molten salt process: a highly efficient anode material for lithium-ion batteries. *Journal Materials Chemistry* **2009,** *19* (20), 3253-3257.

147.   Chang, P. Y.; Huang, C. H.; Doong, R. A., Ordered mesoporous carbon-TiO_2 materials for improved electrochemical performance of lithium ion battery. *Carbon* **2012,** *50* (11), 4259-4268.

148.   Deng, D.; Kim, M. G.; Lee, J. Y.; Cho, J., Green energy storage materials: Nanostructured TiO_2 and Sn-based anodes for lithium-ion batteries. *Energy & Environmental Science* **2009,** *2* (8), 818-837.

149.   Fang, H. T.; Liu, M.; Wang, D. W.; Sun, T.; Guan, D. S.; Li, F.; Zhou, J. G.; Sham, T. K.; Cheng, H. M., Comparison of the rate capability of nanostructured amorphous and anatase TiO_2 for lithium insertion using anodic TiO_2 nanotube arrays. *Nanotechnology* **2009,** *20* (22).

150.   Ganapathy, S.; van Eck, E. R. H.; Kentgens, A. P. M.; Mulder, F. M.; Wagemaker, M., Equilibrium Lithium-Ion Transport Between Nanocrystalline Lithium-Inserted Anatase TiO_2 and the Electrolyte. *Chemistry-a European Journal* **2011,** *17* (52), 14811-14816.

151.   Han, H.; Song, T.; Lee, E. K.; Devadoss, A.; Jeon, Y.; Ha, J.; Chung, Y. C.; Choi, Y. M.; Jung, Y. G.; Paik, U., Dominant Factors Governing the Rate Capability of a TiO_2 Nanotube Anode for High Power Lithium Ion Batteries. *ACS Nano* **2012,** *6* (9), 8308-8315.

152.   Okumura, T.; Fukutsuka, T.; Yanagihara, A.; Orikasa, Y.; Arai, H.; Ogumi, Z.; Uchimoto, Y., Nanosized Effect on Electronic/Local Structures and Specific Lithium-Ion Insertion Property in TiO_2-B Nanowires Analyzed by X-ray Absorption Spectroscopy. *Chemistry Materials* **2011,** *23* (16), 3636-3644.

153.   Das, S. K.; Bhattacharyya, A. J., Influence of Mesoporosity and Carbon Electronic Wiring on Electrochemical Performance of Anatase Titania. *Journal of Electrochemical Society* **2011,** *158* (6), A705-A710.

154.   Yang, Z. G.; Choi, D.; Kerisit, S.; Rosso, K. M.; Wang, D. H.; Zhang, J.; Graff, G.; Liu, J., Nanostructures and lithium electrochemical reactivity of lithium titanites and titanium oxides: A review. *Journal of Power Sources* **2009,** *192* (2), 588-598.

155.   Jiang, Y. M.; Wang, K. X.; Guo, X. X.; Wei, X.; Wang, J. F.; Chen, J. S., Mesoporous titania rods as an anode material for high performance lithium-ion batteries. *Journal of Power Sources* **2012,** *214*, 298-302.

156.   Dambournet, D.; Belharouak, I.; Amine, K., Tailored Preparation Methods of TiO_2 Anatase, Rutile, Brookite: Mechanism of Formation and Electrochemical Properties. *Chemistry Materials* **2010,** *22* (3), 1173-1179.

157.   Murphy, D. W.; Cava, R. J.; Zahurak, S. M.; Santoro, A., Ternary Li_xTiO_2 phases from insertion reactions. *Solid State Ionics* **1983,** *9/10, Part 1* (0), 413-417.

158.   Subramanian, V.; Karki, A.; Gnanasekar, K. I.; Eddy, F. P.; Rambabu, B., Nanocrystalline TiO2 (anatase) for Li-ion batteries. *Journal of Power Sources* **2006,** *159* (1), 186-192.

159.   Chen, X.; Mao, S. S., Titanium dioxide nanomaterials: Synthesis, properties, modifications, and applications. *Chemical Review* **2007,** *107* (7), 2891-2959.

160.   Yang, Z. X.; Du, G. D.; Meng, Q.; Guo, Z. P.; Yu, X. B.; Chen, Z. X.; Guo, T. L.; Zeng, R., Synthesis of uniform TiO_2@carbon composite nanofibers as anode for lithium ion batteries with enhanced electrochemical performance. *Journal of Materials Chemistry* **2012,** *22* (12), 5848-5854.

161.   Ohtani, B.; Prieto-Mahaney, O. O.; Li, D.; Abe, R., What is Degussa (Evonik) P25? Crystalline composition analysis, reconstruction from isolated pure particles and photocatalytic activity test. *Journal of Photochemistry and Photobiology a-Chemistry* **2010,** *216* (2-3), 179-182.

162.   Yang, C. C.; Zheng, Y. R., Improved the performance of dye-sensitized solar cells by incorporating mesoporous silica (SBA-15) materials in scattering layer. *Journal of Power Sources* **2012,** *201*, 387-394.

163.   Kavan, L.; Bacsa, R.; Tunckol, M.; Serp, P.; Zakeeruddin, S. M.; Le Formal, F.; Zukalova, M.; Graetzel, M., Multi-walled carbon nanotubes functionalized by carboxylic groups: Activation of TiO_2 (anatase) and phosphate olivines (LiMnPO4; LiFePO4) for electrochemical Li-storage. *Journal of Power Sources* **2010,** *195* (16), 5360-5369.

164.   Reddy, K. M.; Baruwati, B.; Jayalakshmi, M.; Rao, M. M.; Manorama, S. V., S-, N- and C-doped titanium dioxide nanoparticles: Synthesis, characterization and redox charge transfer study. *Journal of Solid State Chemistry* **2005,** *178* (11), 3352-3358.

165.   Sing, K. S. W.; Williams, R. T., Physisorption hysteresis loops and the characterization of nanoporous materials. *Adsorpt. Sci. Technol.* **2004,** *22* (10), 773-782.

166.   Zhen, M. M.; Su, L. W.; Yuan, Z. H.; Liu, L.; Zhou, Z., Well-distributed TiO_2 nanocrystals on reduced graphene oxides as high-performance anode materials for lithium ion batteries. *Rsc Advances* **2013,** *3* (33), 13696-13701.

167.   Ming, J.; Wu, Y. Q.; Nagarajan, S.; Lee, D. J.; Sun, Y. K.; Zhao, F. Y., Fine control of titania deposition to prepare C@TiO_2 composites and TiO_2 hollow particles for photocatalysis and lithium-ion battery applications. *Journal of Materials Chemistry* **2012,** *22* (41), 22135-22141.

168.   Chen, J. S.; Liu, H.; Qiao, S. Z.; Lou, X. W., Carbon-supported ultra-thin anatase TiO2 nanosheets for fast reversible lithium storage. *Journal of Materials Chemistry* **2011,** *21* (15), 5687-5692.

169.   Chen, J. S.; Lou, X. W., Anatase TiO_2 nanosheet: An ideal host structure for fast and efficient lithium insertion/extraction. *Electrochemical Communication* **2009,** *11* (12), 2332-2335.

170.   Wang, Q.; Wen, Z. H.; Li, J. H., A hybrid supercapacitor fabricated with a carbon nanotube cathode and a TiO2-B nanowire anode. *Advanced Functional Materials* **2006,** *16* (16), 2141-2146.

171.   Zhang, Q. Y.; Zhang, C. L.; Li, B.; Kang, S. F.; Li, X.; Wang, Y. G., Preparation and electrochemical properties of Ca-doped $Li_4Ti_5O_{12}$ as anode materials in lithium-ion battery. *Electrochimia Acta* **2013,** *98*, 146-152.

172.   Rahman, M. M.; Wang, J. Z.; Hassan, M. F.; Wexler, D.; Liu, H. K., Amorphous Carbon Coated High Grain Boundary Density Dual Phase $Li_4Ti_5O_{12}$-TiO_2: A

Nanocomposite Anode Material for Li-Ion Batteries. *Advanced Energy Materials* **2011,** *1* (2), 212-220.

173.   Jang, Y. J.; Jang, Y. H.; Kim, D. H., Carbohydrate-Derived Carbon Sheaths on TiO2 Nanoparticle Photoanodes for Efficiency Enhancement in Dye-Sensitized Solar Cells. *Particle & Particle Systems Characterization* **2013,** *30* (12), 1030-1033.

174.   Liu, L.; Fan, Q.; Sun, C.; Gu, X.; Li, H.; Gao, F.; Chen, Y.; Dong, L., Synthesis of sandwich-like TiO2@C composite hollow spheres with high rate capability and stability for lithium-ion batteries. *Journal of Power Sources* **2013,** *221* (0), 141-148.

175.   Ding, B.; Yuan, C. Z.; Shen, L. F.; Xu, G. Y.; Nie, P.; Zhang, X. G., Encapsulating Sulfur into Hierarchically Ordered Porous Carbon as a High-Performance Cathode for Lithium-Sulfur Batteries. *Chemistry-European Journal* **2013,** *19* (3), 1013-1019.

176.   Xin, S.; Yin, Y. X.; Wan, L. J.; Guo, Y. G., Encapsulation of Sulfur in a Hollow Porous Carbon Substrate for Superior Li-S Batteries with Long Lifespan. *Part. Part. Syst. Char.* **2013,** *30* (4), 321-325.

177.   Wang, D. W.; Li, F.; Liu, M.; Lu, G. Q.; Cheng, H. M., 3D aperiodic hierarchical porous graphitic carbon material for high-rate electrochemical capacitive energy storage. *Angew. Chem. Int. Edn.* **2008,** *47* (2), 373-376.

178.   Holdorf, M. M.; Owen, H. A.; Lieber, S. R.; Yuan, L.; Adams, N.; Dabney-Smith, C.; Makaroff, C. A., Arabidopsis ETHE1 Encodes a Sulfur Dioxygenase That Is Essential for Embryo and Endosperm Development. *Plant Physiol.* **2012,** *160* (1), 226-236.

179.   Wang, C.; Wan, W.; Chen, J. T.; Zhou, H. H.; Zhang, X. X.; Yuan, L. X.; Huang, Y. H., Dual core-shell structured sulfur cathode composite synthesized by a one-pot route for lithium sulfur batteries. *Journal of Materials Chemistry A* **2013,** *1* (5), 1716-1723.

180.   Wang, J. L.; Liu, L.; Ling, Z. J.; Yang, J.; Wan, C. R.; Jiang, C. Y., Polymer lithium cells with sulfur composites as cathode materials. *Electrochimia Acta* **2003,** *48* (13), 1861-1867.

181.   Ghosh, A.; Lee, Y. H., Carbon-Based Electrochemical Capacitors. *ChemsusChem* **2012,** *5* (3), 480-499.

182.   Magasinski, A.; Dixon, P.; Hertzberg, B.; Kvit, A.; Ayala, J.; Yushin, G., High-performance lithium-ion anodes using a hierarchical bottom-up approach. *Nature Materials* **2010,** *9* (4), 353-358.

CURRICULUM VITAE

CUNYU ZHAO

EDUCATION
Ph.D., Mechanical Engineering, University of WI-Milwaukee (Dec. 2014)
M.S., Chemical Engineering, Tianjin University, P.R. China (2008)
B.S., Chemical Engineering, Hefei University of Technology, P.R. China (2006)

PROFESSIONAL SKILLS
Gas chromatography (Agilent 7890A); Mass spectroscopy (Agilent 5975C); Physisorption apparatus (Micromeritics ASAP 2020); X-ray diffractometer (XRD); Scanning electron microscopy (SEM); Transmitting electron microscopy (TEM); Demonstrated experience with battery electrochemical characterization e.g. impedance spectroscopy(EIS), galvanostatic potentiometry, cycle life testing.
Microsoft Office software; PROII simulation software; Aspen Software; AutoCAD.

PROCESS ENGINEER EXPERIENCE
GTC (Beijing) Technology, Inc.   Process Engineer   Beijing, P.R. China   2008-2011
Responsible for aromatic extractive distillation process design, including process simulation, material balance, equipment sizing, piping and instrumentation design, and process flow design and analysis. Performed cost estimates, submitted project proposals, developed operating guidelines, start-up procedures and process design package.

Project Experiences

- Key person for project coordination among Sinopec Yanshan Petrochemical, SEI and GTC for Yanshan Styrene Recovery project. Both customers and PDP clients were satisfied with the immediate action upon project minute of meeting.
- Designed condensate recovery system for SECCO styrene project in Shanghai, China. Saved 10% energy of the total energy consumption; Specified instrumentation and line list for the project. Efficiently accomplished the project for customers.
- Designed GT-Styrene Recovery process for Jilin Petrochemical Co. based on specified raw pygas material with GTC's proprietary technology. Simulated the styrene extractive distillation process and optimized the process with heat integration by saving 10% energy. Prepared PFD drawing, material and utility balance.
- Designed GT-BTX process for Petrochina Daqing Co. Simulated the BTX Extractive Distillation process and Optimized the process with heat integration. Prepared PFD drawing, material and utility balance and Cost Estimation.
- Assisted start-up expert on Petrochina Dushanzi Co. BTX project start-up. Familiarized with on-site BTX unit problems and provide methods for resolving problems. Assisted foreign expert to communicate effectively with client.

TEACHING EXPERIENCE
University of WI-Milwaukee   Teaching Assistant   Milwaukee, WI   Sep.2011- May.2012
- Fluid Mechanics Lecture and Lab.   The students were satisfied about the course instruction and lab instruction. 97% of the class (32 students) got A- above score.

RESEARCH EXPERIENCE

University of WI-Milwaukee   Research Assistant   Milwaukee, WI   Jan. 2011- Dec.2014

- Research on TiO_2-based catalysts for application in CO_2 photoreduction.
- Innovated hybrid nanomaterials using as photocatalysts for CO_2 photoreduction with water. Improved the photocatalytic conversion activity of CO_2 with water to alternative fuels.
- Explored hybrid nanostructures alternative materials as anode for Lithium-ion batteries. By growing carbon on TiO_2, attained the good cyclability and rate capability for Li-ion batteries.
- Research, design and develop novel nanomaterial structure for use as cathodes for Li-S batteries and Li-ion batteries.
- Innovated porous microsphere carbon/sulfur nanostructure for Li-S battery cathode materials.   Inhibited shuttle effect and increase the conductivity of the electrode.

HONORS & AWARDS

- "Top 3" poster award in the graduate student poster competition at the Annual Spring Symposium of the Catalysis Club of Chicago held on May 13, 2014 at the BP Research Center.
- Third place prize in the graduate student poster competition UWM-CEAS Annual Poster Competition, 2014.
- University of Wisconsin-Milwaukee Distinguished Graduate Student Fellowship Award, 2014-2015.
- UWM Chancellor's Graduate Student Award, University of Wisconsin-Milwaukee, Milwaukee, WI, 2012-2014.
- First place prize in the graduate student poster competition at the Nano Science and Engineering Forum (NSEF) in 2012 at the AIChE Annual Meeting in Pittsburgh, PA.
- Student Travel Grant, 2013 AICHE Annual conference, San Francisco, CA, Nov., 2013.

PUBLICATIONS

- Liu, L.J., **Zhao, C.Y.**, Zhao, H.L., Pitts, D.T., Li, Y.* CO_2 photoreduction with H_2O vapor by porous MgO/TiO_2 microspheres: effects of surface MgO dispersion and CO_2 adsorption/desorption dynamics. Catalysis Science & Technology, 2014.
- **Zhao, C.Y.**, Liu, L.J., Krall, A.J., Zhao, H.L., Wen, Z.H., Chen, J.H., Hurley, P., Jiang, J.W., Li, Y.*. Sulfur-infiltrated porous carbon microspheres with controllable multi-modal pore size distribution for high energy lithium–sulfur batteries. Nanoscale, 2014, 6(2), 882-888.
- Liu, L.J., Pitts, D.T., Zhao, H.L., **Zhao, C.Y.**, Li, Y.* Silver-incorporated bicrystalline (anatase/brookite) TiO_2 microspheres for CO_2 photoreduction with water in the presence of methanol. Applied Catalysis A: General. 2013, 467, 474-482.
- Liu, L.J., **Zhao, C.Y.**, Li, Y.*. Spontaneous dissociation of CO_2 to CO on defective surface of $Cu(I)/TiO_{2-x}$ nanoparticles at room temperature. Journal of Physical Chemistry C. 2013, 117, 10191-10202.
- Liu, L.J., **Zhao, C.Y.**, Zhao, H.L., Pitts, D.T., Li, Y.*. Porous microspheres of MgO-patched TiO_2 for CO_2 photoreduction with H_2O vapor: Temperature-dependent activity and stability. Chemical Communications. 2013, 49, 3664-3666.
- Gu, H.B., Guo, J., Wei, H.G., Huang, Y.D., **Zhao, C.Y.**, Li, Y., Wu, Q.L., Haldolaarachchige, N., Young, D.P., Wei, S.Y., Guo, Z.H. *, Giant magnetoresistance in non-magnetic phosphoric acid doped polyaniline silicon Nanocomposites with higher magnetic field sensing sensitivity.
Physical Chemistry Chemical Physics, 2013, 15, 10866-10875.

- **Zhao, C.Y.**, Liu, L.J., Zhang, Q.Y., Wang, J., Li, Y.* Photocatalytic Conversion of CO_2 and H_2O to Fuels by Nanostructured Ce-TiO_2/SBA-15 Composites. Catalysis Science & Technology, 2012, 2, 2558-2568.
- **Zhao, C.Y.**, Krall, A.J., Zhao, H.L., Zhang, Q.Y., Li, Y.*. Ultrasonic spray pyrolysis synthesis of Ag/TiO_2 nanocomposite photocatalysts for simultaneous H_2 production and CO2 reduction. International Journal of Hydrogen Energy, 2012, 37(13), 9967-9976.
- Zeng, L.P., **Zhao, C.Y.**, Zhu, Z.K., Wu, X.S.. Comprehensive processing of coke oven gas and coking crude benzol. Fuel & Chemical Processes, 2009, 6, 36-38.
- Zhang, Y., **Zhao, C.Y.**, Liang, H., Liu, Y.*. Macroporous Monolithic Pt/γ-Al_2O_3 and K–Pt/γ-Al_2O_3 Catalysts Used for Preferential Oxidation of CO. Catalysis Letters, 2009, 127 (3), 339-347.
- Zhang, Y., Liang, H., **Zhao, C.Y.**, Liu, Y.*. Macroporous alumina monoliths prepared by filling polymer foams with alumina hydrosols. Journal of Materials Science, 2009, 44 (3), 931-938.

CONFERENCE PAPERS

- L.J. Liu, C.Y. Zhao, H.L. Zhao, D. Pitts and Y. Li, "CO2 Photoreduction With H2O Vapor By Porous MgO/TiO2 Microspheres: Temperature-Dependent Activity and Stability" Presented at the 2013 AICHE Annual meeting Catalysis and Reaction Engineering (CRE) Division, San Franscisco, CA, Nov. 2 - 8, 2013.
- C.Y. Zhao, L.J. Liu, A.J. Krall, H.L. Zhao, and Y. Li, "Sulfur-Infiltrated 3D Porous Carbon Microsphere Nanoarchitecture for High Energy Lithium-Sulfur Batteries" Presented at the the 2013 AICHE Annual meeting Nano Science and Engineering Forum (NSEF), San Franscisco, CA, Nov. 2 - 8, 2013.
- C.Y. Zhao, L.J. Liu, A.J. Krall, H.L. Zhao, and Y. Li, "Ultrasonic Spray Pyrolysis Synthesis of Ag-TiO2 Nanocomposite Photocatalysts for Simultaneous H2 Production and CO2 Reduction" Presented at the 2012 AICHE Annual meeting Nano Science and Engineering Forum (NSEF), Pittsburgh, PA, Oct. 28-Nov. 2, 2012
- C.Y. Zhao, and Y. Li,, "Photocatalytic Conversion of CO2 to Fuels by Nanostructured CeO2-TiO2/SiO2 Catalysts" Presented at the 2013 AICHE Annual meeting Catalysis and Reaction Engineering (CRE) Division, Minneapolis, MN., Oct. 16-Oct. 21, 2011.